Waves in disordered particulate materials: transmission and inter-particle correlations

Aristeidis Karnezis

Department of Mechanical Engineering

University of Sheffield

Supervisors: Dr Art L. Gower, Dr Anton Krynkin

A Thesis Submitted for the degree of
Doctor of Philosophy
in the Faculty of Engineering

Sheffield
11th March 2024

Acknowledgements

I consider myself incredibly fortunate to have been given the opportunity to pursue a field of study that truly captivates my interest. The past four years have been nothing short of remarkable. I would like to express my deep appreciation and gratitude to my supervisor, Dr Artur Gower, for his continuous support, invaluable guidance, and exceptional mentorship throughout my doctoral journey at the University of Sheffield. Without his expertise, patience, and belief in my research, this thesis would not have been possible. His dedication to fostering my growth as a researcher has played a pivotal role in shaping my academic and personal development.

I would like to extend my heartfelt thanks to the UK Acoustics Network (UKAN) for their funding support that enabled me to attend conferences and workshops to broaden my academic horizons. Their financial assistance has not only enriched my research experience but has also allowed me to connect with fellow scholars and professionals in the field.

I am indebted to my colleagues and fellow researchers, Paulo Sergio Piva and Kevish Napal, for their collaboration, and the countless insightful discussions that have enriched my research experience.

I would also like to thank the wonderful people within the Dynamics Research Group for making my academic journey so enjoyable. I am deeply appreciative of the collaborative spirit, shared laughter and the sense of community that we've built together.

My sincere appreciation goes to my family for their continuous support, encouragement, and understanding throughout this demanding journey.

Last but certainly not least, I want to express my deepest gratitude to Argyro. Thank you for accompanying me through the highs and lows of this academic journey. Your belief in me provided the motivation and resilience needed to overcome the challenges of pursuing a PhD.

Abstract

At its core, this dissertation not only contributes to a deeper understanding of wave propagation in particulate materials but also opens new avenues for innovative engineering solutions in fields such as acoustic and electromagnetic material sensing and design. For instance, it contributes to the development of materials for specific wave-manipulation applications such as selectively blocking or absorbing specific wave frequencies. It challenges the standard approach that on average, a wave propagates through random particulate materials with a single effective wavenumber, demonstrating instead the presence of multiple effective wavenumbers due to strong multiple scattering phenomena. This finding is surprising, considering the homogeneous and isotropic nature of the medium and our focus on scalar waves. To confirm these predictions, we conduct high-fidelity Monte-Carlo simulations, avoiding any statistical assumptions and providing the first clear evidence that there is indeed more than one effective wavenumber. However, when performing simulations we came across another unresolved gap in the theory concerning the incident wave that encounters a material with random microstructure. It is well known that any incident wave will eventually be completely replaced by some sort of effective transmitted wave. This is often referred to as the extinction of the incident wave. What was not clear is how far does the incident wave travel before being replaced by an effective wave? In disordered particulate materials we prove that the incident wave does not propagate within the material more than the correlation length between particles. In more detail, the extinction length is exactly equal to the maximum distance at which two particles are still correlated. This result not only helps perform numerical simulations, but is important to know in any experimental measurement, or even when designing materials to control wave propagation. A further challenge we encountered when comparing Monte-Carlo simulations, of thousands of particles, with theoretical predictions, is that the typically used pair-correlations $\mathrm{g}(r)$ - where r is the distance between the particles - did not match exactly the pair-correlations from our Monte-Carlo simulations. This naturally led us to investigate the discrepancy between theoretical pair-correlation functions

and those derived from our Monte-Carlo simulations. This motivated our research on the realizability problem – whether a specific particle configuration can be calculated to match a given pair-correlation. Recognising the significant role of pair-correlations in fields like chemistry and materials science, we demonstrate a way to formulate the realizability problem as a smooth optimisation problem, where the gradients can be easily calculated. This approach, relying on gradient-based methods, promises more efficient solutions compared to traditional brute-force, non-gradient-based techniques.

Contents

List of Tables

List of Figures

Declaration

I, Aristeidis Karnezis, confirm that the Thesis is my own work. I am aware of the University's Guidance on the Use of Unfair Means. This work has not been previously been presented for an award at this, or any other, university.

Chapter 1

Introduction

In the field of materials science and engineering, there is a fundamental truth that applies across all length scales: most materials are composed of a complex and seemingly chaotic arrangement of smaller particles. We will refer to these as particulate materials. This universal characteristic extends from the subatomic world of particle physics to the more tangible and practical world of everyday materials. In particle physics, scientists delve into the subatomic landscape, unravelling the mysterious behaviour of particles on a scale so small that it challenges the limits of human comprehension. Yet, a parallel truth emerges when we zoom out to macroscopic levels: in the domain of everyday materials, we encounter a world where matter is not uniform but consists of an ensemble of smaller constituents, which we refer to as particles, each with its unique properties and interactions. Because particulate materials are so common, designing and characterising them has a wide range of applications across many industries.

Particulate nature of matter. In the world around us, particulate materials are everywhere. From composite materials, such as fibre composites, to suspensions, emulsions and powders (Figure 1.1). Such materials are valuable products across many industries and have empowered advancements in many research areas [70]. For example, pharmaceutical powders play a vital role in the formulation of medicines since the effectiveness of a drug can be strongly influenced by the exact size, shape, and distribution of its constituent particles [57, 70]. In the field of food science and industrial processes, emulsions/dispersions of one immiscible liquid within another, rely on the stable distribution of thousands of oil droplets. In this case, the performance of emulsions in food products, cosmetics, and pharmaceuticals is linked to the control of particle size and uniformity [1, 13]. Furthermore, within the field of advanced materials and composites, understanding the aggregation and dispersion of particles

within a matrix is vital for tailoring mechanical, electrical, and thermal properties[32, 34, 60]. Composite materials in aerospace, automotive, and construction industries are prime examples of where engineered particle arrangements hold the key to enhanced performance [58].

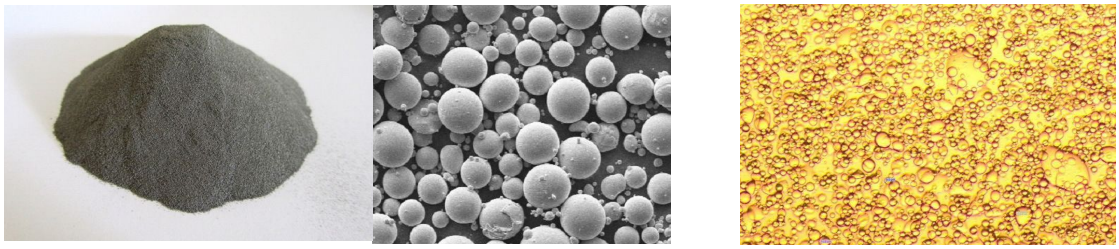

Figure 1.1: On the left, metal powders and their microstructure. On the right, an emulsion made of oil particles suspended in water. Together, these images provide information into the composition and internal structures of different materials.

Given the wide range and significance of particulate materials, it is important to develop robust methodologies to measure, analyse, and ultimately design these materials [1, 10]. Waves, either mechanical (like sound) or electromagnetic (like light), are ideal for sensing and probing particulates because they can be energy-efficient, non-invasive, and quick. These waves also have well-established governing equations that can provide valuable insights into materials if we have detailed knowledge of the material's microstructure.

The challenge, however, arises when we encounter materials with disordered or random microstructures. In most cases, it is impossible to have a complete knowledge of the microstructure of these materials. To deal with this lack of knowledge, we need to use probability distributions to describe the microstructure or distribution of particles. We then rely on a range of statistical tools such as ensemble averaging and statistical closure assumptions to make these complex systems solvable [33, 45, 46, 71].

The interaction of classical waves - such as electromagnetic and acoustic waves - with particulate materials has been well-studied within certain limits. Specifically, when considering long wavelengths [2, 6, 41, 52, 53], where the particles appear small compared to the wavelength of the incoming wave, there is a solid understanding of how to calculate the effective properties of these materials.

In scenarios where multiple scattering is weak, a branch of theory known as Mie theory, has played a central role [8, 40, 44, 56]. Mie theory allows us to characterise particulate materials in the dilute limit, where the re-scattering between the particles can be ignored. That is, the total scattered field is approximately equal to the incident

wave scattered from every particle once. This theory has led to several successful characterisation methods, including Dynamic Light Scattering and techniques based on laser diffraction patterns that have revolutionised how we assess and understand particulate materials [30, 38]. They provide valuable information about particle size, size distribution, and sometimes even shape, allowing researchers and industries to make informed decisions, optimise processes, and develop innovative products across a spectrum of applications [57].

Yet, there are many settings in which these techniques do not work. When there is strong multiple scattering between the particles, these techniques break down, or require many steps such as filtering and diluting the material to reduce the effects of multiple scattering. These extra steps are done in a laboratory setting, making it difficult to use these techniques in production. One clear application is to measure powders and emulsions in process, which are often too dense for single scattering theories, but still need to be measured to optimise the process [77].

1.1 Background

One of the fundamental theories used in the study of waves in materials with random microstructure is the Multiple Scattering Theory [33, 40, 45, 46, 71]. Multiple scattering occurs when waves re-scatter from particles, and other obstacles, many times. It introduces complexity in describing the behaviour of the average wave due to complex interference patterns. It is an unavoidable feature when using waves to probe dense particulates, and it is still not completely resolved how waves travel in these materials, or how to measure these materials with waves. The scenario that is least understood is for intermediate wavelengths, which are neither very long compared to the particles, or extremely short [23, 25, 26, 28]. This is the regime that this dissertation focuses on.

In this section, we give a very brief summary of multiple scattering between particles to help aid the discussion. More detail is provided in Chapter 2 and [25, 26, 39, 40].

We consider a circular cylinder with radius a and describe its geometry using two coordinate systems: The Cartesian (x,y) - where the centre of the cylinder is denoted by $O = (0, 0)$, and the plane polar coordinates (r, θ), where $x = rcos\theta$ and $y = rsin\theta$.

Incident wave. Imagine a scenario where a plane-wave with wavenumber k is impinging on the cylinder. This incident wave, denoted as u_{inc} is characterised by the

equation:

$$u_{\text{inc}} = e^{\mathrm{i}k(x\cos\theta_{in}+y\sin\theta_{in})} = \mathrm{e}^{\mathrm{i}kr\cos(\theta-\theta_{in})}. \tag{1.1}$$

In this equation, θ_{in} represents the angle of incidence. To further explain this wave and simplify the problem, we employ the Jacobi-Anger expansion [76]:

$$\mathrm{e}^{\mathrm{i}w\cos(\theta-\theta_{in})} = \sum_{n=-\infty}^{+\infty} \mathrm{i}^n \mathrm{J}_n(w)\mathrm{e}^{\mathrm{i}n(\theta-\theta_{in})}, \tag{1.2}$$

where $\mathrm{J}_n(w)$ is the Bessel function of the first kind of order n. Substituting (1.2) into (1.1), we express the incident plane-wave as a superposition of cylindrical waves. In other words, when u_{inc} hits the cylinder, the wave scatters in all directions, generating a set of n cylindrical waves. Each of these cylindrical waves represents a different way the original wave has been affected by the cylinder. Consequently, the incident wave can be expressed as:

$$u_{\text{inc}} = \sum_{n=-\infty}^{\infty} g_n \mathrm{J}_n(kr)\mathrm{e}^{\mathrm{i}n\theta}, \qquad \text{for all } r, \tag{1.3}$$

where $g_n = \mathrm{i}^n\mathrm{e}^{-\mathrm{i}n\theta_{in}}$ indicates the coefficients of the incident wave.

Scattered waves. When we work in plane polar coordinates, the Helmholtz equation gives rise to two linearly independent solutions that are represented as:

$$\mathrm{J}_n(kr)\mathrm{e}^{\mathrm{i}n\theta} \qquad \text{and} \qquad \mathrm{Y}_n(kr)\mathrm{e}^{\mathrm{i}n\theta}, \qquad n = 0, \pm1, \pm2, \dots . \tag{1.4}$$

Here, the first term corresponds to the Bessel function of the first kind, while the second term represents the Bessel function of the second kind. Combining these two components of Bessel functions and complex exponentials:

$$\big[\mathrm{J}_n(kr) + \mathrm{i}\mathrm{Y}_n(kr)\big]\mathrm{e}^{\mathrm{i}n\theta} \equiv \mathrm{H}_n^{(1)}(kr)\mathrm{e}^{\mathrm{i}n\theta}, \qquad n = 0, \pm1, \pm2, \dots , \tag{1.5}$$

we generate the Hankel function of the first kind $\mathrm{H}_n^{(1)}$, which represents a cylindrical wave that is radiated away from the origin. This function satisfies the Sommerfeld radiation condition [40, 55, 62], which states that, in two dimensions, the wave behaves as an outgoing wave at infinity with its amplitude decaying according to the condition:

$$\sqrt{r}\left(\frac{\partial u_{\text{sc}}}{\partial r} - \mathrm{i}ku_{\text{sc}}\right) \to 0, \qquad \text{as } r \to \infty. \tag{1.6}$$

This property ensures that the Hankel function of the first kind accurately describes wave propagation in scenarios where the wave extends to infinity without reflection.

To be consistent with the symmetries of the incident wave, we introduce the scattered wave u_{sc} as the response of the cylinder to the incident wave. Thus:

$$u_{\mathrm{sc}} = \sum_{n=-\infty}^{\infty} f_n \mathrm{H}_n(kr)\mathrm{e}^{\mathrm{i}n(\theta-\theta_{in})}, \qquad \text{for } r \geq a, \tag{1.7}$$

where the coefficients f_n carry information about how the cylinder interacts with the incident wave and how it scatters energy. For our convenience, we also express $\mathrm{H}_n^{(1)}$ as H_n.

Total wave. To fully address the problem, it is essential to establish a boundary condition at the surface of the cylinder. This boundary condition determines how the waves interact with the surface of the cylinder and how they propagate in the vicinity of the cylinder. Essentially, it provides the necessary link between the incident coefficients g_n and the scattered coefficients f_n.

To aid our discussion, we introduce two types of boundary conditions that will be the focus of this dissertation:

- *Dirichlet boundary condition* (sound-soft):

$$u_{\mathrm{tot}} = 0 \;\text{ or }\; u_{\mathrm{sc}} = -u_{\mathrm{inc}} \;\text{ on the cylinder boundary.}$$

- *Neumann boundary condition* (sound-hard):

$$\frac{\partial u_{\mathrm{tot}}}{\partial r} = 0 \;\text{ or }\; \frac{\partial u_{\mathrm{sc}}}{\partial r} = -\frac{\partial u_{\mathrm{inc}}}{\partial r} \;\text{ on the cylinder boundary.}$$

where $u_{\mathrm{tot}} = u_{\mathrm{inc}} + u_{\mathrm{sc}}$ represents the total field and $\frac{\partial}{\partial r}$ denotes normal differentiation on the boundary of the cylinder.

Applying, for example, Neumann's boundary conditions on the cylinder, we take the derivatives of equations (1.1) and (1.7) and set $r = a$. This leads to:

$$\sum_{n=-\infty}^{\infty} k\big[g_n \mathrm{J}_n^{'}(ka) + f_n \mathrm{H}_n^{'}(ka)\big]\mathrm{e}^{\mathrm{i}n(\theta-\theta_{in})} = 0, \qquad \text{for } 0 \leq \theta - \theta_{in} < 2\pi. \tag{1.8}$$

Then, using the orthogonality property of the complex exponentials, it is clear that the expression within the braces $[\,]$ must be equal to zero for every n. Therefore, we can

determine the coefficients f_n as:

$$f_n = -\frac{\mathrm{J}_n'(ka)}{\mathrm{H}_n'(ka)} g_n. \tag{1.9}$$

With these coefficients established, we can then express the scattered field at all points where $r \geq a$ using (1.7).

T-Matrix method. Imagine now the circular cylinder as a particle. The T-matrix method, first introduced by Waterman [43, 75], is an operation existing only when scattering is linear and essentially accounts for the boundary conditions of the particle. It also relates the known incident coefficients g_n with the scattering coefficients f_n as follows:

$$f_m = \sum_{n=-\infty}^{\infty} T_{mn} g_n. \tag{1.10}$$

In other words, (1.9) can be expressed in terms of the T-matrix:

$$T_{mn} = -\left[\frac{\mathrm{J}_n'(ka)}{\mathrm{H}_n'(ka)}\right] \delta_{mn}. \tag{1.11}$$

As shown in (1.11), the T-matrix remains unaffected by the incident field and governs the scattering of waves by the particle. This implies that the T-matrix relies on the particle's inner properties, including its shape, size, density, and other internal properties [20, 21]. When we modify these properties, we have to redo the calculations for the boundary conditions to find the new T-matrix. It is also important to remember that (1.7) will be affected by the changes we make to the particle, yet, (1.10) remains the same.

In this dissertation, we are interested in the case of homogeneous cylinders/-particles. Assume u corresponds to the acoustic pressure, ρ and c the density of the background material and the speed of the wave, respectively. The shape of the particle is circular with density ρ_0, speed of sound c_0 and radius r_0. In the case where the continuity of pressure and displacement across the particle's boundary is applied [37, Section IV A], we obtain that:

$$T_{mn} = \delta_{mn} T_n, \quad \text{with} \quad T_n = -\frac{q_0 \mathrm{J}_n'(kr_0)\mathrm{J}_n(k_0 r_0) - \mathrm{J}_n(kr_0)\mathrm{J}_n'(k_0 r_0)}{q_0 \mathrm{H}_n'(kr_0)\mathrm{J}_n(k_0 r_0) - \mathrm{H}_n(kr_0)\mathrm{J}_n'(k_0 r_0)}, \tag{1.12}$$

where $q_0 = \frac{\rho_0 c_0}{\rho c}$, $k_0 = \frac{\omega}{c_0}$ and ω is the frequency of the incident wave.

In the next section, we will focus on the multiple scattering of waves from one configuration of particles. We will employ the T-matrix method as it is a very powerful tool

for multiple scattering problems [27, 47] and we will exploit the multiple scattering of waves to reach to the governing equation for one configuration of particles.

Scattering from J cylinders. Assume a region $\mathcal{R}$ filled with J particles as shown in Figure 1.2. For our convenience and to formulate a mathematical description, we

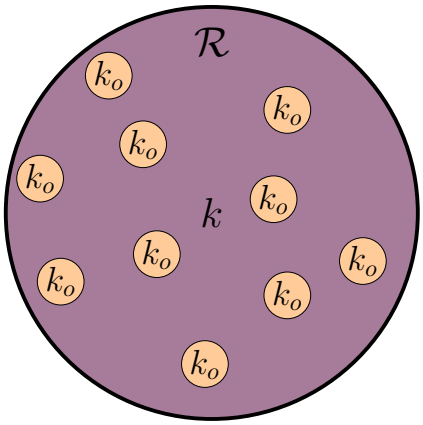

$$\nabla^2 u(r) + k^2 u(r) = 0, \qquad \text{for background material}$$
$$\nabla^2 u(r) + k_o^2 u(r) = 0, \qquad \text{for particles}$$

Figure 1.2: In the absence of particles from the material, the total wave will satisfy the scalar wave equation, where $k = \frac{\omega}{c}$ represents the wavenumber of the background material and c is the speed of sound in the background material. Likewise, when particles are present inside the material the total wave will satisfy the scalar wave equation, but this time $k_0 = \frac{\omega}{c_0}$ is the wavenumber of the material inside the particle with c_0 being the speed of sound inside the particle.

assume that all particles considered are similar, besides their position. The total field can be expressed as a superposition of the incident wave and all the scattered waves generated from each different particle. Thus:

$$u_{\text{tot}} = u_{\text{inc}} + \sum_{i=1}^{N} u_{\text{sc}}^i, \tag{1.13}$$

where u_{inc} is the incident field and u_{sc}^i the scattered field by the i-th particle.

The next step is to introduce the incident field u_{inc} and the scattered field u_{sc} in two dimensions. To do that, we employ once again the two separate solutions of the Helmholtz equation, namely the cylindrical Bessel and Hankel functions of the first kind. This leads to:

$$\mathrm{V}_n(k\boldsymbol{r}) = \mathrm{J}_n(kr)\mathrm{e}^{\mathrm{i}n\theta}, \tag{1.14}$$

$$\mathrm{U}_n(k\boldsymbol{r}_j) = \mathrm{H}_n(kr_j)e^{in\theta_j}, \tag{1.15}$$

where $\boldsymbol{r}_j = (r_j, \theta_j)$ stands for the position vector of the j-th particle expressed in polar coordinates.

Now, substituting (1.14) in (1.3) and (1.15) in (1.7), equation (1.13) can be rewritten in the form:

$$u_{\text{tot}} = \sum_{n=-\infty}^{\infty} g_n \mathrm{V}_n(k\boldsymbol{r}) + \sum_{j=1}^{N} \sum_{n=-\infty}^{\infty} f_n^j \mathrm{U}_n(k\boldsymbol{r} - k\boldsymbol{r}_j). \tag{1.16}$$

Notice that the expression for the incident wave will remain the same as (1.3) since the incident wave does not depend on the positions of the particles of the material inside the region.

Before applying the T-matrix method we need to express (1.16) with respect to only one coordinate system. One way to do that is by combining multi-pole expansions with addition theorems. A multi-pole expansion corresponds to a mathematical series representing a function of angles and is widely used in problems involving the propagation of electromagnetic waves [40]. Addition theorems are a powerful tool that has the ability to transform an expansion around a point in space to an expansion around another point [40]. A representation can be found in Figure 1.3.

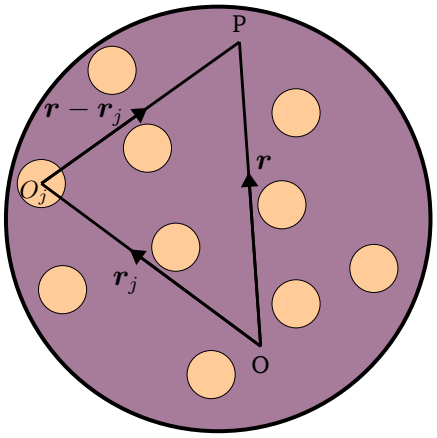

Figure 1.3: This figure illustrates the geometry of a group of J particles centred around a common origin, referred to as O. For each particle, there are local origins O_j, located at positions r_j.

Now, let us return to our problem. We will use Graf's addition theorem to re-expand the cylindrical waves with respect to the centre of a given particle i [40]. To accomplish this, we re-expand the incident wave in the following manner:

$$g_n \mathrm{V}_n(k\boldsymbol{r}) = g_n \sum_{n'} \mathrm{V}_{n-n'}(k\boldsymbol{r}_i)\mathrm{V}_{n'}(k\boldsymbol{r} - k\boldsymbol{r}_i). \tag{1.17}$$

Similarly, we expand the scattered waves while considering all particles except for the i-th particle ($j \neq i$):

$$f_n^{\,j}\mathrm{U}_n(k\boldsymbol{r} - k\boldsymbol{r}_j) = f_n^{\,j}\sum_{n'}\mathrm{U}_{n-n'}(k\boldsymbol{r}_i - k\boldsymbol{r}_j)\mathrm{V}_{n'}(k\boldsymbol{r} - k\boldsymbol{r}_i). \tag{1.18}$$

By doing this we can express our total field as the combination of the wave scattered by the i-th particle and an additional Bessel wave expansion:

$$u_{\mathrm{tot}}(\boldsymbol{r} - \boldsymbol{r}_i) = \sum_n f_n^{\,i}\mathrm{U}_n(k\boldsymbol{r} - k\boldsymbol{r}_i) + \sum_{n'} d_{n'}^{\,i}\mathrm{V}_{n'}(k\boldsymbol{r} - k\boldsymbol{r}_i), \tag{1.19}$$

such that (1.20)

$$d_{n'}^{\,i} = \sum_n \left[\sum_{j\neq i} f_n^{\,j}\mathrm{U}_{n-n'}(k\boldsymbol{r}_i - k\boldsymbol{r}_j) + g_n\mathrm{V}_{n-n'}(k\boldsymbol{r}_i)\right]. \tag{1.21}$$

Then, we can employ the T-matrix method and derive the expression for the coefficients $f_n^{\,i}$ as follows:

$$f_n^{\,i} = \sum_{m=-\infty}^{\infty} T_{nm} d_m^{\,i} \qquad \text{for } \; n, m = -\infty, \ldots, \infty \; \text{ and } \; j = 1, 2, \ldots, J. \tag{1.22}$$

with J being the number of particles. Ultimately, by iterating through this process for all particles ($i = 1, 2, \ldots,$ J) we arrive at a self-consistent linear system of equations [20, 21]:

$$f_n^{\,i} = T_n \sum_{n'} \mathrm{V}_{n'-n}(k\boldsymbol{r}_i) g_{n'} + T_n \sum_{j\neq i}\sum_{n'} \mathrm{U}_{n'-n}(k\boldsymbol{r}_i - k\boldsymbol{r}_j) f_{n'}^{\,j}. \tag{1.23}$$

The expression (1.23) corresponds to the formula [49, Equation 2.4] and characterises the scattering coefficients $f_n^{\,i}$.

Ensemble-averaged multiple scattering. The computation of $f_n^{\,i}$ allows us to solve the scattering problem for a given configuration of particles but there are still two challenges that we need to address:

- In most cases, we do not know the exact position of the particles.
- It is common to encounter a huge number of particles in the majority of industrial applications and nowadays there is no quantitative method to monitor the particulates.

Instead, we aim to describe the average properties, or statistical properties of the particles. To achieve this we use a standard technique from statistical physics called

ensemble averaging [19]. To do this we introduce the probability density of the particles occupying a specific position:

$$\mathrm{p}(\boldsymbol{r}_1, \ldots, \boldsymbol{r}_J), \tag{1.24}$$

where the variables $\boldsymbol{r}_i$ describe the positions of the i-th particle. The probability density function reflects the probability of finding the particles in a configuration where the first particle exists in the element of volume $d\boldsymbol{r}_1$ about the point $\boldsymbol{r}_1$, the second particle exists in the element of volume $d\boldsymbol{r}_2$ about the point $\boldsymbol{r}_2$ etc..

Then, we are able to attain the ensemble average of the total field $u(\boldsymbol{r})$ over all possible particle positions. In order to do this, we multiply the probability density function with the value for the configuration $\boldsymbol{r}_1, \boldsymbol{r}_2, \ldots, \boldsymbol{r}_J$, and finally we integrate over all positions $\boldsymbol{r}_i$ accessible to the particles. Thus, we obtain the expression:

$$\langle u(\boldsymbol{r}) \rangle = \int \ldots \int u(\boldsymbol{r}_1, \ldots, \boldsymbol{r}_J) \mathrm{p}(\boldsymbol{r}_1, \ldots, \boldsymbol{r}_J) d\boldsymbol{r}_1, \ldots, d\boldsymbol{r}_J. \tag{1.25}$$

The total ensemble-averaged wave $u(x)$ is defined as:

$$\langle u(\boldsymbol{r}) \rangle = \langle u_{\mathrm{inc}}(\boldsymbol{r}) \rangle + \langle u_{\mathrm{sc}}(\boldsymbol{r}) \rangle \,, \tag{1.26}$$

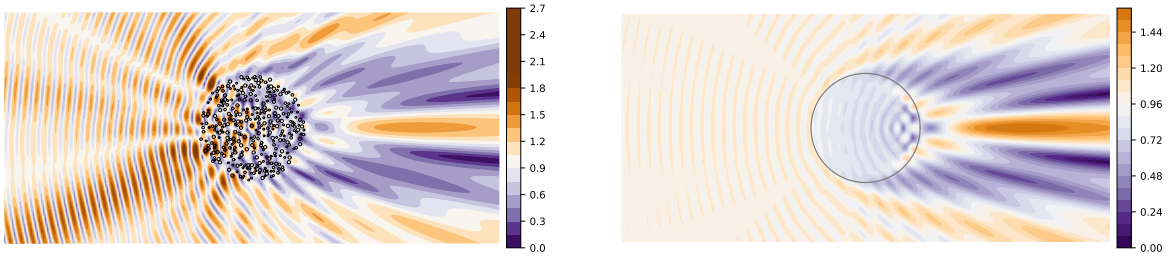

Figure 1.4: The picture on the left demonstrates the wave scattering of one specific configuration of particles due to an incident plane-wave. The picture on the right demonstrates the ensemble-averaged scattered wave of many different configurations of particles [25]. While the picture on the left displays the scattered field at a single moment in time, the picture on the right displays the average measurements of many sensors over time or space.

where $\langle u_{\mathrm{inc}}(\boldsymbol{r}) \rangle = u_{\mathrm{inc}}(\boldsymbol{r})$ and that is because there is no dependence of the incident field with particle configuration. Consequently, the main challenge is to solve the ensemble average of the scattering coefficient, $\langle u_{\mathrm{sc}}(\boldsymbol{r}) \rangle$, which basically identifies how all the particles scatter the incident wave on average. The interesting part about the ensemble-averaged picture of various configurations of particles illustrated in Figure 1.4, is that it looks like a wave that travels consistently without scattering but in an attenuating manner from the incident wave.

1.2 Research gaps & Key contributions

Traditional methods to modelling wave-particle interactions in materials with random microstructure often rely on the simplification of multiple scattering phenomena. This leads to assumptions that may not fully capture the complexity of how waves interact with particles.

Two main areas of interest in this dissertation are the exotic pair-correlations and the resonant particles. Exotic pair-correlations lead to unconventional relationships between pairs of particles within a material. These unique interactions can arise from factors such as particle shapes resulting in unexpected material behaviours such as enhanced or suppressed electrical, thermal, or mechanical properties. In parallel, for resonant particles, when the incident wave matches the resonant frequency, very strong multiple scattering occurs, and most mathematical models used break down [82]. These non-standard behaviours demand an extension of existing theoretical frameworks to accommodate such complexities.

Hence, this dissertation focuses on significant advancements in the field of wave propagation and how classical waves interact with materials with random microstructure. It includes novel findings that introduce the existence of multiple effective wavenumbers in homogeneous and isotropic materials. It proves the Ewald-Oseen extinction theorem for any geometry, frequency and incident wave and extends its applicability in the field of random particulates. It introduces the Cookie-cutter method which is a new method to derive particle pair-correlations from random configurations. It proposes a novel gradient-based optimisation method to tackle the realizability problem which examines if it is possible to achieve a specific particle configuration that matches a given pair-correlation.

These findings challenge existing views and open new paths for more accurate modelling and prediction of wave interactions in random materials. This will have a significant impact on how we design and characterise materials in various applications. The following paragraphs aim to provide a clear explanation of the main ideas discussed in this dissertation.

Multiple effective wavenumbers. In acoustics, the study of scattering from random particulate materials has been of great interest due to its relevance in various real-world applications such as sonar systems, underwater acoustics, and biomedical imaging, among others [57]. One motivation of the seminal work of Foldy [19], was to understand how underwater bubbles affect sonar. In this scenario, the simplest way to measure wave transmission or scattering is to take an average over time or space. In

mathematical terms this corresponds to an ensemble average over all possible particle configurations, and it replaces the unknown particles positions with a pair-correlation [35]. Further, if the particles are distributed uniformly, according to a uniform random distribution, then the average transmitted field is by consequence also uniform [25].

In the literature, it is commonly assumed that the ensemble average of a wave propagating in a particulate that has an isotropic distribution of particles, can be described with only one effective wavenumber:

$$k_\star = \frac{\omega}{c_\star} + i\alpha, \tag{1.27}$$

where $c_\star$ represents the effective wavespeed and α the rate of attenuation [11, 17, 37, 40, 64, 67, 72]. Note that (1.27) is for a wave propagating in the bulk medium with no waveguide. A case in point is depicted in Figure 1.5.

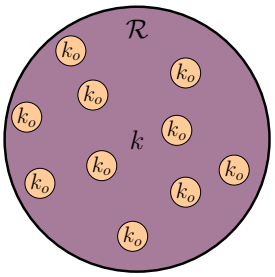

$\nabla^2 u(r) + k^2 u(r) = 0,$ for background material
$\nabla^2 u(r) + k_o^2 u(r) = 0,$ for particles

Before Averaging.

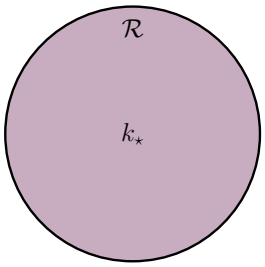

$\nabla^2 u(r) + k_\star^2 u(r) = 0$

After Averaging.

Figure 1.5: Assume a region $\mathcal{R}$ filled with J particles. Before averaging, the total wave satisfies different scalar wave equations as explained in Figure 1.2. After averaging, the total wave satisfies the scalar wave equation, where $k_\star$ given by (1.27), represents the complex effective wavenumber.

Of course, classical scalar waves in homogeneous and isotropic media only have one wavenumber. However, it does not follow directly from the mathematical modelling that a wave propagating in an ensemble-averaged medium has only one effective wavenumber $k_\star$: two different recent theoretical models [25, 26, 61, 78] challenge this assumption and have shown that there exist at least two complex effective wavenumbers for one fixed frequency within such materials. This is a highly unusual result, as it does not occur for classical waves, so these predictions require some validation.

A key contribution of this research is the provision of the first clear numerical evidence that confirms the presence of multiple effective wavenumbers triggered by factors such as particle correlations and specific frequencies that induce strong scattering. Our

findings underscore the importance of clarifying the theoretical framework to bridge the gap between theoretical expectations and numerical simulations, particularly when applying the governing equation (1.23) in practical scenarios.

Ewald-Oseen extinction theorem. To compare numerical simulations with the theoretically predicted transmitted field we had to first fill in a gap in the theory. It was not entirely clear from the theory where inside the material the incident wave is completely gone and replaced by an average effective transmitted wave. Despite extensive research in the field of scattering by particulates, exemplified by the works of Allegra and Hawley [3], the precise point of this wave transition within the material has not been covered.

The lack of clarity stems from the following quote:
"*When a wave is incident on a homogeneous medium, it is extinguished inside the medium in the process of interaction and is replaced by a wave propagated in the medium with a velocity different from that of the incident wave.*"

This statement introduced by Born and Wolf [54, 79] refers to the so-called *Ewald-Oseen extinction theorem* [4, 7]. This theorem is a fundamental assumption in wave physics stating that incident waves entering a material do not propagate or significantly contribute to the total transmitted field within the material [4, 22, 74]. While this assumption has been derived and employed extensively in the context of disordered particulate materials, including situations involving low-frequency waves and low particle volume fractions, disagreements persist in the scientific literature regarding the exact extinction length — the distance into the medium that incident waves travel before extinction.

This theorem finds application beyond the field of disordered materials and across a spectrum of scientific and engineering disciplines. For instance, it plays a crucial role in crystallography, aiding in the understanding of X-ray diffraction patterns in crystalline solids [18]. In the field of electromagnetic wave propagation, it helps analyse wave behaviour in various media, from dielectrics to conductors [22, 51]. In photonics and optics, it guides the design of optical devices like lenses and fibre optics. In electron microscopy, it assists in understanding electron-sample interactions. Additionally, acousticians apply the theorem to analyse sound wave propagation in diverse media, contributing to the design of acoustic systems and environmental noise predictions.

A major accomplishment of this work is that we are able to prove that for any particulate material geometry, frequency, and incident wave, the Ewald-Oseen extinction theorem is a result of more fundamental assumptions. With this proof, we can

clearly demonstrate that the extinction length is equal to the inter-particle correlation length L. These theoretical results enabled us to compare theory with high fidelity Monte-Carlo simulations, and confirm that multiple effective waves are indeed needed for densely packed particulates.

Cookie-cutter method. When we compared our Monte-Carlo simulations, which involve thousands of particles, to theoretical predictions, we faced another challenge: the typically used pair-correlations $\mathrm{g}(\boldsymbol{r})$ - where r is the distance between the particles - did not exactly match the pair-correlations from our Monte-Carlo simulations. The *Cookie-cutter* method offers a solution to this problem. This novel computational method significantly improves Monte-Carlo simulations by avoiding boundary artefacts that usually appear when placing particles within a finite region.

To delve deeper, when particles are placed in a finite region, they can sometimes end up too close to the boundaries, causing unrealistic interactions that would not occur in a real-world scenario. The Cookie-cutter method essentially cuts out smaller regions that contain the particle's centres, from the larger simulation region, avoiding the artefacts from the boundaries. By focusing on these smaller regions and averaging the results over several iterations, the method allows us to match the simulated particle interaction with the theoretical predictions leading to more accurate and reliable results.

Inter-particle correlations. The radial distribution function, also known as the pair-correlation function $\mathrm{g}(\boldsymbol{r})$ is a fundamental concept in various scientific fields [9, 35, 67, 68]. It plays a crucial role in understanding wave propagation and scattering in complex particulate materials. The pair-correlation effectively characterises the spatial distribution of particles, providing insight into their arrangement within the medium. A crucial application of the pair-correlation function arises when ensemble averaging the governing equations in particulate materials, as exemplified in (1.23). In this context, the function serves as the only term that captures the particle distribution information [35, 65, 66]. Essentially, $\mathrm{g}(\boldsymbol{r})$ describes how particle density varies as a function of distance from a reference particle in a configuration of particles. In other words, $\mathrm{g}(\boldsymbol{r})$ measures the probability of finding another particle at a distance $\boldsymbol{r}$ from a given reference particle. For instance, see Figure 1.6.

In statistical physics, the pair-correlation function is often used to deduce thermal conductivity and fluid properties [5, 48, 68]. For instance, in studying heat transfer in a disordered medium, the pair-correlation function helps determine how particles are arranged relative to one another. This arrangement affects the way heat is conducted through the material. By employing statistical methods and ensemble averaging,

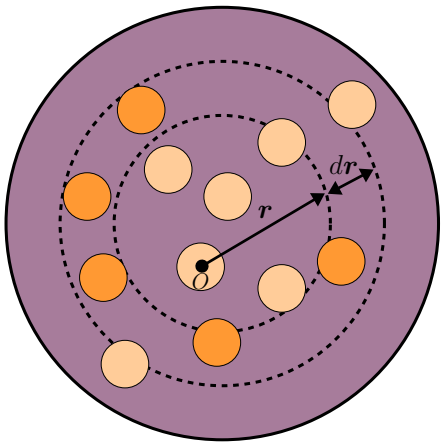

Figure 1.6: The standard method involves calculating the number of particles located within a specific distance of $\boldsymbol{r} + d\boldsymbol{r}$ away from a reference particle O. The concept is visually depicted, where one of the light orange particles serves as the point of reference, and the dark orange particles are those whose centres are contained within the dashed circular regions.

researchers can calculate the pair-correlations for different particle configurations. These correlations then can be used in developing accurate models for predicting the thermal properties and fluid behaviour in complex, disordered systems [48].

While theoretical methods are commonly used to understand and predict materials behaviour, it is less common but highly valuable to employ these methods for optimising material behaviour. For example, a notable part of this research focuses on the realizability problem, which is the challenge of determining whether a configuration of particles that matches a given pair-correlation function, exists [14, 15, 36, 66, 69, 81]. An important achievement of this work is that we demonstrate a way to formulate the realizability problem from first principles. This formulation transforms it into a smooth optimisation problem, where the gradients can be easily calculated, and therefore enables us to use gradient-based methods instead of the traditional brute-force, non-gradient-based methods. Solving the realizability problem is still an open challenge and impacts the mechanical, electrical, thermal and other properties of the material, ultimately leading to a modified and optimised behaviour.

The following research questions are designed to address the core challenges and opportunities highlighted in the preceding discussion.

1.3 Research questions

To push the limits on where the theoretical methods for waves in particulates can be used, we first need to carefully evaluate where the methods can and can not currently

be used. The main objective of this thesis is to address two common assumptions that are currently used and lack clear answers:

- Does the average transmitted field satisfy the wave equation with one, unique, complex effective wavenumber?
- What precisely happens to the incident wave as it enters the particulate material? More specifically, how far does it propagate before becoming extinct?

We also realise that the answer to these questions is intimately related to the properties of the pair-correlation, such as the correlation distance between particles. Also, as part of the numerical validation study, we needed to calculate particle configurations that exactly matched different inter-particle pair-correlations. This led us to address two more questions:

- How do inter-particle correlations influence the overall behaviour of the wave in the disordered materials?
- Given a pair-correlation, how do we calculate a configuration of particles that best matches this pair-correlation?

These research goals will enhance our understanding of wave interactions with particulate materials under challenging conditions and will open new research avenues, not only for more precise and effective material sensing techniques but also for the design of materials with specific properties.

1.4 Relevance & Importance

Understanding how acoustic or electromagnetic waves behave in materials with random microstructure, that is, explaining how waves interact with these complex materials, is a crucial step in characterising the properties of these materials and designing novel materials with specific behaviours. The behaviour of these materials often depends on the physical properties of their constituent particles, such as their size and density. These factors are carried out across a wide range of industries and have a direct influence on various material properties such as the dissolution rate of a tablet or the flow and mix properties of the powder particles [57, 70]. Advancements in mechanical engineering can be made by designing the next generation of sound absorbing materials to control wave propagation. Additionally, since all materials scatter light and sound and by extension, waves, either acoustic or electromagnetic, can be used for non-invasive and energy-efficient sensing of particulate materials.

Measuring particle size and density and understanding how they affect many products and processes, could optimise the efficiency of the manufacturing processes

and enhance the quality of the product [10, 24, 31]. Nowadays, laser diffraction is the state of the art technique for characterising the properties of a particulate material [12, 50, 73, 80]. Many organisations around the world, such as Malvern Panalytical [38], Horiba [30], and Microtrac [42] use this technique. It involves projecting a laser through a dispersed particulate material and measuring the angle and intensity of the light scattering, which reveals particle size. However, this method assumes that the incident light interacts with only one particle before it is detected. In high-density materials, the incident light may interact with multiple particles before reaching the detector. This interaction can alter the properties (angle, intensity) of the detected light. This may lead to misinterpretation of the light's properties by the instrument. That is one reason why the material is diluted before the process of laser diffraction begins.

Let us now consider a scenario where we run a pharmaceutical company that processes powders, typically transported through pipes. Despite laser diffraction being the leading method for analysis, there are limitations, particularly in understanding the microstructure of the powder in its natural state. Here we ask: What if we could implement a method that does not require diluting the powder or using laser diffraction? What if we could exploit the multiple scattering of waves and design a sensor that can determine the statistical properties of the powder particles in real time? This device would operate by emitting and receiving waves - mechanical, sound or electromagnetic - tailored on the powder's nature. As these waves interact with the powder, they generate multiple scattering patterns. By analysing these scattering patterns, we could reveal detailed insights into the particle size and density. This innovative approach has the potential to provide real-time monitoring of the powder, offering a significant advantage over traditional methods.

As an analogy, we solve the multiple scattering problem and compute the total scattered wave through the use of the Julia packages *MultipleScattering.jl* [27] and *EffectiveWaves.jl* [29]. These tools allow us to generate large and reliable datasets from different scattering simulations. The scattering coefficients from the particulate material can be obtained and numerical methods - such as Supervised Machine Learning techniques - can be applied to extract information on the particulate (e.g. particle size and density) [16, 24, 59, 63]. This approach can start with basic methods such as linear regression and move on with more sophisticated models that are able to capture more complicated relationships between the scattering coefficients, and the average and standard deviation of the different species of particles. Thus, this large amount of data is essential to understand how to sense and design materials in order

to control waves.

1.5 Overview of the dissertation

In Chapter 2, we demonstrate that the average transmitted wave is a sum of effective waves when propagating beyond one inter-particle correlation length away from the boundary. This finding is critical, as our goal is to verify the existence of these waves and conduct Monte-Carlo simulations.

Chapter 3 enhances our understanding of the main concepts presented in Chapter 2 but also paves the way for the advanced methods discussed in Chapter 4. To elaborate, Section 3.1 focuses on the effects of multiple effective wavenumbers on reflection coefficients. Section 3.2 introduces an asymptotic method for determining effective wavenumbers in three dimensions, particularly in scenarios involving monopole scatterers. Section 3.3 focuses on the challenges in Monte-Carlo simulation when simulating particle configurations in finite regions and sets the stage for Chapter 4.

Chapter 4 demonstrates how to calculate particle configurations from a given pair-correlation. This is not only useful when comparing theoretical results to Monte-Carlo simulations, but also in material design: changing the pair-correlation affects many of the average properties (thermal, chemical, fluid flow) of a material. To either make the material, or determine if it is feasible, we need to calculate a configuration of particles from the pair-correlation. Consequently, our primary goal is to tackle both of these objectives by focusing on the study of techniques for deriving particle configurations from pair-correlations and vice-versa. We also aim to introduce advanced techniques in smooth nonlinear optimisation, demonstrating how these can be applied to rapidly deduce particle configurations from known pair-correlations.

In Chapter 5 we give a brief summary of the key findings from our research and explore potential future directions for further work.

References

[1] BS ISO 20998-3:2017. *London: British Standards Institution*. 2017. URL: https://www.iso.org/obp/ui/en/#iso:std:iso:20998:-3:ed-1:v1:en.

[2] Ian D. Abrahams et al. 'The effective material properties of a composite elastic half-space'. In: *Journal of the Acoustical Society of America* 139 (Apr. 2016), 2151–2151. URL: http://dx.doi.org/10.1121/1.4950359.

[3] J. R. Allegra et al. 'Attenuation of Sound in Suspensions and Emulsions: Theory and Experiments'. In: *The Journal of the Acoustical Society of America* 51.5B (May 1972), 1545–1564. URL: http://dx.doi.org/10.1121/1.1912999.

[4] Vincent C. Ballenegger et al. 'The Ewald-Oseen extinction theorem and extinction lengths'. In: *American Journal of Physics* 67.7 (July 1999), pp. 599–605. URL: https://doi.org/10.1119/1.19330.

[5] J.A. Barker et al. 'Monte Carlo values for the radial distribution function of a system of fluid hard spheres'. In: *Molecular Physics* 21.1 (Jan. 1971), 187–191. URL: http://dx.doi.org/10.1080/00268977100101331.

[6] James G. Berryman. 'Long-wavelength propagation in composite elastic media I. Spherical inclusions'. In: *The Journal of the Acoustical Society of America* 68.6 (Dec. 1980), 1809–1819. URL: http://dx.doi.org/10.1121/1.385171.

[7] Max Born et al. *Principles of Optics: 60th Anniversary Edition*. Cambridge University Press, Dec. 2019. URL: http://dx.doi.org/10.1017/9781108769914.

[8] J. J. Bowman et al. *Electromagnetic and acoustic scattering by simple shapes (Revised edition)*. 1987.

[9] V.V. Bringi et al. 'The effects on pair correlation function of coherent wave attenuation in discrete random media'. In: *IEEE Transactions on Antennas and Propagation* 30.4 (July 1982), pp. 805–808. URL: https://doi.org/10.1109/tap.1982.1142852.

[10] R E Challis et al. 'Ultrasound techniques for characterizing colloidal dispersions'. In: *Reports on Progress in Physics* 68.7 (June 2005), pp. 1541–1637. URL: https://doi.org/10.1088/0034-4885/68/7/r01.

[11] Mathieu Chekroun et al. 'Time-domain numerical simulations of multiple scattering to extract elastic effective wavenumbers'. In: *Waves in Random and Complex Media* 22.3 (Aug. 2012), 398–422. URL: http://dx.doi.org/10.1080/17455030.2012.704432.

[12] Dong Chen et al. 'A New Angular Light Scattering Measurement of Particulate Matter Mass Concentration for Homogeneous Spherical Particles'. In: *Sensors* 19.10 (May 2019), p. 2243. URL: http://dx.doi.org/10.3390/s19102243.

[13] Cilas. *Particle Size and Shape Analysis in Paint, Ink and Pigment Industry*. 2022. URL: http://www.bruben.com.ar/pdf/Aplicaciones/020-pigmentos%20paint%20industry.pdf.

[14] O. Costin et al. 'On the Construction of Particle Distributions with Specified Single and Pair Densities'. In: *The Journal of Physical Chemistry B* 108.51 (Oct. 2004), pp. 19614–19618. URL: https://doi.org/10.1021/jp047793m.

[15] Jenness Crawford et al. 'Aspects of correlation function realizability'. In: *The Journal of Chemical Physics* 119.14 (Sept. 2003), pp. 7065–7074. URL: https://doi.org/10.1063/1.1606678.

[16] Antonio Di Noia et al. *Neural Networks and Support Vector Machines and Their Application to Aerosol and Cloud Remote Sensing: A Review*. Springer International Publishing, 2018, 279–329. URL: http://dx.doi.org/10.1007/978-3-319-70796-9_4.

[17] J Dubois et al. 'Coherent acoustic response of a screen containing a random distribution of scatterers: Comparison between different approaches'. In: *Journal of Physics: Conference Series* 269 (Jan. 2011), p. 012004. URL: https://doi.org/10.1088/1742-6596/269/1/012004.

[18] P. P. Ewald. 'Zur Begründung der Kristalloptik'. In: *Annalen der Physik* 354.1 (1916), pp. 1–38. URL: https://doi.org/10.1002/andp.19163540102.

[19] Leslie L. Foldy. 'The Multiple Scattering of Waves. I. General Theory of Isotropic Scattering by Randomly Distributed Scatterers'. In: *Physical Review* 67.3-4 (Feb. 1945), pp. 107–119. URL: https://doi.org/10.1103/physrev.67.107.

[20] M. Ganesh et al. 'A far-field based T-matrix method for two dimensional obstacle scattering'. en. In: *ANZIAM Journal* 51.0 (May 2010), pp. 215–230. URL: https://journal.austms.org.au/ojs/index.php/ANZIAMJ/article/view/2581 (visited on 23/03/2018).

[21] M. Ganesh et al. 'Algorithm 975: TMATROM—A T-Matrix Reduced Order Model Software'. In: *ACM Trans. Math. Softw.* 44.1 (July 2017), 9:1–9:18. URL: http://doi.acm.org/10.1145/3054945 (visited on 23/03/2018).

[22] J de Goede et al. 'On the extinction theorem in electrodynamics'. In: *Physica* 58.4 (Apr. 1972), pp. 568–584. URL: https://doi.org/10.1016/0031-8914(72)90212-1.

[23] Artur L. Gower et al. 'A proof that multiple waves propagate in ensemble-averaged particulate materials'. In: *Proceedings of the Royal Society A: Mathematical, Physical and Engineering Sciences* 475.2229 (Sept. 2019), p. 20190344. URL: http://dx.doi.org/10.1098/rspa.2019.0344.

[24] Artur L. Gower et al. 'Characterising particulate random media from near-surface backscattering: A machine learning approach to predict particle size and concentration'. In: *EPL (Europhysics Letters)* 122.5 (July 2018), p. 54001. URL: http://dx.doi.org/10.1209/0295-5075/122/54001.

[25] Artur L Gower et al. 'Effective waves for random three-dimensional particulate materials'. In: *New Journal of Physics* 23.6 (June 2021), p. 063083. URL: http://dx.doi.org/10.1088/1367-2630/abdfee.

[26] Artur L. Gower et al. 'Multiple Waves Propagate in Random Particulate Materials'. In: *SIAM Journal on Applied Mathematics* 79.6 (Jan. 2019), 2569–2592. URL: http://dx.doi.org/10.1137/18M122306X.

[27] Artur L Gower et al. 'MultipleScatering.jl: A Julia library for simulating, processing, and plotting multiple scattering of waves.' In: *github.com/JuliaWaveScattering/MultipleScattering.jl* (2020).

[28] Artur L. Gower et al. 'Reflection from a multi-species material and its transmitted effective wavenumber'. en. In: *Proc. R. Soc. A* 474.2212 (Apr. 2018), p. 20170864. URL: http://rspa.royalsocietypublishing.org/content/474/2212/20170864 (visited on 22/04/2018).

[29] Artur Lewis Gower. 'EffectiveWaves.jl: A Julia package to calculate ensemble averaged waves in heterogeneous materials'. Version 0.3.4. In: *github.com/JuliaWaveScattering/EffectiveWaves.jl* (Dec. 2018).

[30] *Horiba Scientific - Dynamics Light Scattering*. URL: https://www.horiba.com/int/scientific/technologies/dynamic-light-scattering-dls-particle-size-distribution-analysis/.

[31] Turner JA Hu P. 'Contribution of double scattering in diffuse ultrasonic backscatter measurements'. In: *J Acoust Soc Am.* 137(1) (2015). URL: http://dx.doi.org/10.1103/PhysRevLett.108.058301.

[32] Yao Huang et al. 'Tailoring the electrical and thermal conductivity of multi-component and multi-phase polymer composites'. In: *International Materials Reviews* 65.3 (Mar. 2019), pp. 129–163. URL: https://doi.org/10.1080/09506608.2019.1582180.

[33] Akira Ishimaru. *Wave propagation and scattering in random media: Single scattering and transport theory v. 1*. San Diego, CA: Academic Press, Feb. 1978.

[34] Jaison Jeevanandam et al. 'Review on nanoparticles and nanostructured materials: history, sources, toxicity and regulations'. In: *Beilstein Journal of Nanotechnology* 9 (Apr. 2018), pp. 1050–1074. URL: https://doi.org/10.3762/bjnano.9.98.

[35] Gerhard Kristensson et al. *Multiple scattering by a collection of randomly located obstacles Part IV: The effect of the pair correlation function*. English. Vol. TEAT-7272. Technical Report LUTEDX/(TEAT-7272)/1-23/(2021). 2021. URL: https://portal.research.lu.se/en/publications/multiple-scattering-by-a-collection-of-randomly-located-obstacles-8.

[36] T. Kuna et al. 'Realizability of Point Processes'. In: *Journal of Statistical Physics* 129.3 (Sept. 2007), pp. 417–439. URL: https://doi.org/10.1007/s10955-007-9393-y.

[37] C. M. Linton et al. 'Multiple scattering by random configurations of circular cylinders: Second-order corrections for the effective wavenumber'. en. In: *J. Acoust. Soc. Am.* 117.6 (2005), p. 3413. URL: http://scitation.aip.org/content/asa/journal/jasa/117/6/10.1121/1.1904270 (visited on 04/09/2016).

[38] *Malvern Panalytical - Laser Diffraction*. URL: https://www.malvernpanalytical.com/en/products/technology/light-scattering/laser-diffraction.

[39] P. A. Martin. 'Multiple Scattering: an Invitation'. In: *Third International Conference on Mathematical and Numerical Aspects of Wave Propagation*. Ed. by G. Cohen. Philadelphia: SIAM, 1995, pp. 3–16.

[40] P. A. Martin. *Multiple Scattering: Interaction of Time-Harmonic Waves with N Obstacles*. Cambridge University Press, Aug. 2006. URL: http://dx.doi.org/10.1017/CBO9780511735110.

[41] P. A. Martin et al. 'Estimating the dynamic effective mass density of random composites'. In: *The Journal of the Acoustical Society of America* 128.2 (Aug. 2010), pp. 571–577. URL: https://doi.org/10.1121/1.3458849.

[42] *Microtrac MRB - Particle Characterisation*. URL: https://www.microtrac.com.

[43] M.I. Mishchenko et al. 'Peter Waterman and T-matrix methods'. In: *Journal of Quantitative Spectroscopy and Radiative Transfer* 123 (July 2013), pp. 2–7. URL: https://doi.org/10.1016/j.jqsrt.2012.10.025.

[44] Michael I. Mishchenko. 'Coherent backscattering by two-sphere clusters'. In: *Optics Letters* 21.9 (May 1996), p. 623. URL: http://dx.doi.org/10.1364/OL.21.000623.

[45] Michael I. Mishchenko. *Electromagnetic Scattering by Particles and Particle Groups: An Introduction*. Cambridge University Press, Apr. 2014. URL: http://dx.doi.org/10.1017/CBO9781139019064.

[46] Michael I. Mishchenko et al. *Multiple Scattering of Light by Particles: Radiative Transfer and Coherent Backscattering*. Cambridge University Press, 2006. 518 pp.

[47] Michael I. Mishchenko et al. 'T-matrix computations of light scattering by nonspherical particles: A review'. In: *J. Quant. Spectrosc. Radiat. Transfer*. Light Scattering by Non-Spherical Particles 55.5 (May 1996), pp. 535–575. URL: http://www.sciencedirect.com/science/article/pii/0022407396000027.

[48] Rana Nandi et al. 'Transport Properties of the Nuclear Pasta Phase with Quantum Molecular Dynamics'. In: *The Astrophysical Journal* 852.2 (Jan. 2018), p. 135. URL: https://doi.org/10.3847/1538-4357/aa9f12.

[49] K. K. Napal et al. 'Effective T-matrix of a cylinder filled with a random 2 dimensional particulate'. In: (2023). URL: https://arxiv.org/abs/2308.13338.

[50] Robert T. Nishida et al. 'A Simple Method for Measuring Fine-to-Ultrafine Aerosols Using Bipolar Charge Equilibrium'. In: *ACS Sensors* 5.2 (Jan. 2020), 447–453. URL: http://dx.doi.org/10.1021/acssensors.9b02143.

[51] C. W. Oseen. 'Über die Wechselwirkung zwischen zwei elektrischen Dipolen und üer die Drehung der Polarisationsebene in Kristallen und Flüssigkeiten'. In: *Annalen der Physik* 353.17 (1915), pp. 1–56. URL: https://doi.org/10.1002/andp.19153531702.

[52] W. J. Parnell et al. 'Effective Properties of a Composite Half-Space: Exploring the Relationship Between Homogenization and Multiple-Scattering Theories'. In: *The Quarterly Journal of Mechanics and Applied Mathematics* 63.2 (Apr. 2010), 145–175. URL: http://dx.doi.org/10.1093/qjmam/hbq002.

[53] William J. Parnell et al. 'Multiple point scattering to determine the effective wavenumber and effective material properties of an inhomogeneous slab'. In: *Waves in Random and Complex Media* 20.4 (Nov. 2010), pp. 678–701. URL: https://doi.org/10.1080/17455030.2010.510858.

[54] D.N. Pattanayak et al. 'General form and a new interpretation of the Ewald-Oseen extinction theorem'. In: *Optics Communications* 6.3 (Nov. 1972), pp. 217–220. URL: https://doi.org/10.1016/0030-4018(72)90178-2.

[55] Allan D. Pierce. *Acoustics: An Introduction to Its Physical Principles and Applications*. Springer International Publishing, 2019. URL: http://dx.doi.org/10.1007/978-3-030-11214-1.

[56] Roy Pike. 'Particle Sizing by Laser Light Scattering'. In: (2002), 895–919. URL: http://dx.doi.org/10.1016/b978-012613760-6/50048-6.

[57] 'Powder Technology: Fundamentals of Particles, Powder Beds, and Particle Generation'. In: (Nov. 2006). URL: http://dx.doi.org/10.1201/9781420044119.

[58] Wohlers Report. '3D Printing and Additive Manufacturing State of the Industry'. In: *Annual Worldwide Progress Report, ASTM International: Denver, CO, USA* (2020).

[59] Matthias Rupp et al. 'Fast and Accurate Modeling of Molecular Atomization Energies with Machine Learning'. In: *Physical Review Letters* 108.5 (Jan. 2012). URL: http://dx.doi.org/10.1103/PhysRevLett.108.058301.

[60] Kunio Shinohara. 'Fundamental and Rheological Properties of Powders'. In: (1997), pp. 96–145. URL: https://doi.org/10.1007/978-1-4615-6373-0_4.

[61] Alverède Simon et al. 'Propagation of coherent shear waves in scattering elastic media'. In: *Physical Review E* 103.5 (May 2021). URL: https://doi.org/10.1103/physreve.103.l051001.

[62] J. J. Stoker. 'On radiation conditions'. In: *Communications on Pure and Applied Mathematics* 9 (1956), pp. 577–595. URL: https://api.semanticscholar.org/CorpusID:119513891.

[63] Peter D. Thorne et al. 'An overview on the use of backscattered sound for measuring suspended particle size and concentration profiles in non-cohesive inorganic sediment transport studies'. In: *Continental Shelf Research* 73 (Feb. 2014), pp. 97–118. URL: https://doi.org/10.1016/j.csr.2013.10.017.

[64] Victor P. Tishkovets et al. 'Scattering of electromagnetic waves by ensembles of particles and discrete random media'. In: *Journal of Quantitative Spectroscopy and Radiative Transfer* 112.13 (Sept. 2011), pp. 2095–2127. URL: https://doi.org/10.1016/j.jqsrt.2011.04.010.

[65] S. Torquato et al. 'Controlling the Short-Range Order and Packing Densities of Many-Particle Systems'. In: *The Journal of Physical Chemistry B* 106.33 (July 2002), pp. 8354–8359. URL: https://doi.org/10.1021/jp0208687.

[66] S Torquato et al. 'Random Heterogeneous Materials: Microstructure and Macroscopic Properties'. In: *Applied Mechanics Reviews* 55.4 (July 2002), B62–B63. URL: https://doi.org/10.1115/1.1483342.

[67] L. Tsang et al. 'Multiple scattering of acoustic waves by random distribution of discrete spherical scatterers with the quasicrystalline and Percus–Yevick approximation'. In: *The Journal of the Acoustical Society of America* 71.3 (Mar. 1982), 552–558. URL: http://dx.doi.org/10.1121/1.387524.

[68] Leung Tsang et al. *Scattering of Electromagnetic Waves: Numerical Simulations*. Wiley, May 2001. URL: http://dx.doi.org/10.1002/0471224308.

[69] O.U. Uche et al. 'On the realizability of pair correlation functions'. In: *Physica A: Statistical Mechanics and its Applications* 360.1 (Jan. 2006), pp. 21–36. URL: https://doi.org/10.1016/j.physa.2005.03.058.

[70] Ugur Ulusoy. 'A Review of Particle Shape Effects on Material Properties for Various Engineering Applications: From Macro to Nanoscale'. In: *Minerals* 13.1 (Jan. 2023), p. 91. URL: https://doi.org/10.3390/min13010091.

[71] B J Uscinski. *Elements of wave propagation in random media*. en. New York, NY: McGraw-Hill, Nov. 1977.

[72] V. K. Varadan et al. 'Multiple scattering theory for waves in discrete random media and comparison with experiments'. In: *Radio Science* 18.3 (May 1983), pp. 321–327. URL: https://doi.org/10.1029/rs018i003p00321.

[73] Konstantina Vasilatou et al. 'Calibration of optical particle size spectrometers against a primary standard: Counting efficiency profile of the TSI Model 3330 OPS and Grimm 11-D monitor in the particle size range from 300nm to 10μm'. In: *Journal of Aerosol Science* 157 (2021), p. 105818. URL: https://www.sciencedirect.com/science/article/pii/S0021850221005498.

[74] P. C. Waterman et al. 'Multiple Scattering of Waves'. In: *Journal of Mathematical Physics* 2.4 (July 1961), pp. 512–537. URL: https://doi.org/10.1063/1.1703737.

[75] P.C. Waterman. 'Matrix formulation of electromagnetic scattering'. In: *Proceedings of the IEEE* 53.8 (1965), pp. 805–812. URL: https://doi.org/10.1109/proc.1965.4058.

[76] G. N. Watson. *A Treatise on the Theory of Bessel Functions*. University Press, Cambridge, 1944.

[77] Robert Weser et al. 'Particle characterisation in highly concentrated dispersions using ultrasonic backscattering method'. In: *Ultrasonics* 53.3 (Mar. 2013), 706–716. URL: http://dx.doi.org/10.1016/j.ultras.2012.10.013.

[78] J. R. Willis. 'Transmission and reflection of energy at the boundary of a random two-component composite'. In: *Proceedings of the Royal Society A: Mathematical, Physical and Engineering Sciences* 479.2271 (Mar. 2023). URL: http://dx.doi.org/10.1098/rspa.2022.0730.

[79] Emil Wolf. 'A generalized extinction theorem and its role in scattering theory'. In: *Coherence and Quantum Optics: Proceedings of the Third Rochester Conference on Coherence and Quantum Optics held at the University of Rochester, June 21–23, 1972*. Springer. 1973, pp. 339–357.

[80] Renliang Xu. 'Light scattering: A review of particle characterization applications'. In: *Particuology* 18 (Feb. 2015), 11–21. URL: http://dx.doi.org/10.1016/j.partic.2014.05.002.

[81] Ge Zhang et al. 'Realizable hyperuniform and nonhyperuniform particle configurations with targeted spectral functions via effective pair interactions'. In: *Physical Review E* 101.3 (Mar. 2020). URL: https://doi.org/10.1103/physreve.101.032124.

[82] Maciej Zworski. 'Mathematical study of scattering resonances'. In: *Bulletin of Mathematical Sciences* 7.1 (Mar. 2017), pp. 1–85. URL: https://doi.org/10.1007/s13373-017-0099-4.

Chapter 2

The average transmitted wave in random particulate materials

ARISTEIDIS KARNEZIS, PAULO S. PIVA, ART L. GOWER

Abstract

Microwave remote sensing is significantly altered when passing through clouds or dense ice. This phenomenon is not unique to microwaves; for instance, ultrasound is also disrupted when traversing through heterogeneous tissues. Understanding the average transmission in particle-filled environments is central to improve data extraction or even to create materials that can selectively block or absorb certain wave frequencies. Most methods that calculate the average transmitted field assume that it satisfies a wave equation with a complex effective wavenumber. However, recent theoretical work has predicted more than one effective wave propagating even for scalar waves propagating in statistically isotropic media. In this work we provide the first clear evidence of these predicted multiple effective waves by using high-fidelity Monte-Carlo simulations that do not make any statistical assumptions. To achieve this, it was necessary to fill in a missing link in the theory for particulate materials. To this end, we prove that the incident wave does not propagate throughout the material, which is usually taken as an assumption called the *Ewald-Oseen extinction theorem*. By proving this we conclude that the extinction length - the distance it takes for the incident wave to be extinct - is equal to the correlation length between the particles.

2.1 Introduction

Most materials, at some length scale, are formed of a random configuration of smaller particles. Consider particles in powder for pharmaceuticals, grains of sand, oil droplets in emulsions, and aggregates in solid composites. The wide number of these particulate materials, and their associated engineering applications, make it worthwhile developing methods to characterise these materials and design them intelligently.

Background. When it comes to measurement and characterisation of particulate materials, the main tools are classical waves such as electromagnetic and ultrasonic or acoustic. The governing equations for these classical waves would be well-understood if the material itself was known in all its details. Unfortunately, in most cases it is impossible to know in detail the microstructure of the material because it is disordered. In these scenarios, ensemble averaging and statistical assumptions need to be employed to obtain solvable systems [20, 33, 34, 47].

The interaction of classical waves with particulate materials (on average) is well-understood within certain limits. In the long-wavelength limit, where the particles appear small compared to the wavelength of the incident wave, it is well-understood how to calculate effective properties [42]. In the dilute limit, where there is no multiple scattering, Mie theory has led to characterisation methods such as Dynamic Light Scattering and laser diffraction resulted in a range of widely used tools*†.

Pushing the limits. In the cases where multiple scattering is significant, and the incident wavelength is not long (compared to the microstructure), the average wave is not as simple to describe [7, 15, 29]. This is especially true when using exotic pair-correlations [41, 43] and resonant particles [28, 37]. To push the theory to these new limits, we need to clearly understand the validity of all the assumptions made. Within this context, we aim to address two significant assumptions that currently remain unanswered.

Multiple effective wavenumbers. Most of the literature assumes there is only one effective wavenumber [9, 10, 27, 31, 40, 44, 48]. As the medium is isotropic and homogeneous (after ensemble averaging) it seems reasonable to assume that there is only one effective wavenumber $k_\star$ for waves travelling in a bulk material (i.e. no waveguide). However, two different theoretical methods [15, 50] have predicted that there exist at least two (complex) effective wavenumbers for one fixed frequency. Here we give the first clear numerical evidence of these multiple effective wavenumbers

*Malvern Panalytical: www.malvernpanalytical.com/laser-diffraction
†Horiba Scientific: www.horiba.com/dynamic-light-scattering

as well as demonstrate that multiple wavenumbers are triggered by particles, and frequencies, that lead to strong scattering. To clearly relate the transmitted field from numerical simulations with the transmitted wave from theoretical results, we have to first be clear on what the most general theoretical framework predicts about the transmitted field.

Incident wave extinction. It is often assumed that the incident wave does not propagate, or contribute to, the total transmitted field inside a material. This assumption is called the *Ewald-Oseen extinction theorem* [7, 11], and is applied more broadly than on just averaged disordered or random materials. For disordered particulate material, this assumption has been derived in many different limits, including low-frequency and low particle volume fraction [4], but there are still disagreements in the literature on the exact extinction length [4], that is, the distance into the medium that the incident waves travels before vanishing. Knowledge of the exact extinction length is required, for example, in experiments where the source and transmitted wave can be mixed. This situation arises when measuring light from objects at astronomical distances [4].

In this work we are able to prove that for any particulate material geometry, frequency, and incident wave, the Ewald-Oseen extinction theorem is a result of more fundamental assumptions. With the proof, we can clearly demonstrate that the incident wave does not propagate further than the correlation length between the particles. That is, the extinction length is equal to the inter-particle correlation length.

Microscopic extinction. The theoretical methods we use consider the scattering from all particles and take an ensemble average. This has been called the microscopic approach [25, 33, 40, 44, 46]. The microscopic approach solves the boundary conditions around every particle, and the resulting equations involve terms which satisfy the background wave equation, just like the incident wave. Cancelling these terms is often called the Ewald-Oseen extinction theorem [5], but it is not the same as concluding that the incident wave itself is extinct, see for example [30, 32]. Further, this cancellation does not lead to the extinction length. We are able to connect the two approaches by showing that the boundary conditions around each particle, used in the microscopic approach, do lead to the incident wave itself being extinct, and provide an extinction length.

Monte-Carlo. There have been several studies that use Monte-Carlo methods to validate effective wave theory. Examples include comparing Monte-Carlo with: the average scattering from a sphere filled with particles [36, 53], and one effective wavenumber from the theory [8, 9]. To our knowledge, there has been no Monte-Carlo

validation or evidence that more than one multiple effective wavenumber exists. Here, by using precise Monte-Carlo simulations, we provide the first clear evidence that at least two effective wavenumbers, and therefore two effective waves, are present in the transmitted field. The theoretical methods that predict these multiple effective wavenumbers make several statistical assumptions, whereas our numerical simulations make no such assumptions. They, therefore, provide a clear validation of the theoretical predictions.

Summary of the paper. In Section 2.1.1 we provide an overview of the theory and the results of this paper. In Section 2.2 we discuss what the theory predicts for the average wave in a plate filled with random particles and how to easily identify when multiple wavenumbers should appear. In Section 2.3 we discuss our Monte-Carlo simulations, which involve simulating waves scattered from tens of thousands of particle configurations, how we verify convergence, and how we clearly demonstrate that there are scenarios where at least two effective wavenumbers appear in the transmitted field. In Section 2.4 we provide rigorous derivations that: the incident wave does not propagate in the particulate material, and the average transmitted wave is a sum of waves which satisfy effective wave equations. Our derivations are more general than just for a plate, they hold for a finite region, and in fact for any spatial dimension. So the proof we provide is also valid for three-dimensional materials.

2.1.1 Overview of the theory

Consider a harmonic incident plane-wave $u_{\text{inc}}(x) = \mathrm{e}^{\mathrm{i}kx}$, satisfying the Helmholtz equation with wavenumber k, so that $u_{\text{inc}}(x)\mathrm{e}^{-\mathrm{i}\omega t}$ satisfies a scalar wave equation, where x is the distance of propagation. When this incident wave propagates through a random particulate medium, the general assumption has been that it will be replaced by one effective wave of the form:

$$\langle u(x)\rangle = A_\star \mathrm{e}^{\mathrm{i}k_\star x}, \tag{2.1}$$

where $k_\star$ is a complex effective wavenumber, for the fixed frequency ω, $A_\star$ is the average transmission coefficient, and $\langle u(x)\rangle$ is the ensemble average of $u(x)$ over all possible particle configurations [10, 27, 31, 40, 44, 48].

In the low-frequency limit, when the particles are small relative to the incident wave- length, there is substantial evidence to justify (2.1). But beyond the low-frequency limit, and when using more exotic pair-correlations and distributions for the particles, there is no clear consensus. Two different methods [16, 50] suggest a

different form for (2.1) given by:

$$\langle u(x)\rangle = A_{\text{inc}}\mathrm{e}^{\mathrm{i}kx} + \sum_{p=1}^{\infty} A_p \mathrm{e}^{\mathrm{i}k_p x}, \tag{2.2}$$

where A_{inc} is the amplitude of the incident wave, A_p are the average transmission coefficients and k_p are complex effective wavenumbers. In the next two paragraphs we further explain the form (2.37).

Incident wave extinction. When A_{inc} is not zero, a part of the incident wave remains even when propagating through a random particulate. The work by Martin [30] suggests that this is the case. Assuming $A_{\text{inc}} = 0$ is called the Ewald-Oseen extinction theorem [11, 25, 40], and it is due to the scattering and absorption of energy by the random distribution of particles. Much of the literature [4] assumes this extinction happens after the incident wave has propagated a certain distance in the material. In this paper we prove that for any: frequency, material geometry, particle distribution, and for two and three spatial dimensions, the incident wave is extinct ($A_{\text{inc}} = 0$ for plane-waves) at a distance equal to particle correlation length.

Multiple effective wavenumbers. Each term in the sum of (2.2) represents an effective wave with a different wavenumber k_p. This is highly unusual for scalar waves at a fixed angular frequency ω. Yet, two different theoretical methods have predicted the existence of at least two ($p > 1$) complex effective wavenumbers [16, 38, 50]. The evidence for this unusual prediction, beyond just theoretical, is lacking. In this work we use highly accurate simulations and Monte-Carlo method for circular cylindrical particles to demonstrate that these extra wavenumbers are present for specific frequencies. To our knowledge, this is the first clear evidence of the existence of these multiple effective wavenumbers.

Average reflected field. Beyond just curiosity, these extra effective wavenumbers can have a significant effect on the average reflected, transmitted, or scattered wave from a particulate material [14, 16]. It is also far simpler to calculate the cases where there is only one dominant wavenumber [10, 15].

To understand when these multiple wavenumbers are needed, we have produced a series of phase diagrams. A phase diagram in the field of acoustics is a graphical representation that shows how the acoustic properties of a material change. By mapping these properties against frequency and volume fraction, we can optimise materials for specific acoustic applications, such as soundproofing or ultrasonic imaging, by identifying the conditions under which the material's acoustic response is most favourable for the intended application. An example is shown in Figure 2.1 for sound-soft

particles. The regions with a light colour, corresponding to values below 0.5 shown in the colour bar, require more than one effective wavenumber to accurately describe the transmitted field. For example, we can see that only one wavenumber is needed for low particle volume fraction $\phi < 0.1$, with only one exception around $ka = 0.6$. The green curve in the figure shows the scattering strength of just one particle by itself. Surprisingly, we see that the frequencies at which the single particle scatters the strongest (the peaks in the green curve) are also the frequencies at which two (or more) effective wavenumbers are required, and therefore needed to accurately describe wave transmission. In other words, strong scattering leads to multiple effective wavenumbers. These results, and other phase diagrams, are further discussed in Section 2.3.1.

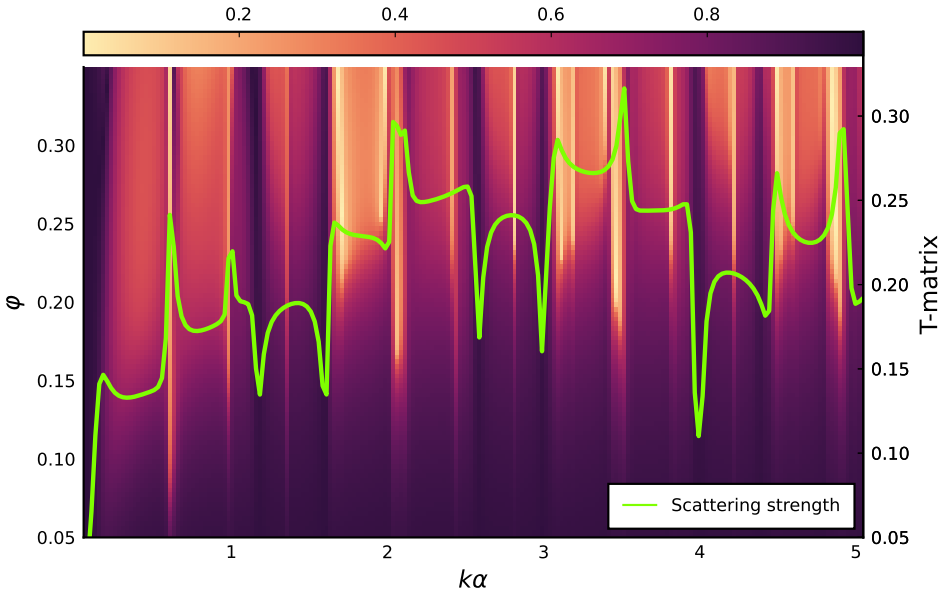

Figure 2.1: The phase diagram for sound-soft $(\rho_o, c_o = 0.30)$ particles showing when more than one effective wavenumber is needed. The x–axis shows ka, with a being the particle radius, and k being the incident wavenumber. The y–axis is the particle volume fraction ϕ. The regions with a light colour in the background, anything less than approximately 0.5 shown in the colour bar, require more than one effective wavenumber. The height of the green curve is the scattering strength of just one particle (given by (2.18)).

2.2 A plate filled with particles

For a medium that is isotropic and homogeneous, it seems reasonable to assume that there is only one effective wavenumber for one fixed angular frequency ω. However, recently two different theoretical models have predicted that there exist at least two (complex) effective wavenumbers [16, 50].

Here we design a computational experiment to give clear evidence of at least two of these effective wavenumbers. We do this by using a robust numerical method based on high-fidelity Monte-Carlo simulations for two-dimensional disks.

To describe the material, let $\mathcal{P}_j$ be the disk occupied by the j-th particle, as represented by the circles in Figure 2.2 and shown in more detail in Figure 2.10. Let $\mathcal{P} = \cup_j \mathcal{P}_j$ be the union of all particles. For simplicity we consider circular particles of equal size. In other words, using standard set-builder notation:

$$\mathcal{P}_j = \{\boldsymbol{r} \in \mathbb{R}^2 : \ |\boldsymbol{r} - \boldsymbol{r}_j| < a\}, \tag{2.3}$$

where a is the radius of the particle, centred at $\boldsymbol{r}_j$, and $|\boldsymbol{x}|$ is the length of the vector $\boldsymbol{x}$.

The particles are restricted inside the plate geometry $\mathcal{R}$, given by:

$$\mathcal{R} = \left\{(x, y) \in \mathbb{R}^2 : 0 \leq x \leq W, \ -\frac{H}{2} \leq y \leq \frac{H}{2}\right\}, \tag{2.4}$$

where W is the width and H is the height of the plate as shown in Figure 2.2.

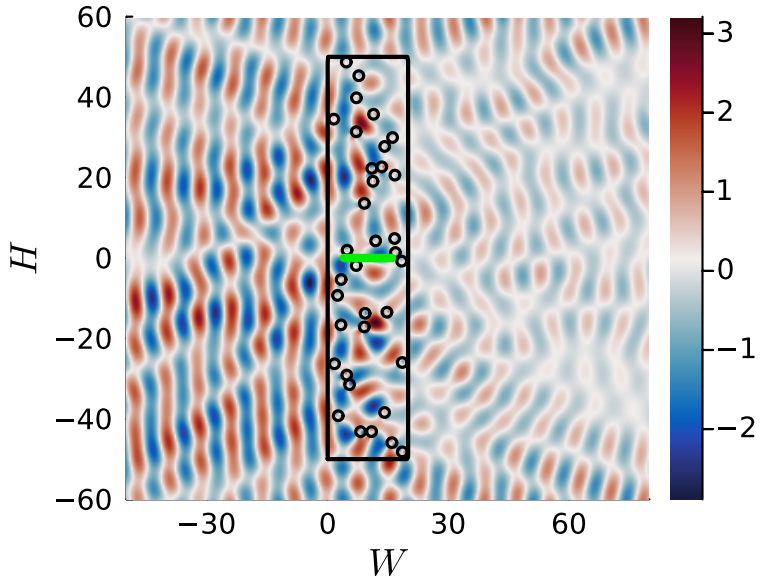

Figure 2.2: Scattering of an incident plane-wave approaching from the left, onto one specific configuration of randomly distributed circular cylinders (or particles) Λ. The particles with radius $a = 1.2$ are considered strong scatterers with density $\rho_0 = 0.30\ kg \cdot m^{-3}$ and wavespeed $c_0 = 0.30\ m \cdot s^{-1}$. The density and wavespeed of the background medium is $\rho = 1.0\ kg \cdot m^{-3}$ and $c = 1.0\ m \cdot s^{-1}$ respectively. To perform this simulation we choose a frequency $\omega = 0.8$ and a particle volume fraction $\phi = 8\%$. The solid black line depicts the plate boundary while the green line shows where the field is measured. The simulation directly solves the governing equations [31].

The total field $u(\boldsymbol{r})$ satisfies a Helmholtz equation which depends on whether $\boldsymbol{r}$ is inside a particle or not:

$$\nabla^2 u(\boldsymbol{r}) + k^2 u(\boldsymbol{r}) = 0, \qquad \text{for } \boldsymbol{r} \in \mathcal{R} \setminus \mathcal{P}, \tag{2.5}$$

$$\nabla^2 u(\boldsymbol{r}) + k_0^2 u(\boldsymbol{r}) = 0, \qquad \text{for } \boldsymbol{r} \in \mathcal{P}, \tag{2.6}$$

where $k = \frac{\omega}{c}$ and $k_0 = \frac{\omega}{c_0}$ are the real wavenumbers of the background and particles respectively. The scalars c and c_0 are, respectively, the wavespeeds in the background and particles.

The simplest scenario to numerically check for effective waves is for planar symmetry. As in this case each frequency has only one mode: the plane-wave. To achieve this, we fill a plate region with a configuration of identical, randomly distributed cylindrical particles whose positions are unknown, as shown in Figure 2.2.

2.2.1 Effective waves for planar symmetry

In this section we summarise the results of the theory for plane-wave symmetry. The results here will be compared with a Monte-Carlo method detailed in Section 2.3.

We consider an incident plane-wave of the form:

$$u_{\text{inc}}(x) = \mathrm{e}^{\mathrm{i}kx}, \tag{2.7}$$

and consider particles in a plate region $\mathcal{R}$ with an infinite height (unlike Figure 2.2 which shows a truncated plate with a finite height).

The theoretical methods consider an ensemble average of the total field u. To achieve this, we describe one configuration of identical particles with:

$$\Lambda = (\boldsymbol{r}_1, \boldsymbol{r}_2, \ldots, \boldsymbol{r}_J), \tag{2.8}$$

where $\boldsymbol{r}_j$ is the centre position of the particle $\mathcal{P}_j$. Naturally, the field u depends on the particle positions. To make this explicit we use $u(x; \Lambda)$.

Next, to calculate the ensemble average, we need to define the probability of all possible particle configurations. To do this, we introduce the joint probability density given by $\mathrm{p}(\Lambda)$. For a brief overview on the probability density function p, see [15, 18, 27]. The theoretical methods then calculate and predict the ensemble average defined by:

$$\langle u(x) \rangle := \int u(x; \Lambda) \mathrm{p}(\Lambda) \mathrm{d}\Lambda, \tag{2.9}$$

where the integral is over all possible particle positions, and the fields depend only on the spatial position x as we are considering planar symmetry.

It is widely assumed that the average $\langle u(x)\rangle$ satisfies a Helmholtz equation with a unique effective complex wavenumber k_* [10, 27, 31, 40, 44, 48]. In Section 2.4.1 we prove that $\langle u(x)\rangle$ is a sum of several effective waves, but only when x is deep enough within the material. To define what "deep enough" means we need to introduce the particle pair-correlation.

Pair-correlations. We assume that particles are distributed both homogeneously and isotropically, which leads to:

$$\mathrm{g}(|\boldsymbol{r}_1 - \boldsymbol{r}_2|) = \frac{\mathrm{p}(\boldsymbol{r}_1, \boldsymbol{r}_2)}{\mathrm{p}(\boldsymbol{r}_1)\mathrm{p}(\boldsymbol{r}_2)}, \tag{2.10}$$

for an infinite number of particles. For details on pair-correlations see [45].

For a disordered or random configuration of particles we have that:

$$\mathrm{g}(|\boldsymbol{r}_1 - \boldsymbol{r}_2|) = \begin{cases} 0, & \text{if} \quad |\boldsymbol{r}_1 - \boldsymbol{r}_2| \leq a_{12}, \\ 1, & \text{if} \quad |\boldsymbol{r}_1 - \boldsymbol{r}_2| \geq b_{12}, \end{cases} \tag{2.11}$$

where $b_{12} \geq a_{12} > 2a$. The distance a_{12} is the minimum allowed distance between the particles while b_{12} is called the correlation length. For the region $a_{12} \leq |\boldsymbol{r}_1 - \boldsymbol{r}_2| \leq b_{12}$ the pair-correlation can take any values for our calculation below, though we expect $\mathrm{g}(r)$ to be continuous in r. In this work we use two different pair-correlations. The first, and the simplest, is called *Hole-Correction*, which assumes that $b_{12} = a_{12}$. The second is called the *Percus-Yevick* approximation, which more accurately approximates the pair-correlation for particles that are distributed according to a uniform random probability, except no two particles can overlap [6, 24, 44, 45]. We use the results from [3] to obtain Percus-Yevick for disks. Figure 2.3 shows the Percus-Yevick distributions for several different particle volume fractions ϕ.

For disordered media we have that $\mathrm{g}(r) \to 1$ as $r \to \infty$. That is, particles become uncorrelated as they are further apart. To prove that $\langle u(x)\rangle$ is a sum of effective waves we need a slightly stronger assumption: that there is a distance b_{12} at which particles are completely uncorrelated as used in (2.11). Essentially, this means that the interactions between particles diminish or disappear, allowing us to consider their effects independently in mathematical models or numerical simulations.

Effective plane-waves. By having a length b_{12} at which particles become uncorrelated, we demonstrate in Section 2.4.1 that for an infinite plate geometry ($H \to \infty$

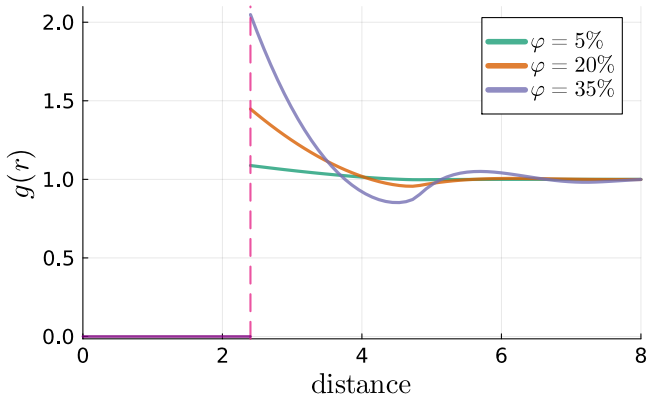

Figure 2.3: The Percus-Yevick approximation is a pair-correlation that represents particles that are uniformly randomly placed, except particles do not overlap. That is, particles do not attract or repel each other. The particle radius $a = 1.2$ and ϕ is the particle volume fraction.

in (2.4)) filled with particles:

$$\langle u(x)\rangle = \sum_{p=1}^{P} \left(A_p^+ \mathrm{e}^{\mathrm{i}k_p x} + A_p^- \mathrm{e}^{-\mathrm{i}k_p x}\right) \quad \text{for} \quad \left|x - \frac{W}{2}\right| < \frac{W}{2} - b_{12} - a, \tag{2.12}$$

where we used planar symmetry as shown in [15]. The $A_p^{\pm}$ are complex amplitudes, the k_p are the complex effective wavenumbers, and P is the number of effective wavenumbers. There is an infinite number of wavenumbers P, but according to theoretical calculations only a few are needed for accurate results. For a detailed discussion on these multiple effective wavenumbers see [14, 16].

The dispersion equation. To calculate the wavenumbers k_p we use the dispersion equation appearing in [14, 16, 27]. The assumptions needed to arrive at this dispersion equation are shown in Section 2.4. To summarise, the k_p are determined by solving:

$$\det \boldsymbol{M}(k_\star) = 0, \quad \text{with} \quad M_{nn'}(k_\star) = \delta_{nn'} + 2\pi\mathfrak{n}T_n[\mathcal{N}_{n'-n} - \mathcal{G}_{n'-n}], \tag{2.13}$$

where

$$\mathcal{N}_\ell = \frac{1}{k_\star^2 - k^2}(ka_{12}\mathrm{H}'_\ell(ka_{12})\mathrm{J}_\ell(k_\star a_{12}) - k_\star a_{12}\mathrm{H}_\ell(ka_{12})\mathrm{J}'_\ell(k_\star a_{12})), \tag{2.14}$$

$$\mathcal{G}_\ell = \int_{a_{12}}^{b_{12}} \mathrm{J}_\ell(k_\star r)\mathrm{H}_\ell(kr)(\mathrm{g}(r) - 1)r\mathrm{d}r, \tag{2.15}$$

and the term $\mathfrak{n}$ is the average number of particles per area, $r = |\boldsymbol{r}|$, $\delta_{nn'}$ is the Kronecker delta, and H_ℓ is the Hankel function of the first kind, while J_ℓ is the Bessel function. The term $\mathcal{N}_\ell$ acts as a coupling term relating to the scattered field at one particle

expressed in coordinates centred at another particle. The term T_n is the T-matrix which determines how one particle scatters waves by itself. For circular homogeneous particles in acoustics we have that:

$$T_n = -\frac{\gamma \mathrm{J}_n'(ka)\mathrm{J}_n(k_o a) - \mathrm{J}_n(ka)\mathrm{J}_n'(k_o a)}{\gamma \mathrm{H}_n'(ka_o)\mathrm{J}_n(k_o a) - \mathrm{H}_n(ka)\mathrm{J}_n'(k_o a)}, \tag{2.16}$$

where $\gamma = \frac{\rho_o c_o}{\rho c}$ and $k_o = \frac{\omega}{c_o}$, with ρ_o being the mass density of the particles and c_o being the wavespeed within the particles.

There are infinitely many $k_\star$ which solve $\det \boldsymbol{M}(k_\star) = 0$. We denote these solutions as k_1, $k_2, \ldots$. The main objective of our Monte-Carlo simulations is to check if the theoretical predictions of the wavenumbers k_p are accurate, and to clearly demonstrate that there is more than one effective wavenumber appearing in the Monte-Carlo results. Before doing this, let us first explore the effective wavenumbers predicted by solving the dispersion equation (2.13).

Effective wavenumbers. We want to identify when the dispersion equation (2.13) predicts that there is more than one effective wavenumber that has a significant contribution to the average transmitted wave. It is important to understand when this occurs, as it is far simpler to calculate the average field when there is only one effective wavenumber [15, 16].

Most of the scientific community at present is also not aware that more than one effective wavenumber can be excited [7, 31, 33], for just one scalar wave. So we will identify for which parameters we can run a heavy Monte-Carlo simulation, as detailed in Section 2.3, to find clear numerical evidence of multiple effective wavenumbers.

	Density	Wavespeed
Background material	$\rho_o = 1.0$ kg/m^3	$c_o = 1.0$ m/s
Sound-soft particles	$\rho_o = 0.30$ kg/m^3	$c_o = 0.30$ m/s
Sound-hard particles	$\rho_o = 10.0$ kg/m^3	$c_o = 10.0$ m/s

Table 2.1: Shows the properties of the background medium and the two main particle properties used for the numerical results. Note that sound-soft (sound-hard) particles are strong (weak) scatterers.

According to theoretical results, only one effective wavenumber k_1 is needed when Im $k_1 \ll$ Im k_p for $p = 2, 3, \ldots$. In any other case, more than one effective wavenumber can be excited and contribute to the average transmission [14, 16]. Though we note that the form of the incident wave and the geometry of the material also affects how the wavenumbers are excited [15].

The first step is to sweep the parameter space by varying the frequency ω and

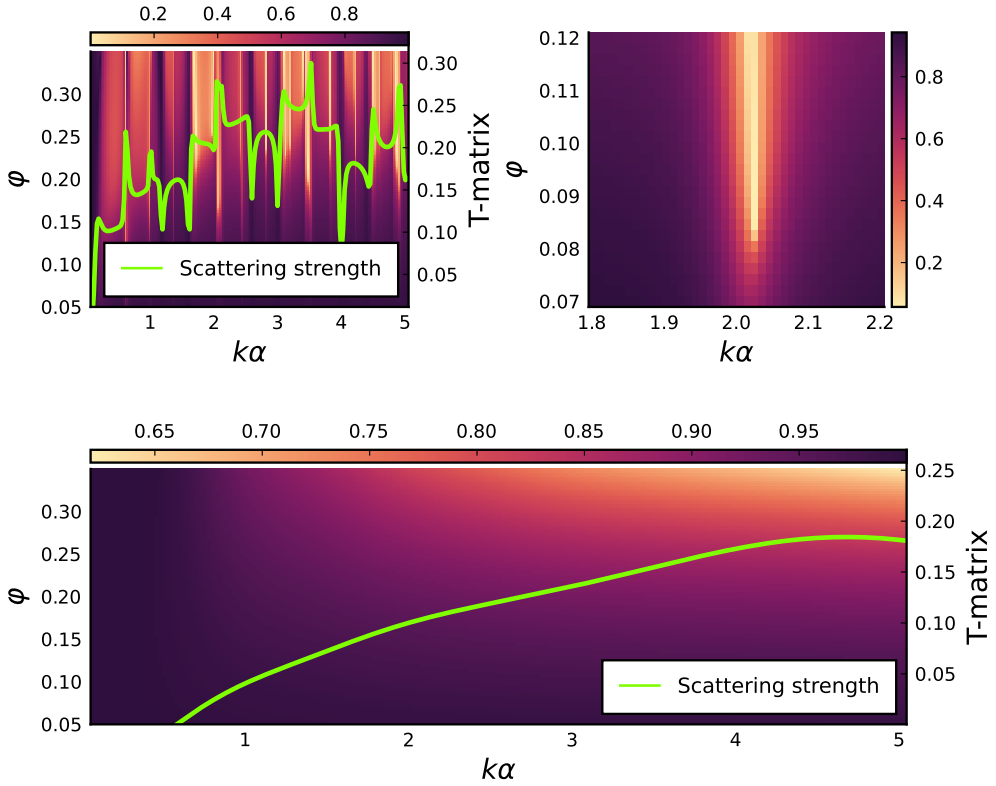

Figure 2.4: The phase diagrams showing when more than one effective wavenumber is needed. The top two diagrams are for sound-soft particles and the bottom diagram is for sound-hard particles with properties shown in Table 2.1. The colour is given by (2.17) where the lighter colours (those above 0.5 shown in the colour bar) indicate that more than one effective wavenumber can be excited. The green curve shows the scattering strength of just one particle and is given by (2.18).

particle volume fraction ϕ, and for each value calculate the effective wavenumbers k_p by solving (2.13). We do this for both sound-hard and sound-soft particles by changing ρ_o and c_o in (2.16). The two main particle properties used are shown in Table 2.1. Next, based on the results shown in [14, 16], we can estimate where more than one effective wavenumber is excited by plotting a heatmap where the colour is given by:

$$\text{colour} = \left| \frac{\operatorname{Im} k_2}{\operatorname{Im} k_1} - 1 \right|. \tag{2.17}$$

After many failed attempts to establish a connection between the phenomena observed in Figure 2.4 and known physical models, we find that the measure (2.17) is

closely related to the scattering strength of a single particle, given by:

$$\text{Scattering strength} = \sqrt{\sum_n |T_n|^2}, \tag{2.18}$$

where T_n is the T-matrix given by (2.16) for acoustics.

The results of sweeping over frequency and particle volume fraction are shown in Figure 2.4. We call these figures phase diagrams, as we see sudden shifts from only one effective wavenumber to two or more wavenumbers. The regions with lighter shading correspond to cases where the value of (2.17) is low, so more than one effective wavenumber is excited. Conversely, the regions with dark shading are where only one effective wavenumber is excited. The green curves shown on top of the phase diagrams are the scattering strength for just one particle. Clearly we see that a large scattering strength leads to more than one effective wavenumber, which is an important observation, as calculating (2.18) is far simpler than calculating the wavenumbers k_p.

The phase diagrams in Figure 2.4 show a large region of the parameter space, but to see in more detail when two or more effective wavenumbers are needed it helps to plot the imaginary parts of the wavenumbers k_p against frequency, which we do in Figure 2.5 for a particle volume fraction of 25%. For sound-soft particles (Figure 2.5a), there are many frequencies ka where two or even three effective wavenumbers have a similar imaginary part, meaning that these wavenumbers can be excited. In contrast, for sound-hard particles (Figure 2.5b), there is only one effective wavenumber that can be easily excited, as there is one curve, representing k_1, that has a significantly lower imaginary part than all the others. The only way to clearly separate the effective wavenumbers would be to use continuity and smoothness to try and follow one curve as ka increases. Due to many jumps and curves crossing each other, it was not possible to identify them separately. Some people might argue that this bears a resemblance to a form of image segmentation. Nonetheless, such a detailed separation is not necessary for our argument, which emphasises that there are lots of different effective wavenumbers close by. Seeing as it is not needed, and the fact that it is not essential for our purposes, we decided not to pursue this approach. In Section 2.3, we use the results presented in Figure 2.5 to identify specific scenarios suitable for Monte-Carlo simulations. This will allow us to verify whether the predictions of more than one effective wavenumber are indeed accurate.

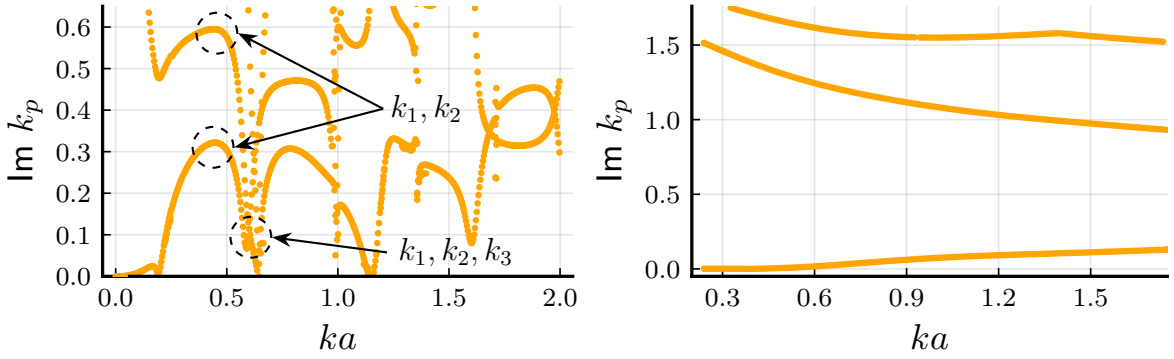

(a) sound-soft particles

(b) sound-hard particles

Figure 2.5: Depicts the imaginary part of the wavenumbers k_p with respect to the non-dimensional frequency ka. We only show the three wavenumbers with the smallest imaginary parts as these are the only ones which make a significant contribution to the average wave. The lowest curve represents k_1, which is the easiest to excite. The particles occupy 25% of the material in each case and their properties for sound-soft and sound-hard particles are shown in Table 2.1.

2.3 The Monte-Carlo simulation

A simple way to approximate the average field (2.9) is to perform a simulation for each particle configuration and then take an average over all configurations. As we are focusing on uniformly distributed particles, the probability density $\mathrm{p}(\Lambda)$ is a constant if particles do not overlap, and $\mathrm{p}(\Lambda) = 0$ if any two particles do overlap. This allows us to numerically approximate the ensemble average:

$$\langle u(\boldsymbol{r};\Lambda)\rangle = \frac{1}{S}\sum_{s=1}^{S} u(\boldsymbol{r};\Lambda_s), \tag{2.19}$$

where each Λ_s is one randomly sampled configuration of particles within the plate that depends on the parameter s. That is, we first create a configuration of particles Λ_s, then simulate the scattered waves $u(\boldsymbol{r};\Lambda_s)$, and then we repeat this process for S configurations of particles, until the average in (2.19) converges. As mentioned in previous sections, $\langle u(\boldsymbol{r};\Lambda)\rangle$ should converge to a sum of plane-waves as shown by (2.12).

The setup for our Monte-Carlo simulations is shown in Figure 2.2 (note the x-axis is the vertical axis in the figure), and we used an incident wave of the form $u_{\text{inc}}(x) = \mathrm{e}^{\mathrm{i}kx}$. To calculate the field $u(\boldsymbol{r};\Lambda_s)$ for each configuration we use a multipole expansion for each particle, together with translation matrices, to solve the boundary conditions [31]. Specifically, we solve [16, Equation (2.9)] for each s, calculate (2.19) and evaluate the

field at $\langle u(x, 0; \Lambda_s)\rangle$ with the x values satisfying the condition at (2.12). This method accurately approximates the exact solution when increasing the truncation order of the multipole expansion until reaching convergence.

An initial numerical investigation revealed that it was computationally feasible to simulate a finite number of particles within the region $0 \leq x \leq 20$, so the width of plate $W = 20$ and height $H = 400$. For details on the methodology of our Monte-Carlo simulations, see Appendix A.

2.3.1 The Monte-Carlo results

Based on the results presented in Section 2.2.1, we choose several cases to simulate the average field with a Monte-Carlo method. We want to identify cases where two or even three wavenumbers can be excited for frequencies as low as possible, because increasing the frequencies lead to a significantly larger computational cost for the Monte-Carlo simulations. This is why we only performed Monte-Carlo simulations for two different frequencies, beyond the low-frequency limit. See Appendix A for details, and descriptions on computational cost.

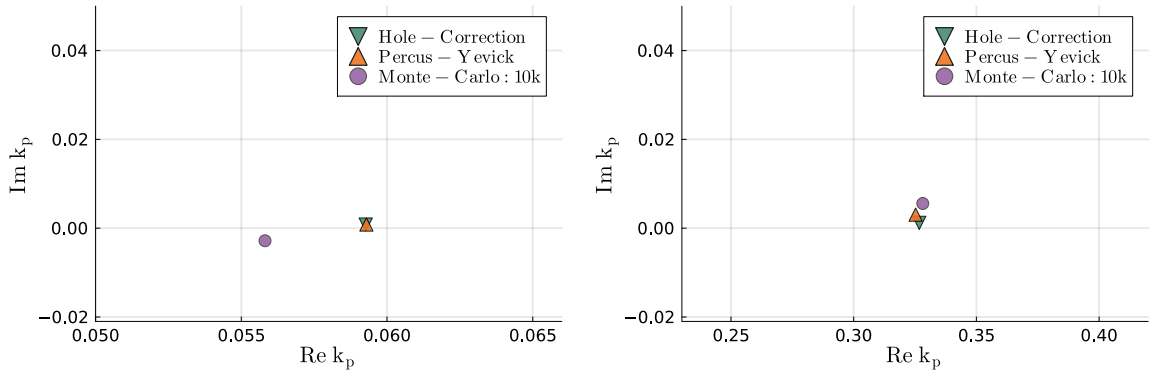

(a) $\phi = 5\%,\ ka = 0.04$ (b) $\phi = 25\%,\ ka = 0.36$

Figure 2.6: The figure on the left shows the behaviour of sound-soft particles in the low-frequency and low volume fraction regime, whereas the figure on the right demonstrates the properties of sound-hard particles. The specific characteristics of these particles are detailed in Table 2.1. The radius of each particle is $a = 1.2$. Both figures depict scenarios where the dispersion equation (2.13) predicts only one effective wavenumber k_p with a lower imaginary part, and therefore this is the only wavenumber that can be excited. The green and red triangles represent effective wavenumbers predicted by the (2.13) when using either the Hole-Correction or Percus-Yevick pair-correlation. The purple dotted points represent the effective wavenumber which best fits the Monte-Carlo simulations when using the formula (2.12).

One effective wavenumber. From Figure 2.5b we see that for sound-hard particles there is a broad range of frequencies where there is only one effective wavenumber with an imaginary part which is far smaller than all others. This means that it is easy to excite this wavenumber, but very difficult to excite the others. This message is also confirmed by the phase diagram shown in Figure 2.4. To verify there is only one effective wavenumber, we perform Monte-Carlo simulations for $ka = 0.36$ for sound-hard particles, and fit the formula (2.12). The results shown in Figure 2.6b confirm that there is only one wavenumber present in the Monte-Carlo simulations. There is a small discrepancy between the effective wavenumbers from the dispersion equation (2.13) and the fitted effective wavenumbers, which could be due to errors introduced in the Monte-Carlo simulations due to truncating an infinite region.

On the other hand, for sound-soft particles we see from Figure 2.5a that only for lower frequencies $0 \leq ka \leq 0.2$, only one effective wavenumber with a smaller imaginary part exists. Monte-Carlo simulations, shown in Figure 2.6a, confirm that there is only one effective wavenumber as predicted by the theory.

Fitting for several effective wavenumbers. Increasing the frequency for sound-soft particles leads to many frequencies where two, or more, effective wavenumbers have a lower imaginary part. For example, for $0.25 < ka < 0.63$ there are two wavenumbers with a smaller imaginary part, which means it is possible to excite two effective wavenumbers in this frequency range. To exemplify, we choose two different frequencies to perform Monte-Carlo simulations:

- $ka = 0.36$, where we aim to excite two effective wavenumbers.
- $ka = 0.62$ where we aim to excite three effective wavenumbers.

Given that we run the Monte-Carlo simulations 40,000 times, we get high fidelity datasets which leads to very small standard error of the mean of the Monte-Carlo simulations. Should the standard error of the mean have been larger, the shaded region in Figures 2.7, 2.9a and 2.9c would have been more visible, introducing some uncertainty in the data. See Appendix A for details on computational cost.

The results of these simulations are presented in Figure 2.7, comparing the average field from the simulation with three types of wave interpretations: the *Dominant Wave* and the *Fitted Wave* alongside its extension, the *Extended Wave*. The dominant wave is derived by fitting the formula (2.12) with $P = 1$, based on the traditional approach where only a single effective wavenumber is considered. This approach, though widely used, proves inadequate as it fails to account for the presence of multiple effective wavenumbers. We demonstrate this in Figures (2.7a) and (2.7c) for $ka = 0.36$ and $ka = 0.62$ respectively. In contrast, the fitted wave shows the outcome of applying

(2.12) with the parameter P set to match the number of effective wavenumbers we aim to excite based on the frequency. To further explain, for $ka = 0.36$, $P = 2$ is used to fit the formula to the Monte-Carlo data, while for $ka = 0.62$, $P = 3$ is used to excite the three wavenumbers. Now, extending the fitted wave beyond the region where (2.12) was fitted to the Monte-Carlo data, describes the extended wave. While the extended wave can still closely follow the Monte-Carlo results, the match with the Monte-Carlo field is expected to get worse as the extended field gets closer to $x = 0$. This is due to a boundary layer where many effective wavenumbers become significant [14, 16].

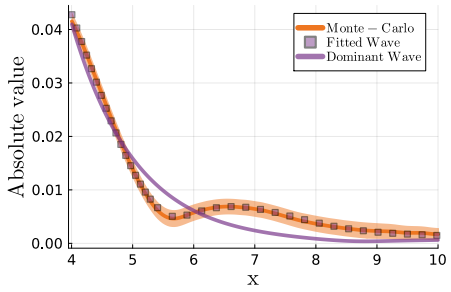

(a) sound-soft: $\phi = 25\%,\ ka = 0.36$

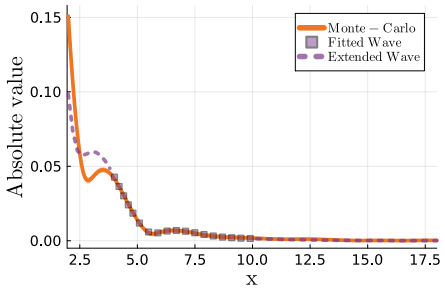

(b) sound-soft: $\phi = 25\%,\ ka = 0.36$

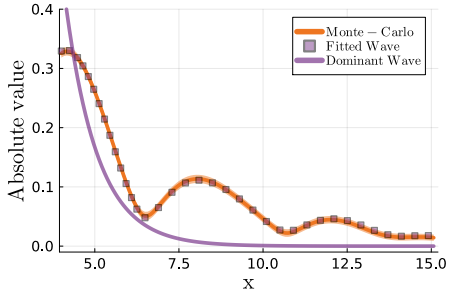

(c) sound-soft: $\phi = 25\%,\ ka = 0.62$

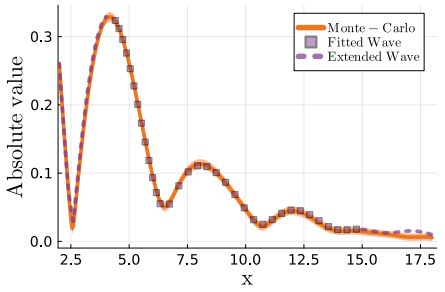

(d) sound-soft: $\phi = 25\%,\ ka = 0.62$

Figure 2.7: The graphs compare the average field from a Monte-Carlo simulation for sound-soft particles in a plate, as shown in Figure 2.2, with two types of fitted waves. The *Dominant Wave* is the result of fitting for just one effective wavenumber when using the formula (2.12) with $P = 1$, and is currently believed to be accurate by most working in the field. We see here that it is not possible to fit for just one wavenumber. The *Fitted Wave* is a result of fitting the formula (2.12) with $P = 2$ for the top two graphs and $P = 3$ for the bottom two, whereas the *Extended Wave* shows what the formula (2.12) predicts outside of the fitted region. The shaded region represents the standard error of the mean of the Monte-Carlo simulations. The non-dimensional frequency ka and volume fraction ϕ used are shown below each figure, the particle radius is $a = 1.2$ and the properties for the background medium and the sound-soft particles can be found in Table 2.1. The key parameters for simulating the scattering of waves in a plate filled with particles are discussed in Appendix A.

Figures (2.7b) and (2.7d) show how the formula (2.12) fitted to the Monte-Carlo data clearly matches the Monte-Carlo data and how the same formula predicts the field

outside of the fitted region. The presence of the boundary layer, and our theoretical results in Section 2.4, have all guided how best to perform, and fit to, the Monte-Carlo results as discussed in Appendix A.

Avoid overfitting. Having an accurate fit does not necessarily give strong evidence that the formula (2.12) is correct. This is especially true for higher frequencies where the Monte-Carlo simulation has a higher standard error of the mean, shown by the shaded yellow region. A larger standard error means that there is a range of effective wavenumbers which can fit this data, and still be closer to the Monte-Carlo results than the standard error. Further, fitting a sum of plane-waves, such as shown by (2.12), can lead to overfitting when using too many wavenumbers, and even become ill-posed. We explain more details on this in the Monte-Carlo methodology in Appendix A.

Projection Method. To ensure that our model is robust against overfitting, and to check if small changes in the field lead to large changes in the fitted wavenumbers, we develop a method, called the *Projection Method*. This method is designed to fit the formula (2.12) for all possible combinations of the effective wavenumbers in a specified region. Given the instability of nonlinear optimisation for scenarios involving multiple effective wavenumbers [35], the Projection Method serves a dual purpose. It not only fits the formula (2.60) but also estimates the sensitivity of the parameters k_p to the dataset.

To fit Monte-Carlo data for the cases with more than one effective wavenumbers, we design an algorithm that sweeps over all possible values of the wavenumbers k_p and for each case performs a linear fit, by using least-squares, to predict the amplitudes A_p^+ in (2.60). For that, we consider a mesh in the complex plane $\mathcal{C} \subset \mathbb{C}$ from which we sample values of k_p.

A sketch of the algorithm for the case $P = 3$ is given in Algorithm 1.

The algorithm calculates the minimum error $\varepsilon(k_1)$ for every possible k_1, and it is this error which is shown in Figures 2.8, 2.9b and 2.9d. We perform further analysis to establish if the optimal wavenumbers are located at the local minima shown, and whether the fitted curves when using (2.60) are within the standard error of the mean of the Monte-Carlo simulation. The blue region in Figure 2.8 is derived by using the smoothing algorithm presented in Appendix A and contains all wavenumbers for which the fitted curves are within the standard error of the mean. There are clearly two distinct disconnected regions for possible values of k_p, which shows that the transmitted wave is composed of a sum of two effective waves.

At least two effective wavenumbers. The result of fitting two effective wavenumbers for $ka = 0.36$ is shown in Figure 2.8. The main conclusion is that this is the first

Algorithm 1: Algorithm for the Projection Method

Data: $\langle u(x,0;\Lambda)\rangle$
for *all values of* $k_1 \in \mathcal{C}$ **do**
  for *all values of* $k_2, k_3 \in \mathcal{C}$ **do**
    if $k_1 \neq k_2 \neq k_3$ **then**
      Determine the values of A_p^+ that best fit $\langle u(x,0;\Lambda)\rangle$ using least-squares;
      Using (2.60), compute the error $\varepsilon(k_1,k_2,k_3) = \|h(x) - \langle u(x,0;\Lambda)\rangle\|$;
      Store $\varepsilon(k_1,k_2,k_3)$;
    end
  end
  Store $\varepsilon(k_1) = \min_{k_2,k_3} \varepsilon(k_1,k_2,k_3)$
end
Result: $\varepsilon(k_1)$

clear evidence that there are two complex effective wavenumbers by using Monte-Carlo simulations which are highly accurate. In more detail: the figure shows that there are two separate effective wavenumbers: one within the blue dashed curve on the left and the other, necessarily, within the blue dashed curve on the right. Wavenumbers within these dashed regions lead to fitting errors which are less than the error committed by the Monte-Carlo simulation.

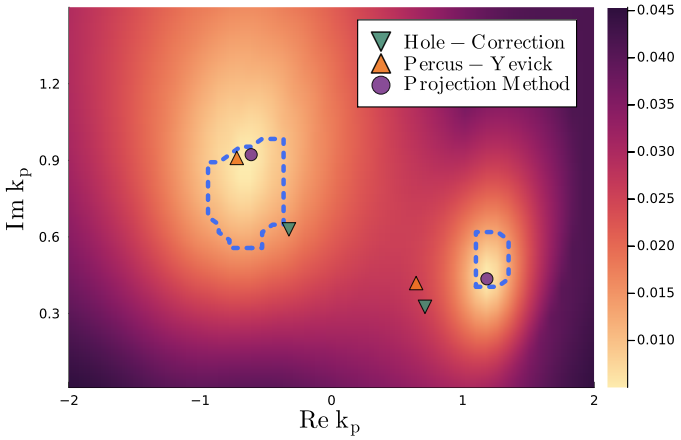

Figure 2.8: Shows how two wavenumbers are needed to fit the formula (2.12) to the Monte-Carlo results. The properties for the background medium and the sound-soft particles can be located in Table 2.1. The particles occupy 25% of the material and the simulation runs for the non-dimensional frequency $ka = 0.36$ where the particle radius is $a = 1.2$. When using the two best fits, shown by the Projection Method, we obtain the fitting shown in Figure 2.7b. The density plot shows what regions of complex wavenumbers that best fit the Monte-Carlo results. When using one wavenumber k_1 in the dashed blue curve on the left, there exists another wavenumber k_2 within the dashed blue region on the right that together to a fitting error which is smaller than the standard error of the mean of the Monte-Carlo simulation.

We also see the dispersion equation (2.13), together with the Percus-Yevick pair-correlation, predicts at least one wavenumber within the blue dashed curve. The predicted wavenumbers when using the Hole-Correction pair-correlation are also shown. The dispersion equation (2.13) predicts an infinite number of effective wavenumbers, so we present only the two wavenumbers with the smallest imaginary part.

Three effective wavenumbers. Figure 2.9 shows in steps our attempt to identify three effective wavenumbers for $ka = 0.62$. The summary is that the amplitude A_3 for the third wavenumber in (2.12) is too small, $|A_3| \approx 0.004$, and as a result, we can not reliably say whether the Monte-Carlo simulations show that there are indeed three effective wavenumbers. This is because the expected errors from the Monte-Carlo simulation are on the order of around 0.003. However, we do conclude again that one effective wavenumber is not enough, at least two are needed.

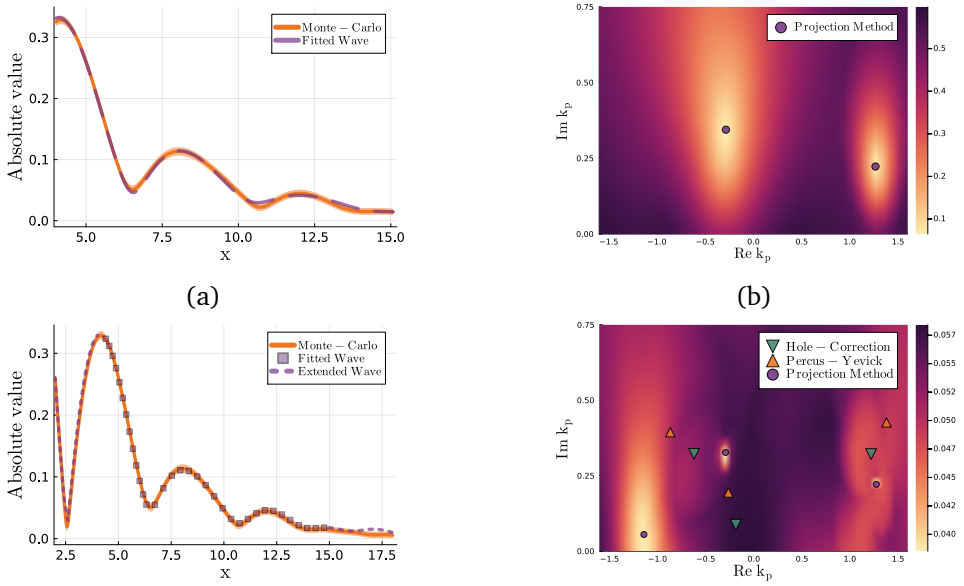

Figure 2.9: The top two graphs show the result of using two effective wavenumbers in the formula (2.12) to fit to the Monte-Carlo results for sound-soft particles (properties given in Table 2.1), volume fraction $\phi = 25\%$ and non-dimensional frequency $ka = 0.62$ where $a = 1.2$. Figure 2.9b shows a density plot over the effective wavenumbers, with light regions indicating that those wavenumbers better fit the data. However, all possible choices of two wavenumbers lead to fitting errors which are greater than the standard error of the mean of the Monte-Carlo simulations. The two wavenumbers with the best fit are denoted by the Projection Method, and lead to the field shown in Figure 2.9a. The bottom two graphs use three effective wavenumbers in the formula (2.12) to fit to the Monte-Carlo results. In this case, we find 4 sets of wavenumbers, all close to each other, that have a fitting error less than the standard error of the mean. The result of using the three wavenumbers with the best fit is shown in Figure 2.9c. However, in Figure 2.9d there are many choices for the wavenumbers which lead to small fitting errors. In particular, the Projection method wavenumber with the smaller imaginary part is sensitive to small changes in the Monte-Carlo results.

In more detail, the top two graphs of Figure 2.9 show the result of fitting the formula (2.12) with $P = 2$ to the Monte-Carlo results. Although there are clearly choices of two wavenumbers which fit the data well, there are no possible choices which lead to fitting errors that are less than the standard error of the mean, as shown by Figure 2.9a which uses the two wavenumbers with the best fit. The bottom two graphs Figure 2.9 show how the fitting errors decrease when adding a third wavenumber, i.e. using $P = 3$ in the formula (2.12). By using $P = 3$, instead of $P = 2$, the fitting error decreased from 6% to 3.8%. Although the fitting error does decrease to below the standard error of the mean, it is only a small decrease, and close to the errors inherent in the Monte-Carlo data. We note that the two Projection Method wavenumbers shown in Figure 2.9b are equal to two of the Projection Method wavenumbers shown in Figure 2.8.

2.4 Deducing the average transmitted wave

In [14, 15, 16] the authors demonstrated that there exist several effective wavenumbers, however, it was not clear how these appear in the average transmitted field. Taking inspiration from [30], the average transmitted field should be a sum of waves, each with a different effective wavenumber. In this section we demonstrate this for any incident field and material geometry.

We use the same notation given in [15] and combine the methods shown in [15] and [30] to show that the average transmitted field is a sum of the incident field plus several effective fields.

We note that although the paper [15] is written for three-dimensional particles, the results that lead up to [15, Section 5] are valid for any dimension as long as we appropriately define the spherical waves u_n and v_n and the translation matrices $\mathcal{V}_{nn'}$ and $\mathcal{U}_{nn'}$. In the case of two dimensions and scalar waves these terms are:

$$\mathrm{v}_n(k\boldsymbol{r}) = \mathrm{J}_n(kr)\mathrm{e}^{\mathrm{i}m\theta}, \quad \mathrm{u}_n(k\boldsymbol{r}) = \mathrm{H}_n(kr)\mathrm{e}^{\mathrm{i}m\theta}, \tag{2.20}$$

$$\mathcal{V}_{nn'}(\boldsymbol{r}) = \mathrm{v}_{n-n'}(\boldsymbol{r}), \quad \text{and} \quad \mathcal{U}_{nn'}(\boldsymbol{r}) = \mathrm{u}_{n-n'}(\boldsymbol{r}), \tag{2.21}$$

where J_n and H_n are the Bessel function and Hankel function of the first kind, and (r, θ) are the polar coordinates of $\boldsymbol{r}$. In our calculations, we will use the general notation rather than substitute the specific form for the two dimensions as shown in (2.21). This way, the proofs we present are valid for any dimension.

For just one configuration of particles, the way we represent the total field $u(\boldsymbol{r})$

depends on whether $\boldsymbol{r}$ is inside a particle or not. We choose to write the field in the form [22, 23, 30]:

$$u(\boldsymbol{r}) = \begin{cases} u_{\text{inc}}(\boldsymbol{r}) + u_{\text{sc}}(\boldsymbol{r}), & \text{for } \boldsymbol{r} \in \mathcal{R} \setminus \mathcal{P}, \\ u_{\text{in}}^{j}(\boldsymbol{r}), & \text{for } \boldsymbol{r} \in \mathcal{P}_j, \end{cases} \tag{2.22}$$

where $u_{\text{inc}}(\boldsymbol{r})$ is the incident wave, $u_{\text{sc}}(\boldsymbol{r})$ is a sum of all the scattered waves, and $u_{\text{in}}^{j}(\boldsymbol{r})$ is the field inside particle j. We use $\mathcal{P}_j$ to denote the region occupied by particle j, whereas $\mathcal{P} = \cup_j \mathcal{P}_j$ is the union of all particles. See Figure 2.10 for an illustration.

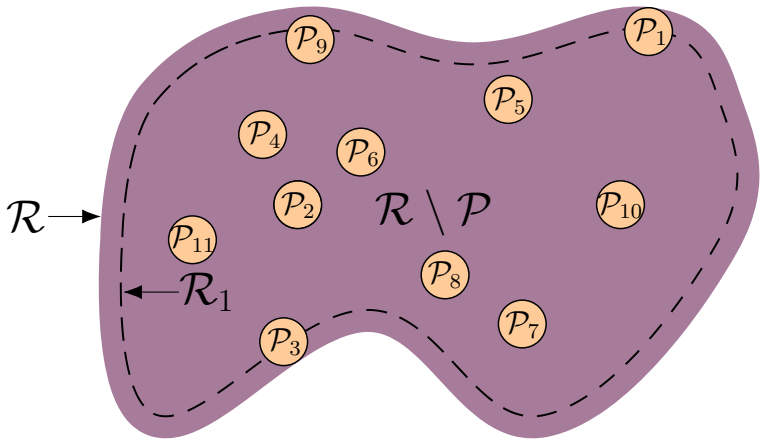

Figure 2.10: A two-dimensional region $\mathcal{R}$ filled with equal-sized disks $\mathcal{P}_j$, which represent the particles. The region $\mathcal{P} = \cup_j \mathcal{P}_j$ depicts the region inside the particles while the shaded region ($\mathcal{R} \setminus \mathcal{P}$) depicts the region outside the particles. The region $\mathcal{R}$ completely contains all the particles, while the region $\mathcal{R}_1$ contains only the particle centres. As the particles are at least one radius a away from the boundary of $\mathcal{R}$, we have that $\mathcal{R}_1$ is smaller than $\mathcal{R}$. Note that as the particles do not overlap, we have that $\mathcal{R} \setminus \mathcal{P} = \mathcal{R} \setminus \mathcal{P}_\ell - \sum_{j \neq \ell} \mathcal{P}_j$ for every ℓ.

The sum of the scattered waves $u_{\text{sc}}(\boldsymbol{r})$, shown in (2.22), is given by:

$$u_{\text{sc}}(\boldsymbol{r}) = \sum_{j=1}^{J} u_{\text{sc}}^{j}(\boldsymbol{r}), \quad \text{where} \quad u_{\text{sc}}^{j}(\boldsymbol{r}) = \sum_{n} f_n^j \mathrm{u}_n(k\boldsymbol{r} - k\boldsymbol{r}_j). \tag{2.23}$$

The field inside the j-th particle can be written in terms of a regular radial waves expansion:

$$u_{\text{in}}^{j}(\boldsymbol{r}) = \sum_{n} b_n f_n^j \mathrm{v}_n(k_o\boldsymbol{r} - k_o\boldsymbol{r}_j), \tag{2.24}$$

where

$$b_n = \frac{T_n \mathrm{H}_n(ka) + \mathrm{J}_n(ka)}{T_n \mathrm{J}_n(k_o a)}, \tag{2.25}$$

and, as a reminder, $k_o = \frac{\omega}{c_o}$ and T_n is given by (2.16). The coefficients in (2.25) describe how the internal structure of the particles affects the wave. For a light introduction on the T-matrix and multiple scattering see [12] and [13].

The ensemble average of any field f, and the conditional ensemble average, are defined as follows:

$$\langle \mathrm{f} \rangle = \int_{\mathcal{R}_1^J} \mathrm{f}\, \mathrm{p}(\boldsymbol{r}_1, \ldots, \boldsymbol{r}_J) \mathrm{d}\boldsymbol{r}_1 \cdots \mathrm{d}\boldsymbol{r}_J, \tag{2.26}$$

$$\langle \mathrm{f} \rangle(\boldsymbol{r}_1) = \int_{\mathcal{R}_1^{J-1}} \mathrm{f}\, \mathrm{p}(\boldsymbol{r}_2, \ldots, \boldsymbol{r}_J | \boldsymbol{r}_1) \mathrm{d}\boldsymbol{r}_2 \cdots \mathrm{d}\boldsymbol{r}_J. \tag{2.27}$$

Here $\mathcal{R}_1^J$ denotes that the integration domain of all J integrals is $\mathcal{R}_1$, which corresponds to the region containing only the particle centres. The probability density function $\mathrm{p}(\boldsymbol{r}_1, \boldsymbol{r}_2, \ldots, \boldsymbol{r}_J)$ represents the likelihood of having particles centred at $\boldsymbol{r}_1, \boldsymbol{r}_2, \cdots, \boldsymbol{r}_J$, while $\mathrm{p}(\boldsymbol{r}_2, \ldots, \boldsymbol{r}_J | \boldsymbol{r}_1)$ is the conditional probability density and can be defined as:

$$\mathrm{p}(\boldsymbol{r}_2, \ldots, \boldsymbol{r}_J | \boldsymbol{r}_1) := \frac{\mathrm{p}(\boldsymbol{r}_1, \ldots, \boldsymbol{r}_J)}{\mathrm{p}(\boldsymbol{r}_1)}. \tag{2.28}$$

To calculate the ensemble average of the transmitted field, it is helpful to write the field in the following form:

$$u(\boldsymbol{r}) = [u_{\mathrm{inc}}(\boldsymbol{r}) + u_{\mathrm{sc}}(\boldsymbol{r})] \chi_{\mathcal{R}\setminus\mathcal{P}}(\boldsymbol{r}) + \sum_j u_{\mathrm{in}}^j(\boldsymbol{r}) \chi_{\mathcal{P}_j}(\boldsymbol{r}), \tag{2.29}$$

where $\chi_{\mathcal{A}}(\boldsymbol{r})$ is defined as the characteristic function:

$$\chi_{\mathcal{A}}(\boldsymbol{r}) = \begin{cases} 1, & \text{if } \boldsymbol{r} \in \mathcal{A}, \\ 0, & \text{if } \boldsymbol{r} \notin \mathcal{A}. \end{cases} \tag{2.30}$$

By taking the ensemble average of (2.29) we obtain:

$$\langle u(\boldsymbol{r}) \rangle = \langle u_{\mathrm{inc}}(\boldsymbol{r}) \chi_{\mathcal{R}\setminus\mathcal{P}}(\boldsymbol{r}) \rangle + \langle u_{\mathrm{sc}}(\boldsymbol{r}) \chi_{\mathcal{R}\setminus\mathcal{P}}(\boldsymbol{r}) \rangle + J \langle u_{\mathrm{in}}^1(\boldsymbol{r}) \chi_{\mathcal{P}_1}(\boldsymbol{r}) \rangle, \tag{2.31}$$

where each term of the sum in (2.29) is the same after ensemble averaging because they are all integrated over the same domain, which means that all particles are indistinguishable from each other. To calculate (2.31) we need to make a few assumptions.

Isotropy and homogeneity assumption. We assume isotropy and homogeneity, which means that $\mathrm{p}(\boldsymbol{r}_1)$, the probability density of one particle being at $\boldsymbol{r}_1$, is a constant.

Then, because the integral of $\mathrm{p}(\boldsymbol{r}_1)$ over $\mathcal{R}_1$ has to equal 1, we conclude that:

$$\mathrm{p}(\boldsymbol{r}_1) = \frac{1}{|\mathcal{R}_1|} = \frac{\mathfrak{n}}{J}, \tag{2.32}$$

where $|\mathcal{R}_1|$ is the volume of $\mathcal{R}_1$, J is the total number of particles and $\mathfrak{n}$ is the number density of particles defined by:

$$\mathfrak{n} := \frac{J}{|\mathcal{R}_1|} = \frac{\phi}{|\mathcal{P}_1|}, \tag{2.33}$$

with ϕ being the particle volume fraction, and $|\mathcal{P}_1|$ being the volume of a particle. Isotropy and homogeneity also imply that the pair-correlation g had the form (2.11) [42]. For convenience, we now use the form:

$$\mathrm{p}(\boldsymbol{r}_2|\boldsymbol{r}_1) = \frac{\mathfrak{n}}{J-1}\mathrm{g}(|\boldsymbol{r}_1 - \boldsymbol{r}_2|). \tag{2.34}$$

The term $(J-1)$ appears now, rather than J, due to there being a finite number of particles, and it ensures that $\mathrm{g}(|\boldsymbol{r}_1 - \boldsymbol{r}_2|) \to 1$ when particles become uncorrelated, as confirmed by [45, Equation (8.1.2)]. For more details on the pair-correlation see [45, Chapter 8 and 9].

Correlation distance assumption. We can only resolve the integrals appearing in (2.31) when $\boldsymbol{r}$ satisfies:

$$\min_{\boldsymbol{r}_1 \in \partial\mathcal{R}_1} |\boldsymbol{r} - \boldsymbol{r}_1| \geq b_{12} + a, \tag{2.35}$$

that is, when the distance of $\boldsymbol{r}$ to the boundary $\partial\mathcal{R}_1$ is greater than $b_{12} + a$. As defined in (2.11), the distance b_{12} denotes the correlation length. Our analysis shows that when (2.35) is true, the transmitted field (2.31) is a sum of effective waves, and the incident wave is no more.

Quasi-crystalline assumption. To calculate (2.31) we assume the closure assumption known as the Quasi-Crystalline Approximation (QCA) which neglects repeated back and forth scattering between a fixed pair of particles. Details are given in [15, 18, 29].

The calculations needed to simplify the ensemble averages in (2.31) are shown in

Appendix B.1-B.3. To summarise, with all given assumptions, (2.31) leads to:

$$\langle u(\boldsymbol{r})\rangle = (1-\phi)u_{\text{inc}}(\boldsymbol{r}) + J\langle u^1_{\text{sc}}(\boldsymbol{r})\chi_{\mathcal{R}\setminus\mathcal{P}_1}(\boldsymbol{r})\rangle - J(J-1)\langle u^1_{\text{sc}}(\boldsymbol{r})\chi_{\mathcal{P}_2}(\boldsymbol{r})\rangle + J\langle u^1_{\text{in}}(\boldsymbol{r})\chi_{\mathcal{P}_1}(\boldsymbol{r})\rangle, \quad (2.36)$$

where the terms in (2.36) are given by (2.62), (2.70), and (2.75). In Section 2.4.1 we show that (2.36) is a sum of waves.

2.4.1 Transmitted effective waves

In this section, we use the effective wave assumption to demonstrate that (2.36) is composed of functions which satisfy effective wave equations. We show that:

$$\langle u(\boldsymbol{r})\rangle = w_{\text{inc}}(\boldsymbol{r}) + \sum_{p=1}^{\infty} w_p(\boldsymbol{r}), \quad (2.37)$$

where

$$\nabla^2 w_{\text{inc}}(\boldsymbol{r}) + k^2 w_{\text{inc}}(\boldsymbol{r}) = 0 \quad \text{and} \quad \nabla^2 w_p(\boldsymbol{r}) + k_p^2 w_p(\boldsymbol{r}) = 0. \quad (2.38)$$

We also show that $w_{\text{inc}}(\boldsymbol{r}) = 0$ when (2.35) holds, and when using the effective boundary condition which is deduced from first principles in [15]. That is, the incident wave is not present inside the material[‡].

For what follows, to keep the notation concise, we define the ball region using standard set-builder notation:

$$\mathcal{B}(\boldsymbol{x}; R) = \left\{\boldsymbol{y} \in \mathbb{R}^2 : \ |\boldsymbol{x}-\boldsymbol{y}| \leq R\right\}. \quad (2.39)$$

The first term in (2.36) is given by $(1-\phi)u_{\text{inc}}(\boldsymbol{r})$, which clearly contributes to the term $w_{\text{inc}}(\boldsymbol{r})$ in (2.37), because the incident wave satisfies the Helmholtz equation $(2.38)_1$.

The second term $J\langle u^1_{\text{sc}}(\boldsymbol{r})\chi_{\mathcal{R}\setminus\mathcal{P}_1}(\boldsymbol{r})\rangle$ is more involved. In Appendix B.3 we prove this term has the reduced form (2.70). To calculate this term, first we use (2.23) together with (2.27) to obtain:

$$\langle u^1_{\text{sc}}(\boldsymbol{r})\rangle(\boldsymbol{r}_1) = \sum_n \langle f_n\rangle(\boldsymbol{r}_1)\mathrm{u}_n(k\boldsymbol{r} - k\boldsymbol{r}_1). \quad (2.40)$$

Following the method shown in [15], we re-expand the scattering coefficients of

[‡]We note that k can not equal k_p [18].

each particle in terms of a series of waves of the form:

$$\langle f_n \rangle(\boldsymbol{r}_1) = \sum_p f_{p,n}(\boldsymbol{r}_1), \tag{2.41}$$

where each $f_{p,n}$ satisfies a Helmholtz equation: $\nabla^2 f_{p,n}(\boldsymbol{r}_1) + k_p^2 f_{p,n}(\boldsymbol{r}_1) = 0$, and the k_p and $f_{p,n}$ are determined from the governing equation of $\langle f_n \rangle(\boldsymbol{r}_1)$. In [15] it is shown how such a series solution can be used for any material region, where [14] proves that (2.41) applies to plane-waves.

Using the effective wave series expansion (2.41) in (2.70) leads to:

$$J\langle u_{\text{sc}}^1(\boldsymbol{r})\chi_{\mathcal{R}\setminus\mathcal{P}_1}(\boldsymbol{r})\rangle = \mathfrak{n}\sum_{np}\int_{\mathcal{R}_1\setminus\mathcal{B}(\boldsymbol{r};a)} f_{p,n}(\boldsymbol{r}_1)\mathrm{u}_n(k\boldsymbol{r}-k\boldsymbol{r}_1)\mathrm{d}\boldsymbol{r}_1. \tag{2.42}$$

As shown in [15, Section 4], we can use Green's second identity to transform the integral in (2.42) into a more trackable form, which describes the interaction of the wave with the boundaries of $\mathcal{R}_1$ and the particles:

$$\int_{\mathcal{R}_1\setminus\mathcal{B}(\boldsymbol{r};a)} f_{p,n}(\boldsymbol{r}_1)\mathrm{u}_n(k\boldsymbol{r}-k\boldsymbol{r}_1)\mathrm{d}\boldsymbol{r}_1 = \frac{\mathcal{I}_{p,n}(\boldsymbol{r}) - \mathcal{J}_{p,n}(\boldsymbol{r})}{k^2 - k_p^2}, \tag{2.43}$$

where

$$\mathcal{I}_{p,n}(\boldsymbol{r}) = \int_{\partial\mathcal{R}_1} \frac{\partial f_{p,n}(\boldsymbol{r}_1)}{\partial\boldsymbol{\nu}_1}\mathrm{u}_n(k\boldsymbol{r}-k\boldsymbol{r}_1) - f_{p,n}(\boldsymbol{r}_1)\frac{\partial \mathrm{u}_n(k\boldsymbol{r}-k\boldsymbol{r}_1)}{\partial\boldsymbol{\nu}_1}\mathrm{d}A_1, \tag{2.44}$$

$$\mathcal{J}_{p,n}(\boldsymbol{r}) = \int_{\partial\mathcal{B}(\boldsymbol{0},a)} \frac{\partial f_{p,n}(\boldsymbol{r}-\boldsymbol{x}_1)}{\partial\boldsymbol{\nu}_1}\mathrm{u}_n(k\boldsymbol{x}_1) - f_{p,n}(\boldsymbol{r}-\boldsymbol{x}_1)\frac{\partial \mathrm{u}_n(k\boldsymbol{x}_1)}{\partial\boldsymbol{\nu}_1}\mathrm{d}A_1, \tag{2.45}$$

from which we can see that:

$$\nabla^2\mathcal{I}_{p,n}(\boldsymbol{r}) + k^2\mathcal{I}_{p,n}(\boldsymbol{r}) = 0 \;\text{ and }\; \nabla^2\mathcal{J}_{p,n}(\boldsymbol{r}) + k_p^2\mathcal{J}_{p,n}(\boldsymbol{r}) = 0.$$

So, clearly, $\mathcal{I}_{p,n}(\boldsymbol{r})$ contributes to $w_{\text{inc}}(\boldsymbol{r})$, while $\mathcal{J}_{p,n}(\boldsymbol{r})$ contributes to $w_p(\boldsymbol{r})$ in (2.37).

The third term in (2.36) is given by (2.77) in Appendix B.4, which after using (2.41) and (2.40) becomes:

$$\begin{aligned} J(J-1)\langle u_{\text{sc}}^1(\boldsymbol{r})\chi_{\mathcal{P}_2}(\boldsymbol{r})\rangle = \phi\mathfrak{n}\sum_{np}\int_{\mathcal{R}_1\setminus\mathcal{B}(\boldsymbol{r};b_{12}-a)} f_{np}(\boldsymbol{r}_1)\mathrm{u}_n(k\boldsymbol{r}-k\boldsymbol{r}_1)\mathrm{d}\boldsymbol{r}_1 \\ - \mathfrak{n}^2\sum_{np}\int_{\mathcal{B}(\boldsymbol{0};b_{12}+a)\setminus\mathcal{B}(\boldsymbol{0};a_{12}-a)} f_{p,n}(\boldsymbol{r}-\boldsymbol{x}_1)\mathrm{u}_n(k\boldsymbol{x}_1)G(\boldsymbol{x}_1)\mathrm{d}\boldsymbol{x}_1, \end{aligned} \tag{2.46}$$

where $G(\boldsymbol{x}_1)$ is defined in (2.78), although it is not required for our goals here.

The first integral in (2.46) is analogous to (2.43), so leads to terms of the form (2.37). The second of these integrals only has $\boldsymbol{r}$ dependence in $f_{p,n}(\boldsymbol{r}-\boldsymbol{x}_1)$, and therefore contributes to $w_p(\boldsymbol{r})$ in (2.37).

The fourth term in (2.36) is given by (2.62), which after using (2.24), (2.41) and the change of variables from $\boldsymbol{r}_1$ to $\boldsymbol{x}_1 = \boldsymbol{r} - \boldsymbol{r}_1$ becomes:

$$J\langle u^1_{\text{in}}(\boldsymbol{r})\chi_{\mathcal{P}_1}(\boldsymbol{r})\rangle = \mathfrak{n}\sum_{pn} b_n \int_{\mathcal{B}(\mathbf{0};a)} f_{p,n}(\boldsymbol{r}-\boldsymbol{x}_1)\mathrm{v}_n(k_o\boldsymbol{x}_1)\mathrm{d}\boldsymbol{r}_1, \tag{2.47}$$

which can only contribute to terms of the form $w_p(\boldsymbol{r})$ in (2.37).

2.4.2 The average of the incident field

In Section 2.4.1 we demonstrated that (2.31) is a sum of terms which satisfy the background and effective wave equations as shown in (2.37). The term w_{inc}, that satisfies the background wave equation, can be seen as what remains of the incident field. In much of the literature [7, 11, 25, 40, 45] it is simply assumed that $w_{\text{inc}} := 0$. This is often called the "extinction theorem", despite it being an assumption. In papers such as [30] that calculate the average field from first principles, it is not clear that $w_{\text{inc}} = 0$. Here we remove any doubt by proving that when sufficiently inside the material, given by condition (2.35), we have that $w_{\text{inc}} := 0$ for any incident field, any material region $\mathcal{R}$, any frequency, and all types of particles.

Using the results from Section 2.4.1, we collect the terms in (2.36) that satisfy the background wave equation to obtain:

$$w_{\text{inc}}(\boldsymbol{r}) = (1-\phi)u_{\text{inc}}(\boldsymbol{r}) + \sum_{pn}\frac{\mathfrak{n}(1-\phi)}{k^2-k_p^2}\mathcal{I}_{p,n}(\boldsymbol{r}). \tag{2.48}$$

Here we show that the right side of (2.48) is zero by using the ensemble boundary condition given by [15, Equation (4.8)]:

$$\sum_{n'}\mathcal{V}_{n'n}(k\boldsymbol{r}_1)g_{n'} + \mathfrak{n}\sum_{nn'p}\frac{\mathcal{I}_{p,n'n}(\boldsymbol{r}_1)}{k^2-k_p^2} = 0, \tag{2.49}$$

where

$$\mathcal{I}_{p,n'n}(\boldsymbol{r}_1) = \int_{\partial\mathcal{R}_1}\mathcal{U}_{n'n}(k\boldsymbol{r}_1-k\boldsymbol{r}_2)\frac{\partial f_{p,n'}(\boldsymbol{r}_2)}{\partial\boldsymbol{\nu}_2} - \frac{\partial\mathcal{U}_{n'n}(k\boldsymbol{r}_1-k\boldsymbol{r}_2)}{\partial\boldsymbol{\nu}_2}f_{p,n'}(\boldsymbol{r}_2)\mathrm{d}A_2, \tag{2.50}$$

with $\boldsymbol{r}_2$ being the variable of integration and $\boldsymbol{\nu}_2$ the normal to the boundary $\partial\mathcal{R}_1$, and the g_n are the coefficients of the incident wave:

$$u_{\text{inc}}(\boldsymbol{r}) = \sum_n g_n \mathrm{v}_n(k\boldsymbol{r}). \tag{2.51}$$

Equation (2.51) assumes the source of the incident wave is outside of the region where the particles are [15]. The other assumptions needed to deduce the ensemble boundary conditions (2.49) are the same assumptions we have used for the calculations in this paper, except the boundary condition is only valid when:

$$\min_{\boldsymbol{r}_2 \in \partial\mathcal{R}_1} |\boldsymbol{r}_1 - \boldsymbol{r}_2| \geq a_{12}. \tag{2.52}$$

To start the demonstration, we multiply both sides of (2.49) by $\mathrm{v}_n(k\boldsymbol{r} - k\boldsymbol{r}_1)$ and sum over n to obtain:

$$\sum_{nn'} \mathcal{V}_{n'n}(k\boldsymbol{r}_1) g_{n'} \mathrm{v}_n(k\boldsymbol{r} - k\boldsymbol{r}_1) + \mathfrak{n} \sum_{nn'p} \frac{\mathcal{I}_{p,n'n}(\boldsymbol{r}_1)}{k^2 - k_p^2} \mathrm{v}_n(k\boldsymbol{r} - k\boldsymbol{r}_1) = 0. \tag{2.53}$$

Now, (2.53) can be simplified by using the fundamental property of translation matrices that

$$\begin{cases} \mathrm{v}_n(k\boldsymbol{r} + k\boldsymbol{d}) = \displaystyle\sum_{n'} \mathcal{V}_{nn'}(k\boldsymbol{d}) \mathrm{v}_{n'}(k\boldsymbol{r}), & \text{for all } \boldsymbol{d}, \\ \mathrm{u}_n(k\boldsymbol{r} + k\boldsymbol{d}) = \displaystyle\sum_{n'} \mathcal{U}_{nn'}(k\boldsymbol{d}) \mathrm{v}_{n'}(k\boldsymbol{r}), & |\boldsymbol{r}| < |\boldsymbol{d}|. \end{cases} \tag{2.54}$$

Using the property of the translation matrices (2.54) together with (2.51), we see that:

$$\sum_{nn'} \mathcal{V}_{n'n}(k\boldsymbol{r}_1) g_{n'} \mathrm{v}_n(k\boldsymbol{r} - k\boldsymbol{r}_1) = \sum_n g_n \mathrm{v}_n(k\boldsymbol{r}) = u_{\text{inc}}(\boldsymbol{r}), \tag{2.55}$$

in accordance with [15, Equation (2.3)].

Next, by choosing $\boldsymbol{r}$ such that (2.35) is satisfied, it is then possible to choose $\boldsymbol{r}_1$ so that the condition (2.52) is true and such that:

$$|\boldsymbol{r} - \boldsymbol{r}_1| < |\boldsymbol{r}_1 - \boldsymbol{r}_2|, \quad \text{for every} \quad \boldsymbol{r}_2 \in \partial\mathcal{R}_1.$$

This enables us to use the translation property (2.54) in (2.50) to obtain:

$$\sum_n \mathcal{I}_{p,n'n}(\boldsymbol{r}_1)\mathrm{v}_n(k\boldsymbol{r}-k\boldsymbol{r}_1) =$$
$$\int_{\partial\mathcal{R}_1} \sum_n \mathrm{v}_n(k\boldsymbol{r}-k\boldsymbol{r}_1)\mathcal{U}_{n'n}(k\boldsymbol{r}_1-k\boldsymbol{r}_2)\frac{\partial f_{p,n'}(\boldsymbol{r}_2)}{\partial\boldsymbol{\nu}_2} - \sum_n \mathrm{v}_n(k\boldsymbol{r}-k\boldsymbol{r}_1)\frac{\partial\mathcal{U}_{n'n}(k\boldsymbol{r}_1-k\boldsymbol{r}_2)}{\partial\boldsymbol{\nu}_2} f_{p,n'}(\boldsymbol{r}_2)\mathrm{d}A_2$$
$$= \int_{\partial\mathcal{R}_1} \mathrm{u}_{n'}(k\boldsymbol{r}-k\boldsymbol{r}_2)\frac{\partial f_{p,n'}(\boldsymbol{r}_2)}{\partial\boldsymbol{\nu}_2} - \frac{\partial \mathrm{u}_{n'}(k\boldsymbol{r}-k\boldsymbol{r}_2)}{\partial\boldsymbol{\nu}_2} f_{p,n'}(\boldsymbol{r}_2)\mathrm{d}A_2 = \mathcal{I}_{p,n'}(\boldsymbol{r}). \quad (2.56)$$

Substituting (2.55) and (2.56) into (2.53) leads to:

$$u_{\mathrm{inc}}(\boldsymbol{r}) + \mathfrak{n}\sum_{n'p}\frac{\mathcal{I}_{p,n'}(\boldsymbol{r})}{k^2-k_p^2} = 0. \quad (2.57)$$

Finally, substituting (2.57) into (2.48), we conclude the extinction theorem $w_{\mathrm{inc}}(\boldsymbol{r}) = 0$ for $\boldsymbol{r}$ that satisfies (2.35). That is, there is no term in the average transmitted wave that satisfies the background wave equation.

2.5 Conclusions

The initial goal of this work was to find clear evidence that there exist at least two effective wavenumbers in an averaged particulate material. It is highly unusual to have two different wavenumbers for an isotropic homogeneous media supporting only scalar waves. However theoretical works [14, 15, 16, 50, 51, 52] have predicted the existence of at least two effective wavenumbers, and their presence changes the overall transmitted and reflected waves.

Monte-Carlo results. To verify the existence of multiple effective wavenumbers we used very precise simulations that calculated scattered waves from different particle configurations and then took an average over the different particle configurations. This turned out to be far more computationally expensive than we expected, and required extensive and careful analysis. To summarise, Figure 2.8 clearly shows that there are two separate wavenumbers that contribute to the field, and that the wavenumbers predicted by the Monte-Carlo method are similar to the wavenumbers predicted by the theory.

When it matters. A natural question that appeared during this work was how to find the parameters that led to multiple effective wavenumbers. That is, for what scenarios will the classical theory that uses only one effective wavenumber [7, 26, 27, 30, 33, 48] be inaccurate? Previous work [15, 16] demonstrated that there is a

dispersion equation (2.13) which provides the effective wavenumbers k_p, and that if there is only one wavenumber k_1 with an imaginary part much small than all others Im $k_1 \ll$ Im k_p for $p = 2, \ldots$, then the classical theory will be accurate.

However, solving the dispersion equation (2.13) can be time-consuming, especially for higher frequencies and a wide range of parameters. When plotting the regions where multiple wavenumbers appear we saw a clear pattern shown in Figure 2.1: particles which are strong scatterers lead to multiple effective wavenumbers. In Figure 2.1 the green curves show the scattering strength of just one particle (2.18). Finding the parameters that lead one particle to be a strong scatterer is far more practical than solving the dispersion equation (2.13), and proved to be a surprisingly good measure. To summarise: strong multiple scattering triggers multiple effective wavenumbers.

Resonators. In the field of metamaterials, strong scatterers such as resonators are often used to tailor the overall behaviour of the material [2]. Using this strategy for disordered, or random, particulates will lead to multiple effective wavenumbers, and will complicate how to predict the overall properties of the material. To truly understand the effect of these resonators it is first necessary to plot their dispersion diagrams by solving the dispersion equation (2.13) with the T-matrix T_n depending on the type of particle used. An example of such a diagram is given in Figure 2.5.

The theoretical results. When deciding how best to sample the transmitted field, we realised that within the theoretical formulation for ensemble averaging particulates, it was not clear that the transmitted wave is a sum of waves with effective wavenumbers. This led us to derive the missing results and provide a general proof about the incident and transmitted waves.

Proof of extinction. It is often assumed that the average field inside a random material does not contain any remnant of the incident wave. This is called the Ewald-Oseen extinction theorem, but as far as the authors are aware, there is no proof of this conjecture for particulate materials. In this work, we were able to prove this extinction theorem for any particulate (for scalar isotropic waves), any frequency, and material geometry. The proof is given in Section 2.4, with the final equation that proves extinction being (2.57). The proof also provides the extinction length: the distance required for the incident wave to travel with the material until it is extinct. We proved that the extinction length is equal to the correlation length plus the particle radius $b_{12} + a$, see equation (2.11) where these quantities are relative to the pair-correlation.

Proof of transmitted effective waves. The same proof for extinction also served to prove that the average transmitted field is a sum of effective waves, when the

distance from the material boundary is greater than the extinction length. The proof is shown in Section 2.4. We note that particularly in the field of continuously varying random media [7, 49], it is assumed that the average transmitted field satisfies an effective wave equation. By proving this for particulates, from a microscopic approach, we provide a link between the two approaches.

Future avenues. This work shows that using Monte-Carlo simulations to approximate a semi-infinite media, such as a plate, filled with particles, is still computationally challenging. We feel that future work focused on validating effective theories for particulates should focus on finite materials (in the computational sense), such as a cylinder filled with cylindrical particles and a sphere filled with spherical particles. There is a theoretical framework to validate against [15]. In terms of theoretical developments, our work has shown a connection between the particulate microscopic approach to effective waves [15, 33, 34, 40, 46] and approaches for continuously varying random media [7, 49]. That is, we demonstrate the effective wave series used in the macroscopic approach given by (2.41) does lead to the average transmitted wave being a sum of effective waves, as illustrated by (2.37). We believe the calculations we provide now pave the way to answer the following open question: are the two approaches equivalent?

Author contributions

AK conceived of the study, drafted the manuscript, wrote all the code for the numerical calculations, developed the theoretical calculations, and produced all the figures. ALG helped conceive the study, edited the manuscript, assisted with and verified the theoretical calculations. PSP assisted with the projection method and with the figures related to this method, verified the calculations, and edited the manuscript.

Data and reproducibility

To produce our results we used the open source software [17], [19], [35].

A The Monte-Carlo methodology

Here we present more details on how we performed the Monte-Carlo simulations, and analysed the results. For a reference on Monte-Carlo methods we refer to the book [45].

To compute the ensemble average wave (2.9) with Monte-Carlo simulations, the waves scattered by particles within a plate geometry (as shown in Figure 2.2) have to be simulated tens of thousands of times, with each simulation having hundreds of particles, before the standard error of the mean converges [31]. For each simulation we calculate exactly how the incident wave $u_{\text{inc}}(x) = \mathrm{e}^{\mathrm{i}kx}$ scatters from all the particles. For these reasons, careful considerations are needed to determine how to perform the Monte-Carlo simulations.

In order, we explain how we created each particle configuration, how we determined the plate width and height, including consideration of convergence, and finally, how we analysed the data.

Sequential addition. To place the particles we use the strategy of sequential addition as described in [45, Chapter 8, Section 2]. In essence, we place one particle at a time according to a random uniform distribution. If the particle overlaps with another particle it is rejected. The process is repeated until we obtain a desired particle volume fraction ϕ.

The plate width. Choosing an appropriate width W for the plate $\mathcal{R}$ was based on two factors:

- The result from the theory shown by (2.12) predicts the plate needs to have a width $W > 2a + 2b_{12}$ for $\langle u(x) \rangle$ to be exactly equal to a sum of effective waves. The minimum value for b_{12} is a_{12}, which we found to be accurate enough for our tolerances. Using $b_{12} = a_{12} > 2a$ implies that we need a plate with $W > 6a = 7.2$, as we used $a = 1.2$ for all numerical experiments.
- The plate width W can not be too wide, otherwise the average wave $\langle u(x) \rangle$ will be completely attenuated, which is a computational waste. Also, in the region where the wave is completely attenuated it is impossible to estimate the k_p by fitting the formula (2.12). Materials, and frequencies, that lead to (2.12) needing more than one effective wavenumber k_1 to accurately approximate $\langle u(x) \rangle$ are highly attenuating materials. See Figure 2.7 for an illustration of the region where we fit the formula (2.12).

The plate height. If the plate filled with particles, as shown in Figure 2.2, was infinite in height, and the particles were excited by a plane-wave, then the average

wave $\langle u(x)\rangle$ would be exactly a sum of plane-waves given by (2.12). See [15] for details. In practice, it is not of course possible to exactly simulate the wave scattered from an infinite plate filled with one specific arrangement of particles. The approximation often used is to have a cell filled with a random set of particles, and then to use periodic tiling of this cell [8]. To avoid the artefacts produced by periodic tiling we perform a convergence study to determine at what height a plate filled with particles behaves approximately like a plate of infinite size.

Let H be the height of the plate, which is illustrated in Figure 2.2. To determine the size needed for H, we first choose a large value $H = 600$, with the plate width $W = 20$, and then fill this plate with one configuration of particles Λ, according to the sequential addition method. We then calculate the total wave at:

$$u\left(x, 0\right) \quad \text{for the values} \quad 2a \leq x \leq W - 2a, \tag{2.58}$$

to create a function $\mathbf{U}_{600}(x)$. To determine the influence of H, we then reduce the height. For example, we use $H = 590$ and remove from Λ any particles that are now outside of the box with the reduced height. We then take the updated configuration of particles Λ and recalculate the total wave in the same region to create the function $\mathbf{U}_{590}(x)$.

For a range of heights we compute the relative error:

$$\text{Error \%} = 100\frac{\|\mathbf{U}_H(x) - \mathbf{U}_{600}(x)\|}{\|\mathbf{U}_{600}(x)\|}. \tag{2.59}$$

By calculating these errors for a range of heights we can plot the error against the height as shown in Figure 2.11.

For sound-soft particles, see Table 2.1 for details, and frequency $ka = 0.3$, we see that the errors have converged. This means that $\mathbf{U}_{600}(x)$ is approximately the same as $\mathbf{U}_\infty(x)$, and we can estimate that the height of the plate has to be approximately $H = 400$ for the scattered waves to have an error of less than 1% in comparison to $\mathbf{U}_\infty(x)$.

For sound-hard particles, see Table 2.1 for details, and $ka = 0.3$, the errors have not converged as can be seen from Figure 2.11, even for very large heights. This means it is unclear what is the error relative to an infinite plate $\mathbf{U}_\infty$. For this reason, we do not focus on this case, and only perform one simulation with $H = 400$. Our hypothesis is that the plane-wave when scattered from the corner of the plate leads to a transmitted wave that travels down inside the plate relatively unobstructed, as these

types of particles are weak scatterers.

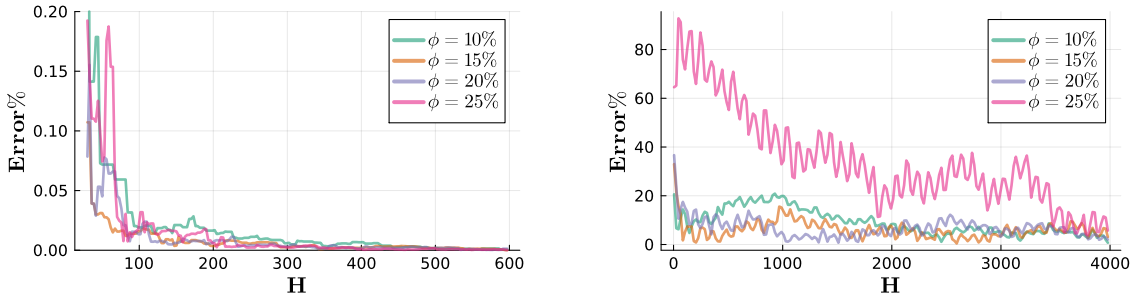

(a) Sound-soft particles (b) Sound-hard particles

Figure 2.11: Shows the rate of convergence which can be described with the normalised difference between the scattered waves (2.59) with respect to the height of the plate **H**.

When fitting for the effective wavenumbers, we need to consider how the errors due to truncating the height of the plate may affect the fitting and the acceptable fit errors.

Analysing the data. We generate Monte-Carlo simulations for the different cases presented in Section 2.3.1 with a plate of width $W = 20$ and height $H = 400$. The data from Monte-Carlo results for the transmitted wave (2.12) is of the form:

$$\langle u(x,0;\Lambda)\rangle = \sum_{p=1}^{P} \left(A_p^+ \mathrm{e}^{\mathrm{i}k_p x} + A_p^- \mathrm{e}^{-\mathrm{i}k_p x}\right) + \epsilon(x), \quad \text{for } 2a \le x \le W - 2a,$$

where $\epsilon(x)$ is a small error that falls inside the standard error of the mean. For the cases where only one effective wavenumber was predicted, the average wave $\langle u(x,0;\Lambda)\rangle$ is fitted well by (2.1), using nonlinear optimisation libraries in Julia [35].

For every wavenumber k_p there are potentially two waves: one travelling towards the positive x - direction and another travelling in the negative x - direction. For the cases where the average wave is completely attenuated when it reaches the edge of the plate, $x = 20$, we should have $A_p^- = 0$, suppressing the wave travelling in the negative x-direction.

From the Monte-Carlo data for cases with more than one effective wavenumber, we find that $\langle u(x,0;\Lambda)\rangle$ is below the standard error of the mean for $x \ge 15$. For this reason, we can take $A_p^- = 0$ and fit it only for A_p^+ and k_p. That is we fit to the Monte-Carlo data functions of the form:

$$h(x) = \sum_{p=1}^{P} A_p^+ \mathrm{e}^{\mathrm{i}k_p x}, \qquad \text{for } 4 \le x \le 15, \tag{2.60}$$

with $\mathrm{Im}[k_p] > 0$. In the case presented in Figure 2.7a the transmitted wave attenuates quicker, therefore we focus the fitting on a narrower range, $4 \leq x \leq 10$.

Another reason to use (2.60), is that fitting for A_p^+, A_p^-, and k_p in the case of multiple effective wavenumbers can become ill-posed. This is related to how inverting a Laplace transform is ill-posed, see [21, Section 2.1]. That is, the more terms included in the sum shown in (2.12) the more ill-posed is the problem of recovering the k_p, A_p^+, and A_p^- from data of the average wave $\langle u(x, 0; \Lambda)\rangle$.

Smoothing Process. The smoothing process involves applying a moving average filter to our data indicating whether certain wavenumbers go out of the likelihood or not. Here is how the smoothing works in detail [1, 39]:

Algorithm 2: Data Smoothing Algorithm

Data: InputMatrix of size $M \times N$, WindowSize: Integer
Result: SmoothedMatrix of size $M \times N$
Function `SmoothData`(*InputMatrix, WindowSize*)**:**
  Initialise SmoothedMatrix of size $M \times N$
  for $i = 1$ **to** N **do**
    for $j = 1$ **to** M **do**
      $\mathrm{s}_i = \max(1, i - WindowSize)$
      $\mathrm{e}_i = \min(N, i + WindowSize)$
      $\mathrm{s}_j = \max(1, j - WindowSize)$
      $\mathrm{e}_j = \min(M, j + WindowSize)$
      SmoothedMatrix[i, j] $= \dfrac{\mathrm{sum}(\mathrm{InputMatrix}[\mathrm{s}_i : \mathrm{e}_i, \mathrm{s}_j : \mathrm{e}_j])}{(\mathrm{e}_i - \mathrm{s}_i + 1) \times (\mathrm{e}_j - \mathrm{s}_j + 1)}$
    end
  end
  return *SmoothedMatrix*

- A new matrix of the same size and type as the input data is initialised to store the smoothed values.
- The function iterates over each element in the input matrix. For each element at position (i, j), it calculates a rectangular window centred around this element. The bounds of the window are calculated such that it stays within the limits of the matrix. This step ensures that the window does not try to access data outside the matrix boundaries.
- Inside the determined window, the function computes the average value of the elements. This is achieved by summing all the elements within the window and then dividing by the total number of elements in that window. The division operation is an integer division which means that the result is the integer part of

the quotient, effectively disregarding any remainder.

- The computed average value is then assigned to the corresponding element in the matrix. This process is repeated for every element in the input matrix, resulting in a smoothed output matrix.
- The parameter responsible for the size of the window controls the extent of smoothing. A larger window size results in more aggressive smoothing because it averages over a larger area, thereby reducing the impact of outliers or noise on a larger scale. Conversely, a smaller window size results in less aggressive smoothing, preserving more of the original detail in the data.

Computational time. Our study utilises high-fidelity Monte-Carlo simulations, whose computational cost was significant. This limits the number of cases we could investigate with Monte-Carlo. For example, we needed to execute 40,000 simulations for scenarios depicted in Figures 2.7, 2.8 and 2.9. Each simulation involves hundreds of particles, and is computationally demanding especially at higher frequencies denoted by ka. To manage this, we employed parallel processing across multiple processors. For instance, simulating sound-soft particles at a frequency of $ka = 0.36$ requires about 72 hours for completion on an 11th Gen. Intel Core i7 with 8 cores. So without parallel processing, the runtime would increase by at least eight-fold.

B The ensemble average transmission

Here we reduce the terms in (2.31) to reach equation (2.36). For this section we use the notation and assumptions introduced in Section 2.4.

In many calculations throughout this section, for any function f which depends on particle configuration, we use that:

$$J\langle \mathrm{f}\rangle = J\int_{\mathcal{R}_1^J} \mathrm{f}\ \mathrm{p}(\boldsymbol{r}_1,\dots,\boldsymbol{r}_J)\mathrm{d}\boldsymbol{r}_1\cdots\mathrm{d}\boldsymbol{r}_J$$
$$= \mathfrak{n}\int_{\mathcal{R}_1^J} \mathrm{f}\ \mathrm{p}(\boldsymbol{r}_2,\dots,\boldsymbol{r}_J|\boldsymbol{r}_1)\mathrm{d}\boldsymbol{r}_1\cdots\mathrm{d}\boldsymbol{r}_J = \mathfrak{n}\int_{\mathcal{R}_1} \langle \mathrm{f}\rangle(\boldsymbol{r}_1)\mathrm{d}\boldsymbol{r}_1, \quad (2.61)$$

where we used, in order, the definitions (2.26) and (2.28) and (2.32). If the f only depends on $\boldsymbol{r}_1$, then we further have that $\langle \mathrm{f}\rangle(\boldsymbol{r}_1) = \mathrm{f}$ because:

$$\int_{\mathcal{R}_1^{J-1}} \mathrm{p}(\boldsymbol{r}_2,\dots,\boldsymbol{r}_J|\boldsymbol{r}_1)\mathrm{d}\boldsymbol{r}_2\cdots\mathrm{d}\boldsymbol{r}_J = 1,$$

which is true for any joint probability density.

B.1 The transmitted internal field

We start by calculating the simplest term. Using (2.24), the definitions of the ensemble average (2.27) and (2.26), then (2.61) leads to:

$$J\langle u_{\rm in}^1(\boldsymbol{r})\chi_{\mathcal{P}_1}(\boldsymbol{r})\rangle = \mathfrak{n}\int_{\mathcal{B}(\boldsymbol{r};a)}\langle u_{\rm in}^1(\boldsymbol{r})\rangle(\boldsymbol{r}_1)\mathrm{d}\boldsymbol{r}_1, \tag{2.62}$$

where the ball $\mathcal{B}(\boldsymbol{r};a)$ is defined by (2.39), and we use the assumption (2.35).

B.2 The transmitted incident field

The next simplest computation is the ensemble average of the incident wave term in (2.31). To do this we will demonstrate the following equalities:

$$\langle u_{\rm inc}(\boldsymbol{r})\chi_{\mathcal{R}\setminus\mathcal{P}}(\boldsymbol{r})\rangle = u_{\rm inc}(\boldsymbol{r})\langle\chi_{\mathcal{R}\setminus\mathcal{P}}(\boldsymbol{r})\rangle = u_{\rm inc}(\boldsymbol{r})\langle 1-\chi_{\mathcal{P}}(\boldsymbol{r})\rangle = u_{\rm inc}(\boldsymbol{r})(1-\phi), \tag{2.63}$$

where ϕ is the particle volume fraction defined by (2.33).

First, we use the ensemble average (2.26), then take $u_{\rm inc}(\boldsymbol{r})$ outside of the integrals, as it does not depend on the particle positions, to reach:

$$\langle u_{\rm inc}(\boldsymbol{r})\chi_{\mathcal{R}\setminus\mathcal{P}}(\boldsymbol{r})\rangle = u_{\rm inc}(\boldsymbol{r})\langle\chi_{\mathcal{R}\setminus\mathcal{P}}(\boldsymbol{r})\rangle. \tag{2.64}$$

To calculate the ensemble average on the right we use:

$$\chi_{\mathcal{R}\setminus\mathcal{P}}(\boldsymbol{r}) = 1-\chi_{\mathcal{P}}(\boldsymbol{r}), \tag{2.65}$$

leading to:

$$\langle\chi_{\mathcal{R}\setminus\mathcal{P}}(\boldsymbol{r})\rangle = \langle 1\rangle - \langle\chi_{\mathcal{P}}(\boldsymbol{r})\rangle = 1-\sum_j\langle\chi_{\mathcal{P}_j}(\boldsymbol{r})\rangle, \tag{2.66}$$

where we used the definition that integrating a probability density function p over all its variables gives 1, and:

$$\chi_{\mathcal{P}}(\boldsymbol{r})\mathrm{p}(\boldsymbol{r}_1,\boldsymbol{r}_2,\ldots,\boldsymbol{r}_J) = \sum_{j=1}^{J}\chi_{\mathcal{P}_j}(\boldsymbol{r})\mathrm{p}(\boldsymbol{r}_1,\boldsymbol{r}_2,\ldots,\boldsymbol{r}_J), \tag{2.67}$$

which holds because if any two particles overlap, we have that $\mathrm{p}(\boldsymbol{r}_1,\boldsymbol{r}_2,\ldots,\boldsymbol{r}_J)=0$. Therefore, if $\chi_{\mathcal{P}_j}(\boldsymbol{r})=1$, then $\chi_{\mathcal{P}_\ell}(\boldsymbol{r})=0$ for $\ell\neq j$.

Next, we use that particles are indistinguishable, except for their positions, so after

ensemble averaging $\langle \chi_{\mathcal{P}_j}(\boldsymbol{r})\rangle = \langle \chi_{\mathcal{P}_1}(\boldsymbol{r})\rangle$ for every j, which together with (2.61) leads to:

$$\langle \chi_{\mathcal{P}}(\boldsymbol{r})\rangle = \sum_{j=1}^{J}\langle \chi_{\mathcal{P}_j}(\boldsymbol{r})\rangle = J\langle \chi_{\mathcal{P}_1}(\boldsymbol{r})\rangle = \mathfrak{n}\int_{\mathcal{R}_1}\chi_{\mathcal{P}_1}(\boldsymbol{r})\mathrm{d}\boldsymbol{r}_1 = \mathfrak{n}\int_{\mathcal{B}(\boldsymbol{r},a)}\mathrm{d}\boldsymbol{r}_1 = \phi, \tag{2.68}$$

where we used (2.39) and (2.35).

B.3 The transmitted scattered field

The most involved term to calculate in (2.31) is $\langle u_{\mathrm{sc}}(\boldsymbol{r})\chi_{\mathcal{R}\setminus\mathcal{P}}(\boldsymbol{r})\rangle$, which will require that we demonstrate the following steps:

$$\begin{aligned}\langle u_{\mathrm{sc}}(\boldsymbol{r})\chi_{\mathcal{R}\setminus\mathcal{P}}(\boldsymbol{r})\rangle &= \sum_{j}\langle u^j_{\mathrm{sc}}(\boldsymbol{r})\chi_{\mathcal{R}\setminus\mathcal{P}}(\boldsymbol{r})\rangle = J\langle u^1_{\mathrm{sc}}(\boldsymbol{r})\chi_{\mathcal{R}\setminus\mathcal{P}}(\boldsymbol{r})\rangle = J\langle u^1_{\mathrm{sc}}(\boldsymbol{r})\prod_{j=1}^{J}\chi_{\mathcal{R}\setminus\mathcal{P}_j}(\boldsymbol{r})\rangle\\ &= J\langle u^1_{\mathrm{sc}}(\boldsymbol{r})\chi_{\mathcal{R}\setminus\mathcal{P}_1}(\boldsymbol{r})\rangle - J\sum_{j=2}^{J}\langle u^1_{\mathrm{sc}}(\boldsymbol{r})\chi_{\mathcal{P}_j}(\boldsymbol{r})\rangle\\ &= J\langle u^1_{\mathrm{sc}}(\boldsymbol{r})\chi_{\mathcal{R}\setminus\mathcal{P}_1}(\boldsymbol{r})\rangle - J(J-1)\langle u^1_{\mathrm{sc}}(\boldsymbol{r})\chi_{\mathcal{P}_2}(\boldsymbol{r})\rangle.\end{aligned} \tag{2.69}$$

The first three equalities in (2.69) are a result of using, in order, (2.23), that particles are indistinguishable, and:

$$\chi_{\mathcal{R}\setminus\mathcal{P}}(\boldsymbol{r})\mathrm{p}(\boldsymbol{r}_1,\boldsymbol{r}_2,\ldots,\boldsymbol{r}_J) = \prod_{j=1}^{J}\chi_{\mathcal{R}\setminus\mathcal{P}_j}(\boldsymbol{r})\mathrm{p}(\boldsymbol{r}_1,\boldsymbol{r}_2,\ldots,\boldsymbol{r}_J),$$

which is a result of $\mathrm{p}(\boldsymbol{r}_1,\boldsymbol{r}_2,\ldots,\boldsymbol{r}_J) = 0$ when any two particles overlap.
The non-overlapping of particles also leads to:

$$\chi_{\mathcal{R}\setminus\mathcal{P}_1}(\boldsymbol{r})\prod_{j=2}^{J}\chi_{\mathcal{R}\setminus\mathcal{P}_j}(\boldsymbol{r})\mathrm{p}(\boldsymbol{r}_1,\boldsymbol{r}_2,\ldots,\boldsymbol{r}_J) = \left[\chi_{\mathcal{R}\setminus\mathcal{P}_1}(\boldsymbol{r}) - \sum_{j=2}^{J}\chi_{\mathcal{P}_j}(\boldsymbol{r})\right]\mathrm{p}(\boldsymbol{r}_1,\boldsymbol{r}_2,\ldots,\boldsymbol{r}_J),$$

which we use to conclude the second line in (2.69), and the third line is just a result of particles being indistinguishable again.

We proceed by simplifying the last two terms in (2.69). Using (2.61) we can reach:

$$J\langle u^1_{\mathrm{sc}}(\boldsymbol{r})\chi_{\mathcal{R}\setminus\mathcal{P}_1}(\boldsymbol{r})\rangle = \mathfrak{n}\int_{\mathcal{R}_1}\langle u^1_{\mathrm{sc}}(\boldsymbol{r})\rangle(\boldsymbol{r}_1)\chi_{\mathcal{R}\setminus\mathcal{P}_1}(\boldsymbol{r})\mathrm{d}\boldsymbol{r}_1 = \mathfrak{n}\int_{\mathcal{R}_1\setminus\mathcal{B}(\boldsymbol{r};a)}\langle u^1_{\mathrm{sc}}(\boldsymbol{r})\rangle(\boldsymbol{r}_1)\mathrm{d}\boldsymbol{r}_1, \tag{2.70}$$

where $\langle u^1_{\mathrm{sc}}(\boldsymbol{r})\rangle(\boldsymbol{r}_1)$ is given by (2.40).

For the last term in (2.69), we further use:

$$\mathrm{p}(\boldsymbol{r}_2,\ldots,\boldsymbol{r}_J|\boldsymbol{r}_1)=\mathrm{p}(\boldsymbol{r}_2|\boldsymbol{r}_1)\mathrm{p}(\boldsymbol{r}_3,\ldots,\boldsymbol{r}_J|\boldsymbol{r}_1,\boldsymbol{r}_2),$$

(2.23), (2.27), and the definition of $\langle f_n\rangle(\boldsymbol{r}_1,\boldsymbol{r}_2)$ given by [15, Equation (3.10) and (3.11)], followed by analogous steps shown in (2.40), to obtain:

$$J\langle u^1_{\mathrm{sc}}(\boldsymbol{r})\chi_{\mathcal{P}_2}(\boldsymbol{r})\rangle=\mathfrak{n}\sum_n\int_{\mathcal{R}_1^2}\langle f_n\rangle(\boldsymbol{r}_1,\boldsymbol{r}_2)\mathrm{u}_n(k\boldsymbol{r}-k\boldsymbol{r}_1)\mathrm{p}(\boldsymbol{r}_2|\boldsymbol{r}_1)\chi_{\mathcal{P}_2}(\boldsymbol{r})\mathrm{d}\boldsymbol{r}_1\mathrm{d}\boldsymbol{r}_2. \tag{2.71}$$

To simplify (2.71) we first use the Quasi-Crystalline Approximation (QCA):

$$\langle f_n\rangle(\boldsymbol{r}_1,\boldsymbol{r}_2)\approx\langle f_n\rangle(\boldsymbol{r}_1), \tag{2.72}$$

which is needed to deduce effective wavenumbers [15, 27, 29].

Before we show how to simplify (2.71) for a general pair-correlation g, we first deduce the results for the simplest pair-correlation called Hole-Correction. It is far easier to understand this case first. The Hole-Correction approximation is the result of taking $b_{12}=a_{12}$ in the general pair-correlation (2.11).

Using (2.72) and (2.34) in the integral (2.71), and swapping the order of integration leads to:

$$J(J-1)\langle u^1_{\mathrm{sc}}(\boldsymbol{r})\chi_{\mathcal{P}_2}(\boldsymbol{r})\rangle=\mathfrak{n}^2\int_{\mathcal{R}_1}\langle u^1_{\mathrm{sc}}(\boldsymbol{r})\rangle(\boldsymbol{r}_1)\int_{\mathcal{R}_1}\chi_{\mathcal{P}_2}(\boldsymbol{r})\mathrm{g}(|\boldsymbol{r}_1-\boldsymbol{r}_2|)\mathrm{d}\boldsymbol{r}_2\mathrm{d}\boldsymbol{r}_1. \tag{2.73}$$

Next we use $b_{12}=a_{12}$ and (2.11) which implies that:

$$\mathrm{g}(|\boldsymbol{r}_1-\boldsymbol{r}_2|)=\chi_{\mathcal{R}_1\setminus\mathcal{B}(\boldsymbol{r}_1;a_{12})}(\boldsymbol{r}_2),$$

which we substitute into (2.73) to reach:

$$J(J-1)\langle u^1_{\mathrm{sc}}(\boldsymbol{r})\chi_{\mathcal{P}_2}(\boldsymbol{r})\rangle=\mathfrak{n}^2\int_{\mathcal{R}_1}\langle u^1_{\mathrm{sc}}(\boldsymbol{r})\rangle(\boldsymbol{r}_1)\int_{\mathcal{B}(\boldsymbol{r};a)\setminus\mathcal{B}(\boldsymbol{r}_1;a_{12})}\mathrm{d}\boldsymbol{r}_2\mathrm{d}\boldsymbol{r}_1, \tag{2.74}$$

where we used that $\mathcal{B}(\boldsymbol{r};a)$ is completely contained in $\mathcal{R}_1$ for every $\boldsymbol{r}_2$ due to (2.35). There are values for $\boldsymbol{r}_1$ for which the integral in (2.74) is zero. To see this we note

$$\boldsymbol{r}_2\in\mathcal{B}(\boldsymbol{r};a)\implies|\boldsymbol{r}_2-\boldsymbol{r}|\leq a\quad\text{and}\quad\boldsymbol{r}_2\notin\mathcal{B}(\boldsymbol{r}_1;a_{12})\implies|\boldsymbol{r}_2-\boldsymbol{r}_1|>a_{12}.$$

Then, from the triangular inequality we have:

$$|\boldsymbol{r}_1 - \boldsymbol{r}| \geq |\boldsymbol{r}_1 - \boldsymbol{r}_2| - |\boldsymbol{r}_2 - \boldsymbol{r}| > a_{12} - a.$$

The above implies that the region of integration for $\boldsymbol{r}_1$ is just $\mathcal{R}_1 \setminus \mathcal{B}(\boldsymbol{r}; a_{12} - a)$. We now further split this region of integration into two disjoint regions: the first is $\mathcal{R}_1 \setminus \mathcal{B}(\boldsymbol{r}; a_{12} + a)$ and the second is $\mathcal{B}(\boldsymbol{r}; a_{12} + a) \setminus \mathcal{B}(\boldsymbol{r}; a_{12} - a)$.

For the first region $\boldsymbol{r}_1 \in \mathcal{R}_1 \setminus \mathcal{B}(\boldsymbol{r}; a_{12} + a)$ implies that $|\boldsymbol{r}_1 - \boldsymbol{r}| \geq a_{12} + a$, which together with $\boldsymbol{r}_2 \in \mathcal{B}(\boldsymbol{r}; a)$ leads to:

$$|\boldsymbol{r}_1 - \boldsymbol{r}_2| \geq |\boldsymbol{r}_1 - \boldsymbol{r}| - |\boldsymbol{r} - \boldsymbol{r}_2| > a_{12},$$

due to the triangle inequality. In other words, the region of integration for $\boldsymbol{r}_2$ becomes $\boldsymbol{r}_2 \in \mathcal{B}(\boldsymbol{r}; a) \setminus \mathcal{B}(\boldsymbol{r}_1; a_{12}) = \mathcal{B}(\boldsymbol{r}; a)$.

For the second region $\boldsymbol{r}_1 \in \mathcal{B}(\boldsymbol{r}; a_{12} + a) \setminus \mathcal{B}(\boldsymbol{r}; a_{12} - a)$, which implies that:

$$a < a_{12} - a \leq |\boldsymbol{r}_1 - \boldsymbol{r}| \leq a_{12} + a.$$

The above guarantees that the two spheres $\mathcal{B}(\boldsymbol{r}; a)$ and $\mathcal{B}(\boldsymbol{r}_1; a_{12})$ will intersect. Let $\mathcal{V}$ be this region of intersection, then the region of integration of $\boldsymbol{r}_2$ becomes $\mathcal{B}(\boldsymbol{r}; a) \setminus \mathcal{B}(\boldsymbol{r}_1; a_{12}) = \mathcal{B}(\boldsymbol{r}; a) \setminus \mathcal{V}$. This is useful as $\mathcal{V}$ is formed of two spherical caps whose volume is easy to calculate [§].

Using the split of these two regions for $\boldsymbol{r}_1$ we obtain:

$$\begin{aligned} J(J-1)\langle u^1_{\text{sc}}(\boldsymbol{r})\chi_{\mathcal{P}_2}(\boldsymbol{r})\rangle &= \mathfrak{n}^2 \int_{\mathcal{R}_1 \setminus \mathcal{B}(\boldsymbol{r}; a_{12}+a)} \langle u^1_{\text{sc}}(\boldsymbol{r})\rangle(\boldsymbol{r}_1) \int_{\mathcal{B}(\boldsymbol{r}; a)} \mathrm{d}\boldsymbol{r}_2 \mathrm{d}\boldsymbol{r}_1 \\ &\quad + \mathfrak{n}^2 \int_{\mathcal{B}(\boldsymbol{r}; a_{12}+a) \setminus \mathcal{B}(\boldsymbol{r}; a_{12}-a)} \langle u^1_{\text{sc}}(\boldsymbol{r})\rangle(\boldsymbol{r}_1) \left[\frac{4}{3}\pi a^3 - V_{\text{cap}}(|\boldsymbol{r} - \boldsymbol{r}_1|)\right] \mathrm{d}\boldsymbol{r}_1 \\ &= \phi\mathfrak{n} \int_{\mathcal{R}_1 \setminus \mathcal{B}(\boldsymbol{r}; a_{12}-a)} \langle u^1_{\text{sc}}(\boldsymbol{r})\rangle(\boldsymbol{r}_1) \mathrm{d}\boldsymbol{r}_1 \\ &\quad - \mathfrak{n}^2 \int_{\mathcal{B}(\boldsymbol{r}; a_{12}+a) \setminus \mathcal{B}(\boldsymbol{r}; a_{12}-a)} \langle u^1_{\text{sc}}(\boldsymbol{r})\rangle(\boldsymbol{r}_1) V_{\text{cap}}(|\boldsymbol{r} - \boldsymbol{r}_1|) \mathrm{d}\boldsymbol{r}_1. \end{aligned} \tag{2.75}$$

where $V_{\text{cap}}(d)$ is the volume of $\mathcal{V}$ and $d = |\boldsymbol{r} - \boldsymbol{r}_1|$. By using the formulas for spherical

[§]For details, see the website: https://mathworld.wolfram.com/Sphere-SphereIntersection.html.

caps [§] we can calculate that:

$$V_{\text{cap}}(d) = \frac{\pi}{12d}(a + a_{12} - d)^2(d^2 + 2(a + a_{12})d - 3(a - a_{12})^2).$$

B.4 An isotropic pair-correlation

In Appendix B.3 we chose a simple pair-correlation to simplify the integral (2.73). Here we show how to reduce this integral when assuming a more general form for the isotropic pair-correlation given by (2.11).

In the pair-correlation (2.11) we assume there is a value b_{12} for which $\mathrm{g}(r) = 1$ when $r \geq b_{12}$. This is an approximation, but it is essential for the results discussed here. The distance b_{12}, which is also called the correlation length, dictates at what distance inside the material the incident wave will be extinct.

Following closely the steps that led to (2.75), we now split the integral over $\boldsymbol{r}_1$ into two regions $\mathcal{R}_1 \setminus \mathcal{B}(\boldsymbol{r}; b_{12} + a)$ and $\mathcal{B}(\boldsymbol{r}; b_{12} + a) \setminus \mathcal{B}(\boldsymbol{r}; a_{12} - a)$, which leads to:

$$\begin{aligned} J(J-1)\langle u^1_{\text{sc}}(\boldsymbol{r})\chi_{\mathcal{P}_2}(\boldsymbol{r})\rangle = \mathfrak{n}^2 \int_{\mathcal{R}_1 \setminus \mathcal{B}(\boldsymbol{r}; b_{12}+a)} \langle u^1_{\text{sc}}(\boldsymbol{r})\rangle(\boldsymbol{r}_1) \int_{\mathcal{B}(\boldsymbol{r}; a)} \mathrm{d}\boldsymbol{r}_2 \mathrm{d}\boldsymbol{r}_1 \\ + \mathfrak{n}^2 \int_{\mathcal{B}(\boldsymbol{r}; b_{12}+a) \setminus \mathcal{B}(\boldsymbol{r}; a_{12}-a)} \langle u^1_{\text{sc}}(\boldsymbol{r})\rangle(\boldsymbol{r}_1) \int_{\mathcal{B}(\boldsymbol{r}; a)} \mathrm{g}(|\boldsymbol{r}_1 - \boldsymbol{r}_2|) \mathrm{d}\boldsymbol{r}_2 \mathrm{d}\boldsymbol{r}_1, \end{aligned} \quad (2.76)$$

where we use (2.35) to guarantee that the ball $\mathcal{B}(\boldsymbol{r}; b_{12} + a)$ is completely contained within the region $\mathcal{R}_1$. Without the condition (2.35) it does not seem possible to show that the incident wave becomes extinct, so we hypothesise that this is a necessary condition, as well as sufficient.

The integral on the right of the first line of (2.76) was already resolved in the previous section, except now we replace a_{12} with b_{12}. For the integrals on the second line of (2.76), we use the change of variables from $\boldsymbol{r}_2$ to $\boldsymbol{r}_{21} = \boldsymbol{r}_2 - \boldsymbol{r}_1$ and $\boldsymbol{r}_1$ to $\boldsymbol{x}_1 = \boldsymbol{r} - \boldsymbol{r}_1$ to obtain:

$$\begin{aligned} J(J-1)\langle u^1_{\text{sc}}(\boldsymbol{r})\chi_{\mathcal{P}_2}(\boldsymbol{r})\rangle = \mathfrak{n}\phi \int_{\mathcal{R}_1 \setminus \mathcal{B}(\boldsymbol{r}; b_{12}+a)} \langle u^1_{\text{sc}}(\boldsymbol{r})\rangle(\boldsymbol{r}_1) \mathrm{d}\boldsymbol{r}_1 \\ + \mathfrak{n}^2 \int_{\mathcal{B}(\mathbf{0}; b_{12}+a) \setminus \mathcal{B}(\mathbf{0}; a_{12}-a)} \langle u^1_{\text{sc}}(\boldsymbol{r})\rangle(\boldsymbol{r} - \boldsymbol{x}_1) G(\boldsymbol{x}_1) \mathrm{d}\boldsymbol{x}_1, \end{aligned} \quad (2.77)$$

where

$$G(\boldsymbol{x}_1) = \int_{\mathcal{B}(\boldsymbol{x}_1; a)} \mathrm{g}(r_{21}) \mathrm{d}\boldsymbol{r}_{21}. \quad (2.78)$$

and $r_{21} = |\boldsymbol{r}_{21}|$. This concludes the calculations in this section.

References

[1] Springer London, 2008. URL: http://dx.doi.org/10.1007/978-1-84800-119-0.

[2] *Acoustic Metamaterials: Negative Refraction, Imaging, Lensing and Cloaking*. Springer Netherlands, 2013. URL: http://dx.doi.org/10.1007/978-94-007-4813-2.

[3] M. Adda-Bedia et al. 'Solution of the Percus-Yevick equation for hard disks'. In: *The Journal of Chemical Physics* 128.18 (May 2008). URL: http://dx.doi.org/10.1063/1.2919123.

[4] Vincent C. Ballenegger et al. 'The Ewald-Oseen extinction theorem and extinction lengths'. In: *American Journal of Physics* 67.7 (July 1999), pp. 599–605. URL: https://doi.org/10.1119/1.19330.

[5] Max Born et al. *Principles of Optics: 60th Anniversary Edition*. Cambridge University Press, Dec. 2019. URL: http://dx.doi.org/10.1017/9781108769914.

[6] V.V. Bringi et al. 'The effects on pair correlation function of coherent wave attenuation in discrete random media'. In: *IEEE Transactions on Antennas and Propagation* 30.4 (July 1982), pp. 805–808. URL: https://doi.org/10.1109/tap.1982.1142852.

[7] Rémi Carminati et al. *Principles of Scattering and Transport of Light*. Cambridge University Press, June 2021. URL: https://doi.org/10.1017/9781316544693.

[8] Mathieu Chekroun et al. 'Comparison between a multiple scattering method and direct numerical simulations for elastic wave propagation in concrete'. In: *Ultrasonic wave propagation in non homogeneous media*. Springer, 2009, pp. 317–327. URL: http://link.springer.com/chapter/10.1007/978-3-540-89105-5_28 (visited on 04/09/2016).

[9] Mathieu Chekroun et al. 'Time-domain numerical simulations of multiple scattering to extract elastic effective wavenumbers'. In: *Waves in Random and Complex Media* 22.3 (Aug. 2012), 398–422. URL: http://dx.doi.org/10.1080/17455030.2012.704432.

[10] J Dubois et al. 'Coherent acoustic response of a screen containing a random distribution of scatterers: Comparison between different approaches'. In: *Journal of Physics: Conference Series* 269 (Jan. 2011), p. 012004. URL: https://doi.org/10.1088/1742-6596/269/1/012004.

[11] Heidi Fearn et al. 'Microscopic approach to reflection, transmission, and the Ewald–Oseen extinction theorem'. In: *American Journal of Physics* 64.8 (Aug. 1996), pp. 986–995. URL: https://doi.org/10.1119/1.18315.

[12] Artur L. Gower. 'Acoustic multiple scattering'. In: (2021). URL: https://github.com/JuliaWaveScattering/MultipleScattering.jl/blob/master/docs/src/maths/acoustics.pdf.

[13] Artur L. Gower. 'Multiple scattering of waves'. In: (2022). URL: https://github.com/JuliaWaveScattering/MultipleScattering.jl/blob/master/docs/src/maths/multiplescattering.pdf.

[14] Artur L. Gower et al. 'A proof that multiple waves propagate in ensemble-averaged particulate materials'. In: *Proceedings of the Royal Society A: Mathematical, Physical and Engineering Sciences* 475.2229 (Sept. 2019), p. 20190344. URL: http://dx.doi.org/10.1098/rspa.2019.0344.

[15] Artur L Gower et al. 'Effective waves for random three-dimensional particulate materials'. In: *New Journal of Physics* 23.6 (June 2021), p. 063083. URL: http://dx.doi.org/10.1088/1367-2630/abdfee.

[16] Artur L. Gower et al. 'Multiple Waves Propagate in Random Particulate Materials'. In: *SIAM Journal on Applied Mathematics* 79.6 (Jan. 2019), 2569–2592. URL: http://dx.doi.org/10.1137/18M122306X.

[17] Artur L Gower et al. 'MultipleScatering.jl: A Julia library for simulating, processing, and plotting multiple scattering of waves.' In: *github.com/JuliaWaveScattering/MultipleScattering.jl* (2020).

[18] Artur L. Gower et al. 'Reflection from a multi-species material and its transmitted effective wavenumber'. en. In: *Proc. R. Soc. A* 474.2212 (Apr. 2018), p. 20170864. URL: http://rspa.royalsocietypublishing.org/content/474/2212/20170864 (visited on 22/04/2018).

[19] Artur Lewis Gower. 'EffectiveWaves.jl: A Julia package to calculate ensemble averaged waves in heterogeneous materials'. Version 0.3.4. In: *github.com/JuliaWaveScattering/EffectiveWaves.jl* (Dec. 2018).

[20] Akira Ishimaru. *Wave propagation and scattering in random media: Single scattering and transport theory v. 1*. San Diego, CA: Academic Press, Feb. 1978.

[21] Jari P. Kaipio et al. *Statistical and Computational Inverse Problems*. Springer New York, 2005. URL: http://dx.doi.org/10.1007/b138659.

[22] Gerhard Kristensson. 'Coherent scattering by a collection of randomly located obstacles – An alternative integral equation formulation'. In: *Journal of Quantitative Spectroscopy and Radiative Transfer* 164 (2015), pp. 97–108. URL: https://www.sciencedirect.com/science/article/pii/S0022407315002046.

[23] Gerhard Kristensson. *Scattering of Electromagnetic Waves by Obstacles*. Mario Boella Series on Electromagnetism in Information and Communication. Edison, NJ, USA: SciTech Publishing, 2016. URL: http://digital-library.theiet.org/content/books/ew/sbew524e.

[24] Gerhard Kristensson et al. *Multiple scattering by a collection of randomly located obstacles Part IV: The effect of the pair correlation function*. English. Vol. TEAT-7272. Technical Report LUTEDX/(TEAT-7272)/1-23/(2021). 2021. URL: https://portal.research.lu.se/en/publications/multiple-scattering-by-a-collection-of-randomly-located-obstacles-8.

[25] Melvin Lax. 'Multiple Scattering of Waves. II. The Effective Field in Dense Systems'. In: *Physical Review* 85.4 (Feb. 1952), pp. 621–629. URL: https://doi.org/10.1103/physrev.85.621.

[26] C. M. Linton et al. 'Multiple Scattering by Multiple Spheres: A New Proof of the Lloyd–Berry Formula for the Effective Wavenumber'. en. In: *SIAM J. Appl. Math.* 66.5 (Jan. 2006), pp. 1649–1668. URL: http://epubs.siam.org/doi/abs/10.1137/050636401 (visited on 14/09/2016).

[27] C. M. Linton et al. 'Multiple scattering by random configurations of circular cylinders: Second-order corrections for the effective wavenumber'. en. In: *J. Acoust. Soc. Am.* 117.6 (2005), p. 3413. URL: http://scitation.aip.org/content/asa/journal/jasa/117/6/10.1121/1.1904270 (visited on 04/09/2016).

[28] Guancong Ma et al. 'Acoustic metamaterials: From local resonances to broad horizons'. In: *Science Advances* 2.2 (Feb. 2016). URL: https://doi.org/10.1126/sciadv.1501595.

[29] Y. Ma et al. 'Multiple scattering theory for wave propagation in discrete random media'. In: *International Journal of Engineering Science* 22.8-10 (Jan. 1984), pp. 1139–1148. URL: https://doi.org/10.1016/0020-7225(84)90115-0.

[30] P. A. Martin. 'Multiple scattering by random configurations of circular cylinders: Reflection, transmission, and effective interface conditions'. In: *The Journal of the Acoustical Society of America* 129.4 (Apr. 2011), 1685–1695. URL: http://dx.doi.org/10.1121/1.3546098.

[31] P. A. Martin. *Multiple Scattering: Interaction of Time-Harmonic Waves with N Obstacles*. Cambridge University Press, Aug. 2006. URL: http://dx.doi.org/10.1017/CBO9780511735110.

[32] P.A. Martin. 'On connections between boundary integral equations and T-matrix methods'. In: *Engineering Analysis with Boundary Elements* 27.7 (July 2003), pp. 771–777. URL: https://doi.org/10.1016/s0955-7997(03)00028-6.

[33] Michael I. Mishchenko. *Electromagnetic Scattering by Particles and Particle Groups: An Introduction*. Cambridge University Press, Apr. 2014. URL: http://dx.doi.org/10.1017/CBO9781139019064.

[34] Michael I. Mishchenko et al. *Multiple Scattering of Light by Particles: Radiative Transfer and Coherent Backscattering*. Cambridge University Press, 2006. 518 pp.

[35] Patrick Kofod Mogensen et al. 'Optim: A mathematical optimization package for Julia'. In: *Journal of Open Source Software* 3.24 (2018), p. 615.

[36] K. Muinonen et al. 'Coherent backscattering verified numerically for a finite volume of spherical particles'. In: *The Astrophysical Journal* 760.2 (Nov. 2012), p. 118. URL: https://doi.org/10.1088/0004-637x/760/2/118.

[37] V. Romero-García et al. 'Wave transport in 1D stealthy hyperuniform phononic materials made of non-resonant and resonant scatterers'. In: *APL Materials* 9.10 (Oct. 2021). URL: http://dx.doi.org/10.1063/5.0059928.

[38] Alverède Simon et al. 'Propagation of coherent shear waves in scattering elastic media'. In: *Physical Review E* 103.5 (May 2021). URL: https://doi.org/10.1103/physreve.103.l051001.

[39] Steven W Smith. *The scientist and engineer's guide to digital signal processing*. en. 1999.

[40] Victor P. Tishkovets et al. 'Scattering of electromagnetic waves by ensembles of particles and discrete random media'. In: *Journal of Quantitative Spectroscopy and Radiative Transfer* 112.13 (Sept. 2011), pp. 2095–2127. URL: https://doi.org/10.1016/j.jqsrt.2011.04.010.

[41] S. Torquato et al. 'Ensemble Theory for Stealthy Hyperuniform Disordered Ground States'. In: *Phys. Rev. X* 5 (2 May 2015), p. 021020. URL: https://link.aps.org/doi/10.1103/PhysRevX.5.021020.

[42] S Torquato et al. 'Random Heterogeneous Materials: Microstructure and Macroscopic Properties'. In: *Applied Mechanics Reviews* 55.4 (July 2002), B62–B63. URL: https://doi.org/10.1115/1.1483342.

[43] Salvatore Torquato. 'Hyperuniform states of matter'. In: *Physics Reports* 745 (June 2018), pp. 1–95. URL: https://doi.org/10.1016/j.physrep.2018.03.001.

[44] L. Tsang et al. 'Multiple scattering of acoustic waves by random distribution of discrete spherical scatterers with the quasicrystalline and Percus–Yevick approximation'. In: *The Journal of the Acoustical Society of America* 71.3 (Mar. 1982), 552–558. URL: http://dx.doi.org/10.1121/1.387524.

[45] Leung Tsang et al. *Scattering of Electromagnetic Waves: Numerical Simulations*. Wiley, May 2001. URL: http://dx.doi.org/10.1002/0471224308.

[46] Leung Tsang et al. *Scattering of Electromagnetic Waves: Theories and Applications*. Wiley, July 2000. URL: http://dx.doi.org/10.1002/0471224286.

[47] B J Uscinski. *Elements of wave propagation in random media*. en. New York, NY: McGraw-Hill, Nov. 1977.

[48] V. K. Varadan et al. 'Multiple scattering theory for waves in discrete random media and comparison with experiments'. In: *Radio Science* 18.3 (May 1983), pp. 321–327. URL: https://doi.org/10.1029/rs018i003p00321.

[49] Kevin Vynck et al. 'Light in correlated disordered media'. In: *Reviews of Modern Physics* 95.4 (Nov. 2023). URL: http://dx.doi.org/10.1103/RevModPhys.95.045003.

[50] J. R. Willis. 'Transmission and reflection at the boundary of a random two-component composite'. In: *Proc. R. Soc. A* 476.2235 (Mar. 2020), p. 20190811. URL: https://doi.org/10.1098/rspa.2019.0811.

[51] J. R. Willis. 'Transmission and reflection of energy at the boundary of a random two-component composite'. In: *Proceedings of the Royal Society A: Mathematical, Physical and Engineering Sciences* 479.2271 (Mar. 2023). URL: http://dx.doi.org/10.1098/rspa.2022.0730.

[52] J.R. Willis. 'Some personal reflections on acoustic metamaterials'. In: *Wave Motion* 108 (Jan. 2022). URL: http://dx.doi.org/10.1016/j.wavemoti.2021.102834.

[53] L. M. Zurk et al. 'Monte Carlo simulations of the extinction rate of densely packed spheres with clustered and nonclustered geometries'. In: *Journal of the Optical Society of America A* 12.8 (Aug. 1995), p. 1772. URL: https://doi.org/10.1364/josaa.12.001772.

Chapter 3

From wave propagation to particle correlations in random particulate materials

ARISTEIDIS KARNEZIS

Abstract

In this chapter, Section 3.1 shows how including more than one effective wavenumber can significantly change reflection coefficients. This aspect is crucial, considering that many measurement techniques rely on the reflection coefficients. In Section 3.2 we delve into the mathematical and computational aspect of determining multiple effective wavenumbers in three dimensions, by solving an implicit determinant equation. Recognising a gap in the existing literature, we have developed an asymptotic method to locate these complex effective wavenumbers, particularly in the context of monopole scatterers. Something which was previously missing in the literature. Section 3.3 addresses challenges that arose when performing Monte-Carlo simulations, where each simulation places one configuration of particles in a finite region. The key finding is that confining particles in a finite region can affect their pair-correlation and even their volume fraction. We demonstrate these effects and show how to avoid them with what we call the *Cookie-cutter* method. The sections are distinct yet collectively enrich our findings.

3.1 Comparing the Reflection Coefficients

In this section, we explore the significance of reflection coefficients in various measurement techniques [4, 15]. The emphasis is on contrasting the coefficients derived from different methods to understand the average behaviour of waves in various scenarios. In other words, rather than comparing the resulting fields of average waves, we can compare their resulting reflection coefficients [6, 10, 14, 17, 18, 23, 24].

In our analysis depicted in Figure 3.1, we examine how reflection coefficients vary with changes in volume fraction (ϕ) for both sound-soft and sound-hard particles (particle properties are detailed in Table 2.1). We keep the particle radius fixed at $a = 1.2$ and vary the non-dimensional frequency over the range $0.24 \leq ka \leq 2.16$.

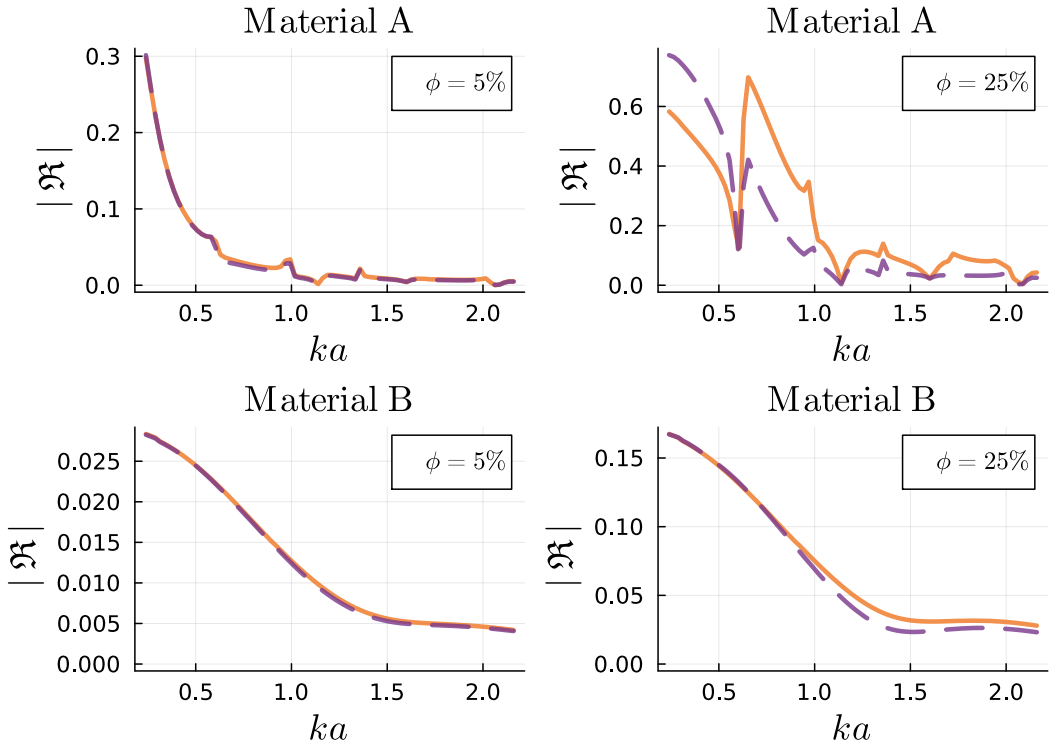

Figure 3.1: Material A contains sound-soft particles with density $\rho_0 = 0.30\ kg \cdot m^{-3}$ and wavespeed $c_0 = 0.30\ m \cdot s^{-1}$. Material B on the other hand considers sound-hard particles with density $\rho_0 = 10.0\ kg \cdot m^{-3}$ and wavespeed $c_0 = 10.0\ m \cdot s^{-1}$. The density and wavespeed of the host material is $\rho = 1.0\ kg \cdot m^{-3}$ and $c = 1.0\ m \cdot s^{-1}$ respectively. The orange solid line represents the reflection coefficients generated using the *Dominant-wavenumber* of the average transmitted wave with respect to the non-dimensional ka. The purple dashed line takes into account all the effective waves (*All-wavenumbers* method) of the average transmitted wave.

Two distinct methods, the *Dominant-wavenumber* and the *All-wavenumbers* methods, are employed to calculate the reflection coefficients, offering insights into their variations across different scenarios [7, 10]. The Dominant-wavenumber method

uses one effective wavenumber k_1, that is equation (2.12) for $p = 1$. Conversely, the All-wavenumbers approach includes multiple wavenumbers and numerically tries to discretise the space to create a mesh. For more details on the All-wavenumbers method, see [7, Section 5]. It is important to take this factor into consideration since the mesh will try to match the discrete solution with a sum of these effective waves. At the same time, it is necessary not to push the matched layer towards the boundaries, because the closer to the boundaries, the more effective waves there are. Then we can calculate the reflection coefficients.

Both methods are applicable for all types of scatterers. For sound-hard particles, it is clear that the Dominant-wavenumber overlaps with the All-wavenumbers method, while for sound-soft particles the two methods do not match. For instance, consider the two scenarios depicted in the top left and bottom left plots of Figure 3.1. In both scenarios, a single effective wavenumber - the dominant wavenumber - can be extracted, giving matching results. Yet, when we increase the volume fraction to 25%, as shown in the top right and bottom right plots of Figure 3.1, we were able to detect multiple wavenumbers. In these scenarios, the results do not overlap, meaning that the existence of more than one wavenumber leads to changes in the reflection coefficients.

3.2 Asymptotic Location of Effective Wavenumbers in 3D

The focus in this section shifts to a three-dimensional perspective on the effective wavenumbers k_p. This expansion builds upon the foundational work of Gower *et al.*, who analytically derived these wavenumbers for two-dimensional scenarios in [5, Section 5]. This study not only assumes large values for $|k_p|$, with an increasing trend as p grows, but also presupposes a positive imaginary part, $\mathrm{Im} k_p > 0$. Such assumptions are critical for satisfying a dispersion equation that relates each wavenumber k_p with a frequency, paving the way for a deeper understanding of how waves propagate through different media. The dispersion equation for effective plane-waves [6, Equation (5.15)] takes the matrix form:

$$M_{nn'}(k_p) = \delta_{nn'} + \sum_{\ell} \frac{\sqrt{4\pi} c_{n'n(\ell,0)}}{k_p^2 - k^2} \mathrm{i}^{-\ell} \sqrt{2\ell + 1} T_n \bar{\mathfrak{n}} a_{12} \mathcal{N}_\ell = 0, \tag{3.1}$$

where a_{12} is the minimum allowed distance between particle centres, T_n are the coefficients for the particle's T-matrix defined in [6, Equation 2.8], $c_{n'n(\ell,0)}$ are the Clebsch-Gordan coefficients with l being non-negative integers ([6, equation B.5]),

$\bar{\mathfrak{n}} = \mathfrak{n}\dfrac{J-1}{J}$ where $\mathfrak{n}$ is the number density of particles defined as $\mathfrak{n} = \dfrac{3\phi}{4\pi a_{12}^3}$, and:

$$\mathcal{N}_\ell = ka_{12}\mathrm{h}_\ell^{(1)'}(ka_{12})\mathrm{j}_\ell(k_p a_{12}) - k_p a_{12}\mathrm{h}_\ell^{(1)}(ka_{12})\mathrm{j}_\ell'(k_p a_{12}), \tag{3.2}$$

which is a coupling term relating to the scattered field at one particle expressed in coordinates centred at another particle. An integral part of this work involves approximating the formulas established in (3.2) using the asymptotic properties of spherical Bessel and Hankel functions of the first kind. Since we are only interested in monopole scatterers that scatter waves uniformly in all directions, it is easy to make this approximation. The simplest case for monopole scatterers is when $\ell = m = n = 0$, meaning that we are only keen for the zeroth order. Thus, the zeroth spherical Bessel function $\mathrm{j}_0(k_p)$ and spherical Hankel function $\mathrm{h}_0(k_p)$ for large $|k_p|$ can be written respectively as follows [2, Section 11.7]:

$$\mathrm{j}_0(k_p) = \frac{\sin k_p}{k_p} \qquad \text{and} \qquad \mathrm{h}_0^{(1)}(k_p) = -i\frac{e^{ik_p}}{k_p}. \tag{3.3}$$

Solving the dispersion equation (3.1) and the determinant of the $M_{nn'}(k_p)$ matrix, we can extract the effective wavenumbers k_p [13]. Thus, the k_p must satisfy:

$$\det(M_{(\ell,0),(\ell',0)}(k_p)) = 0. \tag{3.4}$$

For monopole scatterers, (3.1) takes the form:

$$a_{12}^2(k_p^2 - k^2)\det M = (k_p a_{12})^2 - (ka_{12})^2 + 4\pi\mathfrak{n}a_{12}^3 T_0\mathcal{N}_0 \sim k_p^2 - \mathrm{c}e^{-ik_p a_{12}}, \tag{3.5}$$

where

$$\mathrm{c} = 2\pi\mathfrak{n}a_{12}^2 T_0\mathrm{h}_0^{(1)}(ka_{12}). \tag{3.6}$$

To confirm the presence of these wavenumbers, and determine their behaviour as $|p| \to \infty$, we make use of (3.2) and (3.3) and ignore all terms that are algebraically smaller than k, or similarly we investigate the regime where $k_p \gg k$. Keep in mind that we need to apply this approximation throughout the computations to obtain (3.5). We also note that the effective wavenumbers k_p are independent of the angle of incidence θ_{inc} [12], even though there are effective wavenumbers that are not excited for specific angles of incidence [5, 7].

To find the locations of the effective wavenumbers we substitute:

$$k_p = x + i \log y, \tag{3.7}$$

where x and y are real, and $|x|$ and y are large with $y > 1$. That gives:

$$x^2 - \mathrm{c}e^{-ix}y = 0. \tag{3.8}$$

For the logarithm, we apply the standard branch cut along the interval $(-\infty, 0)$ and consider positive function values for positive arguments. We are interested only in the leading order, so, $x^2 \sim y$, which reduces (3.8) to:

$$x^2 \sim r_c \mathrm{e}^{i(\theta_c - x)}\, y, \qquad \text{or similarly} \qquad x^2 \sim r_c \Big[\cos(\theta_c - x) + i\, \sin(\theta_c - x)\Big]\, y, \tag{3.9}$$

where we substituted $\mathrm{c} = r_c e^{i\theta_c}$, for real scalars r_c and θ_c. Next, we take the real and imaginary parts of (3.9) to be equal and discard the negative solution because of the quadratic nature of x. This leads to:

$$x \sim \theta_c + 2\pi p \qquad \text{and} \qquad y \sim \frac{1}{r_c}(\theta_c + 2\pi p)^2 \qquad \forall p \in \mathbb{Z}. \tag{3.10}$$

Thus, for the case of monopole scatterers, the effective wavenumbers k_p at the leading order take the form:

$$k_p = \sigma_p + i\, \log\left(\frac{\sigma_p^2}{r_c}\right), \tag{3.11}$$

where

$$\begin{cases} \sigma_p = \theta_c + 2\pi p, & \forall \theta_c \in \left[\dfrac{-\pi}{2}, \dfrac{\pi}{2}\right], \qquad \forall p \in \mathbb{Z}, & \text{(3.12a)} \\ r_c e^{i\theta_c} = 2\pi \mathfrak{n} a_{12}^2 T_0 \mathrm{h}_0^{(1)}(k a_{12}), & r_c > 0. & \text{(3.12b)} \end{cases}$$

The real part indicates how rapidly the wave oscillates in space, while the imaginary part represents how the wave attenuates. The growth of the wavenumber is not linear but has a slower, logarithmic scale of increase which can model situations (attenuation) where the decay rate changes more gradually at larger scales.

3.2.1 Numerical results of the theoretical predictions

The next step involves comparing the analytical expression of the effective wavenumbers with numerical results generated using [11]. To be more specific, we consider

spherical particles with penetrable boundary conditions, and the following parameters:

Table 3.1: Parameter Values

Parameter	Value
Volume fraction (ϕ)	30%
Particle radius (a_0)	0.867
Non-dimensional exclusion distance (ξ)	$2a_0$
Non-dimensional particle radius (ka_0)	0.7516
Non-dimensional inter-particle distance (ka_{12})	1.510
Ratio of solid to void particle properties (sound-soft)	0.30
Ratio of solid to void particle properties (sound-hard)	5.0

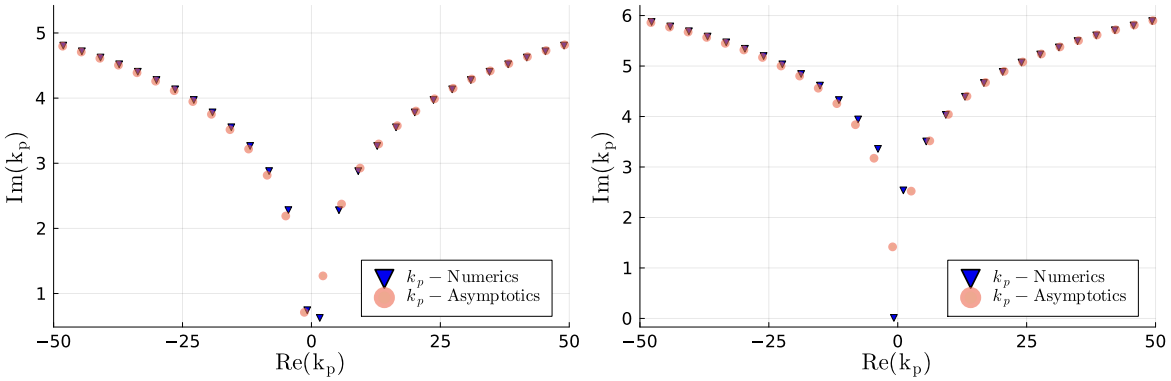

(a) sound-soft particles (b) sound-hard particles

Figure 3.2: Comparison between the analytical formula (3.11) predicting an infinite series of complex effective wavenumbers and the numerical solutions for these effective wavenumbers deduced from the dispersion equation using the *EffectiveWaves.jl* library [11]. The parameters used are given by Table 3.1. The analytic formula generally demonstrates a high level of accuracy, with the exception of the two smallest attenuating wavenumbers.

As shown in Figure 3.2, the effective wavenumbers for sound-soft and sound-hard particles derived asymptotically from (3.11) closely agree with the numerically calculated wavenumbers even when integer p becomes large. However, we cannot help but notice that the wavenumbers with the most contribution to the total average wave are not in agreement. Since these wavenumbers have a small imaginary part (high attenuation), they cannot be analytically calculated, even though they are important to accurately calculate the transmission.

3.3 Enhancing precision in Monte-Carlo simulations

This section acts as a crucial bridge between Chapter 2 and Chapter 4. Here, we address the numerical challenges that arose when performing Monte-Carlo simulations, with a specific focus on the pair-correlation function. We define two key regions,

namely $\mathcal{R}_R$ containing all particles and $\mathcal{R}_{R-a}$ centred on particle centres, and introduce fundamental measures like particle number density ($\mathfrak{n}$) and particle volume fraction (ϕ) to describe particle distributions. However, when using these measures for finite regions, they do not match because of the region's boundaries. In light of this limitation, we have come up with innovative methods to better measure these factors. In Section 3.3.2, we explore two particle placement methods in Monte-Carlo simulations: the Bounded-sphere method and the Cookie-cutter method, with the latter offering better approximation to infinite medium conditions.

However, we encounter a discrepancy when applying the Percus-Yevick (PY) method to characterise pair-correlations, as it fails to match results from the Cookie-cutter method at the same number density. Instead, we find that a reduced number density ($\mathfrak{n}_{PY}$) is required to align Percus-Yevick with the pair-correlation results observed in the Cookie-cutter method. This finding underscores the importance of fitting Monte-Carlo experiments with theoretical models like the Percus Yevick. To do this effectively, it is crucial to connect these results with the formulas introduced in Chapter 4. These techniques, particularly those related to the efficient calculation of pair-correlations from small particle configurations and the recovery of particle configurations from pair-correlations, are foundational to the theoretical and numerical approaches discussed in Chapter 2.

3.3.1 A numerical pair-correlation

In this section we let:

$$\mathcal{R}_R \quad \text{be a sphere that contains all the particles} \tag{3.13}$$

$$\mathcal{R}_{R-a} \quad \text{be a sphere that contains the centre all the particles} \tag{3.14}$$

where a is the particle radius. The region $\mathcal{R}_R$ is the green circle in Figure 3.3, whereas $\mathcal{R}_{R-a}$ is the dashed circle. Let $\mathfrak{p}$ be a particle. We will consider only one type of particle for simplicity.

To specify the density of particles, we use the term *particle number density* $\mathfrak{n}$ to mean the average number of particles per volume, and *particle volume fraction* ϕ to mean the average volume occupied by the particles divided by the volume of the region containing those particles.

Typically the number density $\mathfrak{n}_\infty$ and volume fraction ϕ_∞ are used interchangeably through the formula:

$$\phi_\infty = |\mathfrak{p}|\mathfrak{n}_\infty, \tag{3.15}$$

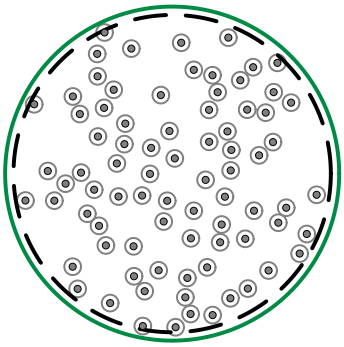

Figure 3.3: The region within the green circle is $\mathcal{R}_R$ and has a radius $R = 20$ with each particle having a 20% volume fraction and a radius of $a = 1$. The region within the dashed circle is $\mathcal{R}_{R-a}$ and all particle centres are within this region.

where $|\mathfrak{p}|$ is the volume of the particle $\mathfrak{p}$. However, this is only exact for an infinite sized region, and so will not be used here. One clear reason why (3.15) does not hold for a finite region is that the region containing the particle centres $\mathcal{R}_{R-a}$ is different from the volume containing the particles $\mathcal{R}_R$.

To aid this discussion, for a finite region, we define:

$$N_R := \text{the number of particles completely contained within } \mathcal{R}_R, \tag{3.16}$$

$$\mathfrak{n}_R := \frac{N_R}{|\mathcal{R}_{R-a}|} \quad \text{the true number density}, \tag{3.17}$$

$$\phi_R := \frac{N_R|\mathfrak{p}|}{|\mathcal{R}_R|} \quad \text{the particle volume fraction in } \mathcal{R}_R, \tag{3.18}$$

$$\phi_\infty := \frac{\text{total volume of intersection of particles with } \mathcal{R}_{R-a}}{|\mathcal{R}_{R-a}|}. \tag{3.19}$$

Note that N_R is also equal to the number of particle centres within $\mathcal{R}_{R-a}$.

See Figure 3.3 for an illustration, noting that the centres of all particles are contained within $\mathcal{R}_{r-a}$. In the next paragraphs, we discuss how $\mathfrak{n}$ is the same as $\mathfrak{n}_\infty$, assuming particles are homogeneously distributed, while the volume fraction is more complicated.

To begin, note that within $\mathcal{R}_{R-a}$ some particles are cut by the border of $\mathcal{R}_{R-a}$. The definition of ϕ_∞ takes into account only the parts of particles within $\mathcal{R}_{R-a}$. Because of this, ϕ_R is less than ϕ_∞, whereas $|\mathfrak{p}|\mathfrak{n}_R$ is more than ϕ_∞. These differences can be significant for a finite region. In Figure 3.4, the radius of the region $\mathcal{R}_R$ is equal to

$R = 20$, and the radius of each particle equals to $a = 1$, in which case, for a 3D sphere:

$$\frac{|\mathcal{R}_R|}{|\mathcal{R}_{R-a}| - 1} = \frac{20^3}{19^3 - 1} \approx 0.166. \tag{3.20}$$

This implies that:

$$\frac{\mathfrak{n}_R|\mathfrak{p}|}{\phi_R - 1} \approx 0.166, \tag{3.21}$$

which is more than a 10% difference.

Instead, it is simpler to consider the number density of a finite region, which is also the variable considered in most theoretical methods of ensemble averaging. For example, let us convince you that $\mathfrak{n}_R = \mathfrak{n}_\infty$ by considering the following thought exercise. Assume the particles are equally likely to be in any position*. Now, pick a smaller region $\mathcal{R}_1 \subset \mathcal{R}_{R-a}$, and count the average number of particle centres N_1 (over many ensembles) within $\mathcal{R}_1$. Then, we figure out the number density in $\mathcal{R}_1$ by dividing N_1 by the size of $\mathcal{R}_1$, which we write as $\mathfrak{n}_1 = \dfrac{N_1}{|\mathcal{R}_1|}$. Because the particles are equally likely to be everywhere, we find that $\mathfrak{n}_1 = \mathfrak{n}_\infty$.

3.3.2 Monte-Carlo simulations

Now that we understand the particle number density in a finite region, we turn to how to generate a random uniformly distributed set of particles. Again, in a finite region, there are important subtleties.

We begin by describing two different methods to place particles within a region $\mathcal{R}$. First, a naive method called the *Bounded-sphere* method that describes the distributions of particles within a bounded sphere of radius R, then a method that does accurately approximate how particles would be distributed in an infinite region, the *Cookie-cutter* method.

Bounded sphere method. The particles of each configuration are generated one at a time, and rejected if they either do not fit within the region $\mathcal{R}_R$ (green circle) or overlap with any other particles. In this case, particles are more likely to be near the border, as shown in Figure 3.4 meaning that particles are not uniformly distributed. We then evaluate the probability density function for the generated particle configurations and calculate the average. We repeat this process to improve the accuracy of the integral estimate.

*This assumption is not true for the bounded-sphere method discussed in Section 3.3.2.

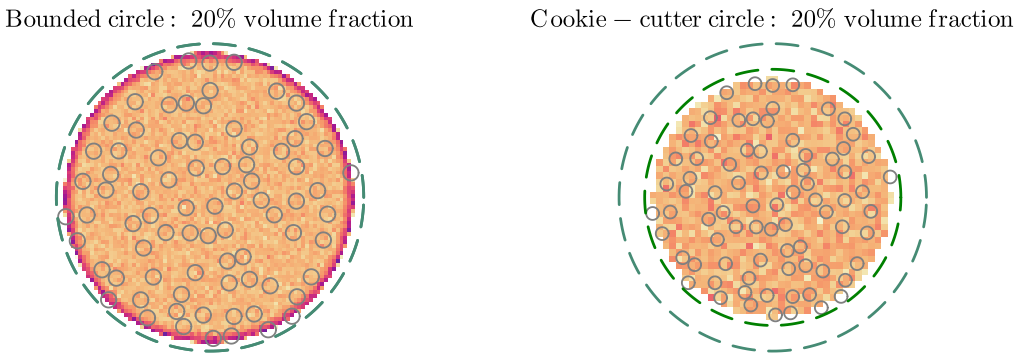

Figure 3.4: Both figures show the result of placing particles randomly within a region $\mathcal{R}$ with a radius of $R = 20$. Each particle has a volume fraction $\phi = 20\%$ and a radius of $a = 1$. The colour shows the average density of particles after 100,000 simulations, with darker being a larger particle density. Here the darkest colour indicates that particles are 40% more likely to appear than the very lightest colour. The circles illustrate just one configuration. The image on the left (right) used the Bounded-sphere (Cookie-cutter) method.

If the system has radial symmetry, meaning that the probability density function is the same at all angles for a given radial distance, then we can average over all angles to obtain the radial probability density function. In other words, for radial symmetry we have that $\mathrm{p}(\boldsymbol{r}) = \mathrm{p}(r)$, so that:

$$\mathrm{p}(r) = \frac{1}{4\pi} \int \mathrm{p}(\boldsymbol{r}) \sin\theta \, \mathrm{d}\theta \, \mathrm{d}\phi. \tag{3.22}$$

One way to approximate (3.22) is to represent $\mathrm{p}(r)$ in some polynomial series, such as:

$$\mathrm{p}(r) = \sum_{\ell} \frac{2\ell + 2}{2} p_\ell \mathrm{P}_\ell(\bar{r}), \tag{3.23}$$

where $\bar{r} = \dfrac{2r}{\bar{R} - 1}$, P_ℓ are the Legendre polynomials and p_ℓ are the coefficients of the Legendre polynomials. To calculate the coefficients p_ℓ we simply multiply (3.22) by $P_\ell(\bar{r})$, use (3.23), and integrate over $\mathrm{d}r$ to arrive at:

$$p_\ell = \frac{1}{4\pi} \int \int \mathrm{P}_\ell(\bar{r}) \frac{\mathrm{p}(\boldsymbol{r})}{r^2} r^2 \sin\theta \mathrm{d}\theta \mathrm{d}\phi \mathrm{d}\bar{r} = \frac{1}{2\pi\bar{R}} \int_{\mathcal{R}} \mathrm{P}_\ell(\bar{r}) \frac{\mathrm{p}(\boldsymbol{r})}{r^2} \mathrm{d}\boldsymbol{r}, \tag{3.24}$$

where $\mathcal{R}$ is the set of all possible particle centres, $\mathrm{d}\boldsymbol{r}$ is a volume element of the variable $\boldsymbol{r}$, and we used:

$$\int_{-1}^{1} \mathrm{P}_{\ell_1}(x) \mathrm{P}_{\ell_2}(x) \mathrm{d}x = \frac{2\delta_{\ell_1 \ell_2}}{2\ell_1 + 1},$$

for any ℓ_1 and ℓ_2.

The probability density function can also be expressed as follows:

$$\mathrm{p}(r) = \frac{1}{4\pi r^2}\int \mathrm{p}(\boldsymbol{r}) r^2 \sin\theta \mathrm{d}\theta \mathrm{d}\phi \approx \frac{1}{4\pi r^2}\sum_{|\boldsymbol{v}_i|=r} \mathrm{p}(\boldsymbol{v}_i)|V(\boldsymbol{v}_i)|$$
$$\approx \frac{1}{4\pi r^2 S}\sum_{s}^{S}\sum_{|\boldsymbol{v}_i|=r}\frac{\#(\mathcal{X}^s \cap V(\boldsymbol{v}_i))}{\#\mathcal{X}^s} = \frac{1}{4\pi r^2 S}\sum_{s}^{S}\frac{1}{\#\mathcal{X}^s}\#\left[\mathcal{X}^s \cap \cup_{|\boldsymbol{v}_i|=r} V(\boldsymbol{v}_i)\right]. \quad (3.25)$$

where $\boldsymbol{v}_i$ is the centre of the volume element $|V(\boldsymbol{v}_i)|$ and $\#\mathcal{X}$ is the number of elements in the set $\mathcal{X}$. An alternative approach to approximate (3.25) is to first substitute (4.1), discretise the integral, and create the histogram:

$$\mathrm{p}(v_i) \approx \frac{1}{4\pi}\frac{1}{v_i^2 dr_i}\sum_{|\boldsymbol{v}_j|=v_i}\mathrm{p}(\boldsymbol{v}_j)|V(\boldsymbol{v}_j)| = \frac{1}{4\pi S}\frac{1}{v_i^2 dr_i}\sum_{s}^{S}\sum_{|\boldsymbol{v}_j|=v_i}\frac{\#\left[\mathcal{X}^s \cap V(\boldsymbol{v}_j)\right]}{\#\mathcal{X}^s}, \quad (3.26)$$

where dr_i is the radial length of $V(\boldsymbol{v}_i)$. Note this approximation fails for $v_i = 0$, which we address in the next section. In terms of computational efficiency, as most volume elements will have no particles in each ensemble $\mathcal{X}^s$, it is more efficient to iterate over each $\boldsymbol{x} \in \mathcal{X}^s$.

Figure 3.5 shows how we fit the probability density $\mathrm{p}(r)$ to the data from our Monte-Carlo simulations by using equations (3.24) and (3.26). This figure is key in showing us that particles tend to gather closer to the boundaries of the region than we might expect. By comparing different estimation methods to model this boundary effect, we underscore the importance of accurately considering boundaries in our simulations.

Cookie-cutter method. The particles are generated one at a time within a large region $\mathcal{R}_{R_L}$ with radius $R_L > R$, and rejected if they either do not fit within $\mathcal{R}_{R_L}$ (larger green circle) or overlap with any other particles. To sample the particle distribution, we then cut out a smaller region, away from the boundaries, and consider only the particles within the smaller region. The cutouts are like cutting out cookie dough. This smaller cutout can be repeated many times, in different locations within $\mathcal{R}_{R_L}$, and then the average particle distribution can be calculated across these cutouts. In Figure 3.4, we just cut out one small circle $\mathcal{R}_R$ from $\mathcal{R}_{R_L}$. In this case the particle centres are equally likely to be anywhere in $\mathcal{R}_{R-a}$.

Producing particles that are homogeneously distributed means we can use these particle positions to numerically calculate pair-correlation functions which closely approximate an infinite medium. One final detail to account for, due to the finite geometry, is that the number density produced by this method is difficult to predict

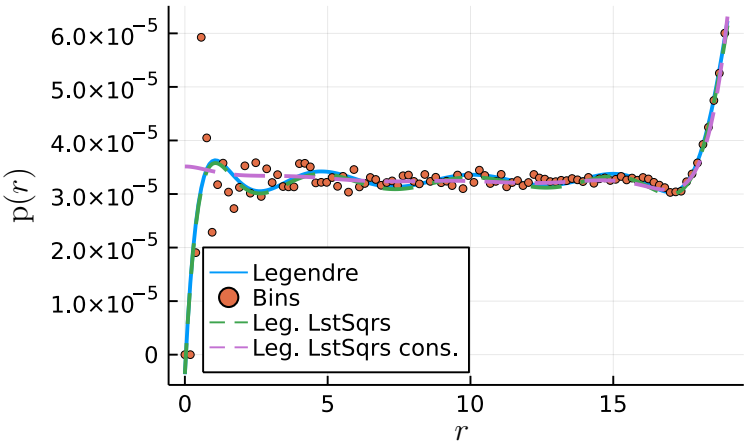

Figure 3.5: Shows our different estimations of $\mathrm{p}(r)$. Due to there being less particles near $r = 0$ we get a more noisy estimate. To explain the legend: *Legendre* used (3.24), *Bins* used (3.26), *Leg. LstSqrs* employs the same *Legendre method* but makes use of the Least Squares to calculate the p_ℓ, and *Leg. LstSqrs cons.* uses Least Squares but with the constraint $p'(0) = 0$.

from the onset. Say we aim to generate a set of particles with the number density $\mathfrak{n}_{R_L}$, so we need to place $N_R \approx \mathfrak{n}_{R_L}|\mathcal{R}_{R_L-a}|$ within $\mathcal{R}_{R_L}$. Doing this, the number $\mathfrak{n}_R$ will be slightly less than $\mathfrak{n}_{R_L}$. This is due to particles still being more likely to appear near the boundary of $\mathcal{R}_{R_L}$, and therefore reduce the number of particles within the region $\mathfrak{n}_R$.

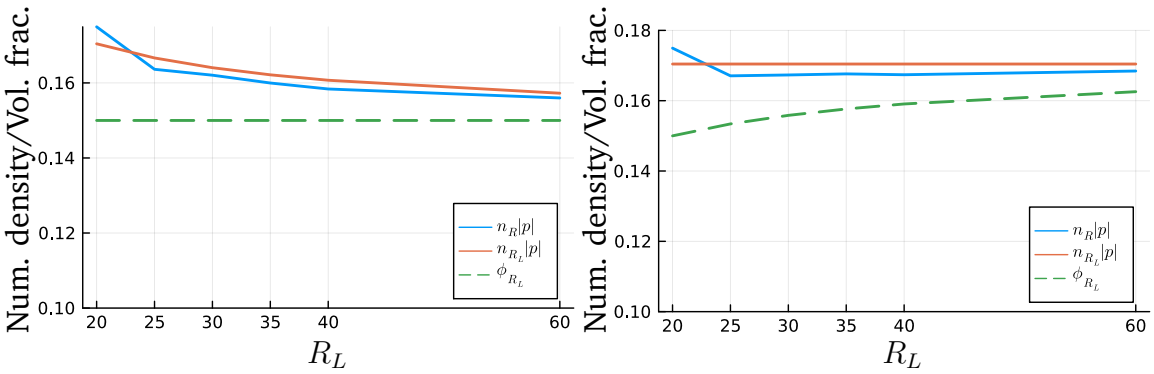

Figure 3.6: Both graphs show how the number density $\mathfrak{n}_R$ produced by the Cookie-cutter method varies when changing the larger region R_L. In both cases,the radius of the region is $R = 20$, and the radius of each particle is $a = 1$. On the left, the volume fraction ϕ_{R_L} is fixed, and we see how increasing R_L leads to a steady decrease in $\mathfrak{n}_R$. On the right, $\mathfrak{n}_{R_L}$ is fixed, then, although $\phi_{R_L} = \mathfrak{n}_{R_L}\dfrac{|\mathcal{R}_{R_L-a}|}{|\mathcal{R}_{R_L}|}$ increases with R_L, the number density $\mathfrak{n}_{R_L}$ changes little.

Figure 3.6 shows that if we fix the number density $\mathfrak{n}_{R_L}$, instead of fixing ϕ_{R_L}, we get only very small changes to the resulting number density $\mathfrak{n}_R$ when increasing R_L. In essence, we can just choose any R_L large enough, and then calculate $\mathfrak{n}_R$. Figure 3.7 shows the result of the changing $\mathfrak{n}_R$, when increasing R_L, and echoes the same results of Figure 3.6. Figure 3.8 shows that the boundary effect is more pronounced as the

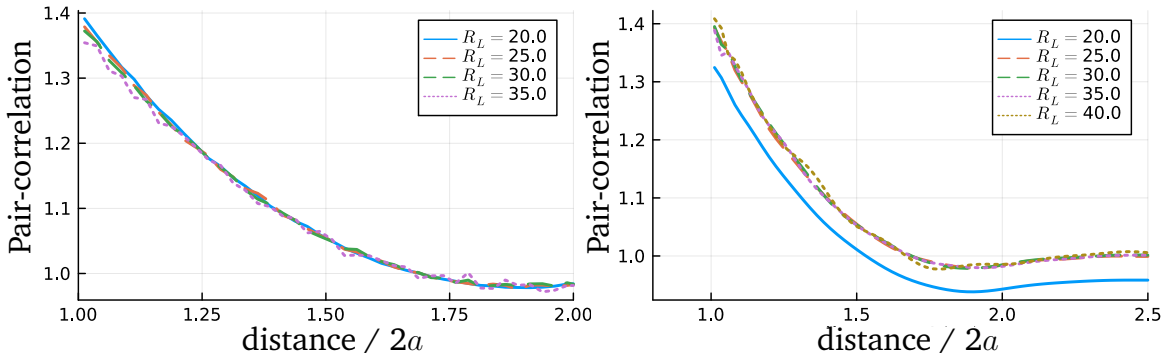

Figure 3.7: The pair-correlation, calculated using the Monte-Carlo method for each of the R_L values, is presented on the left (right) side corresponding to the cases depicted on the left (right) side of Figure 3.6. That is, on the left the value of ϕ_{R_L} is fixed, whereas on the right side, the value of $\mathfrak{n}_{R_L}$ is fixed.

particle volume fraction increases.

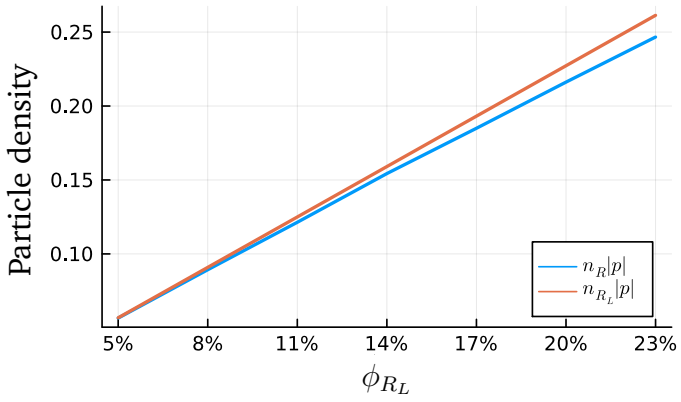

Figure 3.8: For the Cookie-cutter method, the particles are slightly more likely to appear near the boundary of the larger region, which is why $\mathfrak{n}_R < \mathfrak{n}_{R_L}$. This boundary effect becomes more pronounced as the volume fraction increases and limits the possible positions that particles can occupy.

The Monte-Carlo issue. The Cookie-cutter method, that uses Monte-Carlo (MC), should lead to the same pair-correlation of an infinite medium, which is well approximated by the Percus-Yevick (PY) method. When checking the literature, our Percus-Yevick results match those found by others, for example [1, 3, 19, 20, 21, 22]. However, we find that PY does not match the Cookie-cutter method when using the same number density. Let $\mathfrak{n}_{PY}$ be the number density used for PY. We find that $\mathfrak{n}_{PY}$ needs to be less than the number density of the Cookie-cutter method $\mathfrak{n}_R$ for the pair-correlations to be very similar. The main reason for that is the finite geometry of the region. The number density in the smaller region will be slightly less than the one of the larger region. This is due to particles still being more likely to appear near

the boundary of the large region, and as a result they reduce the number of particles within the smaller region.

See, for example Figure 3.9. The aimed volume fraction was $\phi_{\text{aim}} = 25\%$. Each particle has a radius of $a = 1.0$ and there is no separation gap between the particles. The true number density $\mathfrak{n}_\infty = 0.0635$ is estimated numerically, whereas the number density of the larger cookie region is $\mathfrak{n}_{\text{aim}} = 0.0678$. Note that $\mathfrak{n}_\infty|\mathfrak{p}| = 26.6\%$ and $\mathfrak{n}_{\text{aim}}|\mathfrak{p}| = 28.4\%$. The graph on the left side of Figure 3.9 shows the Cookie-cutter pair-correlation and PY with the same number density $\mathfrak{n}_\infty$, revealing that PY overestimates the pair-correlation. On the right, we lower the number density for PY and use $\mathfrak{n}_{PY} = \mathfrak{n}_\infty \dfrac{|\mathcal{R}_{R+d-a}|}{|\mathcal{R}_{R+d}|}$, where $R + d$ is the radius of the larger region of the Cookie-cutter method.

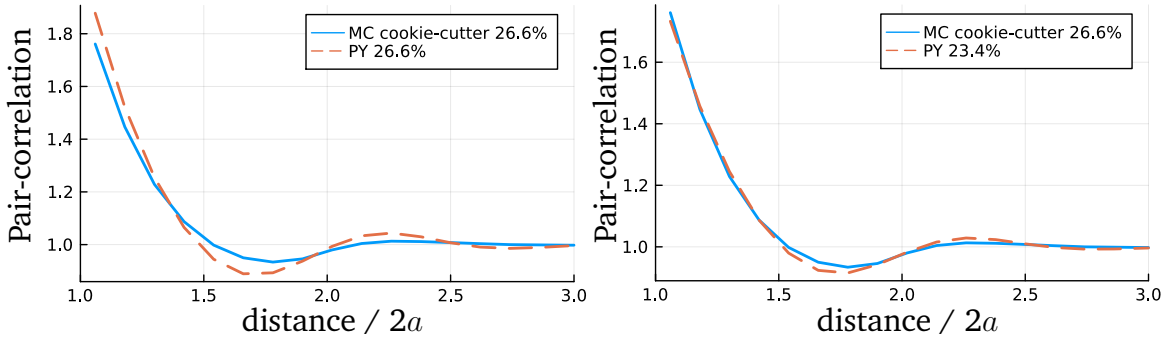

Figure 3.9: Comparison of pair-correlation functions with an aimed volume fraction at $\phi_{\text{aim}} = 25\%$. All particles are identical with a radius of $a = 1$ and no separation gap between them. On the left, we compare the Cookie-cutter method with the Percus-Yevick approximation, both using the same number density $\mathfrak{n}_\infty$. The right side illustrates the PY model after adjusting its number density to $\mathfrak{n}_{PY}$ to match Cookie-cutter spatial constraints.

3.4 Conclusions

In Section 3.1 we discussed the impact of including more than one effective wavenumber on reflection coefficients, an aspect critical for many measurement techniques. In Section 3.2, we addressed the mathematical and computational aspects of determining multiple effective wavenumbers in three dimensions identifying a gap in the existing literature with the development of an asymptotic method for locating these complex effective wavenumbers, particularly in the context of monopole scatterers. Further, Section 3.3, particularly Section 3.3.2, served as an essential bridge between the analytical and numerical aspects of this thesis. It tackled the challenges encountered in Monte-Carlo simulations when particles are confined within a finite region, and paved the way on how to place these particles in such a finite region to achieve a desired

pair-correlation. The results of this study indicate that if the particles are evenly distributed meaning they are similar to one another with little deviation from the mean, the Bounded-sphere method may be preferable. In contrast, for particles that are not evenly distributed, the Cookie-cutter method appears to be an effective method to avoid artefacts in pair-correlation and volume fraction caused by the boundary of the particulate.

Future avenues. The findings from this chapter provide a strong basis for further research in several key areas. Firstly, there is a need to further refine and validate the asymptotic method introduced here, especially to see how well it works with different types of scatterers other than monopoles. This can lead to more precise control over acoustic wave behaviour in materials, which is crucial for industries like medical imaging, and noise reduction. Secondly, we should explore how these findings can help in designing and understanding new materials that are designed to control how waves propagate through them. Lastly, by extending the Cookie-cutter method to address simulation artefacts, we can improve the accuracy of simulations used in material design and testing, thereby speeding up the development of new technologies and materials with optimised properties.

Author contributions

AK conceived of the study, wrote the manuscript, wrote all the code for the numerical calculations, developed the theoretical calculations, and produced all the figures.

Data and reproducibility

To produce our results we used the open source software [8], [9], [11] and [16].

References

[1] M. Adda-Bedia et al. 'Solution of the Percus-Yevick equation for hard disks'. In: *The Journal of Chemical Physics* 128.18 (May 2008). URL: http://dx.doi.org/10.1063/1.2919123.

[2] George B Arfken et al. *Mathematical methods for physicists*. 6th ed. San Diego, CA: Academic Press, July 2005.

[3] V.V. Bringi et al. 'The effects on pair correlation function of coherent wave attenuation in discrete random media'. In: *IEEE Transactions on Antennas and Propagation* 30.4 (July 1982), pp. 805–808. URL: https://doi.org/10.1109/tap.1982.1142852.

[4] Rémi Carminati et al. *Principles of Scattering and Transport of Light*. Cambridge University Press, June 2021. URL: https://doi.org/10.1017/9781316544693.

[5] Artur L. Gower et al. 'A proof that multiple waves propagate in ensemble-averaged particulate materials'. In: *Proceedings of the Royal Society A: Mathematical, Physical and Engineering Sciences* 475.2229 (Sept. 2019), p. 20190344. URL: http://dx.doi.org/10.1098/rspa.2019.0344.

[6] Artur L Gower et al. 'Effective waves for random three-dimensional particulate materials'. In: *New Journal of Physics* 23.6 (June 2021), p. 063083. URL: http://dx.doi.org/10.1088/1367-2630/abdfee.

[7] Artur L. Gower et al. 'Multiple Waves Propagate in Random Particulate Materials'. In: *SIAM Journal on Applied Mathematics* 79.6 (Jan. 2019), 2569–2592. URL: http://dx.doi.org/10.1137/18M122306X.

[8] Artur L Gower et al. 'MultipleScatering.jl: A Julia library for simulating, processing, and plotting multiple scattering of waves.' In: *github.com/JuliaWaveScattering/MultipleScattering.jl* (2020).

[9] Artur L Gower et al. 'ParticleCorrelations.jl: A package to calculate typical pair correlations (or structure factor) for disordered particulates, such as Percus-Yevick, and to calculate specific particle configurations from given pair correlation.' In: *github.com/arturgower/ParticleCorrelations.jl* (2023).

[10] Artur L. Gower et al. 'Reflection from a multi-species material and its transmitted effective wavenumber'. en. In: *Proc. R. Soc. A* 474.2212 (Apr. 2018), p. 20170864. URL: http://rspa.royalsocietypublishing.org/content/474/2212/20170864 (visited on 22/04/2018).

[11] Artur Lewis Gower. 'EffectiveWaves.jl: A Julia package to calculate ensemble averaged waves in heterogeneous materials'. Version 0.3.4. In: *github.com/JuliaWaveScattering/EffectiveWaves.jl* (Dec. 2018).

[12] C. M. Linton et al. 'Multiple Scattering by Multiple Spheres: A New Proof of the Lloyd-Berry Formula for the Effective Wavenumber'. In: *SIAM Journal on Applied Mathematics* 66.5 (2006), pp. 1649–1668. URL: http://www.jstor.org/stable/4096313 (visited on 26/04/2023).

[13] Francine Luppé et al. 'Effective wave numbers for thermo-viscoelastic media containing random configurations of spherical scatterers'. In: *The Journal of the Acoustical Society of America* 131.2 (Feb. 2012), pp. 1113–1120. URL: https://doi.org/10.1121/1.3672690.

[14] P. A. Martin. 'Multiple scattering by random configurations of circular cylinders: Reflection, transmission, and effective interface conditions'. In: *The Journal of the Acoustical Society of America* 129.4 (Apr. 2011), 1685–1695. URL: http://dx.doi.org/10.1121/1.3546098.

[15] P. A. Martin. *Multiple Scattering: Interaction of Time-Harmonic Waves with N Obstacles*. Cambridge University Press, Aug. 2006. URL: http://dx.doi.org/10.1017/CBO9780511735110.

[16] Patrick Kofod Mogensen et al. 'Optim: A mathematical optimization package for Julia'. In: *Journal of Open Source Software* 3.24 (2018), p. 615.

[17] K. Muinonen et al. 'Coherent backscattering verified numerically for a finite volume of spherical particles'. In: *The Astrophysical Journal* 760.2 (Nov. 2012), p. 118. URL: https://doi.org/10.1088/0004-637x/760/2/118.

[18] Karri Muinonen. 'Coherent backscattering of light by complex random media of spherical scatterers: numerical solution'. In: *Waves in Random Media* 14.3 (July 2004), pp. 365–388. URL: https://doi.org/10.1088/0959-7174/14/3/010.

[19] S Torquato et al. 'Random Heterogeneous Materials: Microstructure and Macroscopic Properties'. In: *Applied Mechanics Reviews* 55.4 (July 2002), B62–B63. URL: https://doi.org/10.1115/1.1483342.

[20] Salvatore Torquato. 'Inverse optimization techniques for targeted self-assembly'. In: *Soft Matter* 5.6 (2009), p. 1157. URL: https://doi.org/10.1039/b814211b.

[21] L. Tsang et al. 'Multiple scattering of acoustic waves by random distribution of discrete spherical scatterers with the quasicrystalline and Percus–Yevick approximation'. In: *The Journal of the Acoustical Society of America* 71.3 (Mar. 1982), 552–558. URL: http://dx.doi.org/10.1121/1.387524.

[22] Leung Tsang et al. *Scattering of Electromagnetic Waves: Numerical Simulations*. Wiley, May 2001. URL: http://dx.doi.org/10.1002/0471224308.

[23] J. R. Willis. 'Transmission and reflection at the boundary of a random two-component composite'. In: *Proc. R. Soc. A* 476.2235 (Mar. 2020), p. 20190811. URL: https://doi.org/10.1098/rspa.2019.0811.

[24] J.R. Willis. 'Some personal reflections on acoustic metamaterials'. In: *Wave Motion* 108 (Jan. 2022). URL: http://dx.doi.org/10.1016/j.wavemoti.2021.102834.

Chapter 4

Calculating pair-correlations from random particle configurations

ARISTEIDIS KARNEZIS, ART L. GOWER

Abstract

Particle pair-correlations are broadly used to describe particle distributions in chemistry, physics, and material science. Many theoretical methods require the pair-correlation to predict material properties such as fluid flow, thermal properties, or wave propagation. In all these applications it is either important to calculate a pair-correlation from specific particle configurations, or vice-versa: determine the likely particle configurations from a pair-correlation which is needed to fabricate a particulate material. Most available methods to calculate the pair-correlation from a particle configuration require that the configuration be very large to avoid effects from the boundary. Here we show how to avoid boundary effects even for small particle configurations. Having small particle configurations leads to far more efficient numerical methods. We also demonstrate how to use techniques from smooth nonlinear optimisation to quickly recover a particle configuration from a pair-correlation.

4.1 Introduction

Background. In the field of material science, the investigation of structural properties has witnessed significant progress. Molecular dynamics simulations, coupled with neutron and X-ray scattering experiments, have provided valuable insights into the structural characteristics of materials. For disordered materials, most techniques to probe and analyse these structures focus on the pair-correlation function and the structure factor [29, 30, 41, 42, 48]. The pair-correlation appears naturally in theoretical methods that use ensemble averaging [6, 8, 37, 51], whereas the structure factor appears naturally from scattering experiments [8, 11], including small-angle neutron scattering [7, 47].

The pair-correlation function, denoted by $\mathrm{g}(r)$, represents the probability of finding a pair of particles separated by a certain distance r [6, 8, 37, 51]. The structure factor, denoted by $\mathrm{S}(k)$, corresponds to the Fourier transform of $\mathrm{g}(r)$, and it is essential for characterising the structure of the material from the scattering intensity [8, 11, 12, 39].

Beyond material science, pair-correlations and structure factors extend to calculating shear viscosity, electrical conductivity, and thermal conductivity from a molecular perspective [35]. They also play a significant role in exploring complex phenomena such as the *nuclear pasta* observed in the extreme conditions of neutron star crusts [19, 20, 39]. This phenomenon, characterised by non-uniform arrangements of subatomic particles under extreme gravitational fields, is investigated through neutron and X-ray scattering to understand the internal structure of neutron stars [19, 20, 39].

Knowledge of the pair-correlation function and the structure factor is very useful when designing materials with specific behaviour. Indeed, they can be set in order to achieve specific properties such as hyperuniform structures, materials with exotic band gap profiles and negative refractive index [26, 32, 44, 46, 52]. By adjusting pair-correlations, we aim to create materials with specific properties and unique structural characteristics.

From the authors background, the pair-correlation appears when taking an ensemble average of waves in disordered materials [6, 15, 16, 54]. Essentially, the pair-correlation function captures the spatial distribution and arrangement of particles within a material, directly influencing how waves interact with and propagate through the material. That is, the pair-correlation is the only way the material structure affects wave propagation. This suggests a route to design materials to control waves:

1. To determine pair-correlations that lead to band-gaps, frequency filters, or enhanced transmission.
2. To determine configurations of particles that match the desired pair-correlation.

Step 2) is known as the realizability problem [10, 11, 24, 55, 59], and there are open questions about when it is possible to solve [9, 13, 14, 22, 30, 40].

Realizability problem. Determining a likely configuration of particles from a specific pair-correlation is called the realizability problem. To make the problem easier to understand, here is an example: Think about solving a jigsaw puzzle. Each puzzle piece is like a particle in a material. The goal is to fit all these pieces together within the puzzle board to create a picture. This picture represents our target arrangement of particles. However, just like puzzle pieces must fit together in a certain way and cannot be forced into the wrong place or overlap, the particles in our material must also be arranged in a physically feasible way. This means we can not just place them in any random configuration; they need to fit together according to physical laws, just like puzzle pieces. So, realizability is about making sure that the arrangement we come up with can actually exist in the real world.

The realizability problem appears in the study of many-body systems, such as liquids, and disordered materials [10, 11, 24, 25, 48, 49, 55, 57, 59]. One of the challenges is that the problem often lacks a unique solution. Multiple configurations of particles can result in the same pair-correlation, especially in disordered media where the properties and behaviour of particulates can be influenced by factors like particle size, shape and density [11, 50].

Several necessary conditions for potential pair-correlation functions have been identified, including the requirement of non-negativity to ensure realistic representation of properties such as density or probability distributions in materials, and restrictions on their associated structure factors, which measure variations in particle density within a material [48]. However, establishing a set of sufficient conditions for these functions remains an open challenge [48, 51]. We note that the problem is not completely resolved even in just one spatial dimension.

Reverse Monte-Carlo. Reverse Monte-Carlo structural modelling is one technique that has been used to calculate particle configurations that match a measured structure factors or pair-correlations [9, 13, 14, 22, 30, 40, 53]. Typically these Monte-Carlo simulations are guided by a Genetic Algorithm, or similar random searches, which are computationally intensive [28, 29, 30, 43, 53]. These methods are brute-force, and typically use non-gradient-based methods. While effective to some extent, they struggle when dealing with pair-correlation functions that lack smoothness. In response to

this limitation, we propose a novel approach based on smooth optimisation. Given the straightforward computations of gradients, it stands to reason that gradient-based optimisation methods [45] hold significant potential for superior performance over traditional non-gradient-based approaches. This advantage comes from their ability to efficiently move through the search space by using directional information, thus offering a more targeted and faster convergence to optimal particle arrangements.

Paper summary. In Section 4.2, we start by deducing in a simple self-contained way how to describe probability distributions and the pair-correlation in terms of a set of particles. In Section 4.3 we show how to avoid the effects of boundaries when calculating pair-correlations. The effects of boundaries are usually undesirable, and the details we present seem to be missing from most references. In Section 4.4 we show the same calculations again, but without the use of Dirac deltas for didactic purposes. In Section 4.5 we deduce the structure factor for isotropic distributions both from any given pair-correlation and a set of particles. These results are needed in Section 4.6, where we present a method to calculate a configuration of particles that matches a given structure factor. Developing more efficient methods to reconstruct particle configurations from pair-correlations remains an ongoing challenge in material science and computational chemistry [36]. The method we propose uses techniques from smooth nonlinear optimisation to improve the efficiency, which we are able to do because the structure factor is a smooth function of the particle positions. We also present some preliminary numerical results. Finally, in Section 4.7 we summarise what the paper achieved and possible future directions.

4.2 Particle distributions

Consider there are J particles placed within some region $\mathcal{R}$. That is, the centre of every particle $\boldsymbol{r}_j \in \mathcal{R}$. We represent one possible configuration of particles, or ensemble, by the set $\mathcal{X}^s$, where every $\boldsymbol{r} \in \mathcal{X}^s$ is the centre of a particle in the ensemble.

The function $\mathrm{p}(\boldsymbol{r})$ is the probability density of finding a particle centred at $\boldsymbol{r}$. We can approximate $\mathrm{p}(\boldsymbol{r})$ by defining a mesh of volume elements $V(\boldsymbol{v}_i)$, where the vector $\boldsymbol{v}_i$ is the centre of the volume element, and then counting the number of particles in each $V(\boldsymbol{v}_i)$ divided by the total number of particles. This allows us to introduce $\mathrm{p}_V(\boldsymbol{v}_i)$ as an approximation to $\mathrm{p}(\boldsymbol{v}_i)$, expressed as $\mathrm{p}(\boldsymbol{v}_i) \approx \mathrm{p}_V(\boldsymbol{v}_i)$, to estimate the probability:

$$\mathrm{p}_V(\boldsymbol{v}_i) = \frac{1}{S}\sum_{s}^{S} \frac{\#\left[\mathcal{X}^s \cap V(\boldsymbol{v}_i)\right]}{\#\mathcal{X}^s} \frac{1}{|V(\boldsymbol{v}_i)|}, \tag{4.1}$$

where $|V(\boldsymbol{v}_i)|$ is the volume of $V(\boldsymbol{v}_i)$, $\#\mathcal{X}$ is the number of elements in the set $\mathcal{X}$, and S is the number of ensembles considered. The use of a finite number of ensembles introduces a degree of statistical uncertainty. While increasing S can improve the accuracy of the approximation, it also increases computational demands. There is a trade-off between computational efficiency and statistical robustness. The chosen value of S should provide a reliable representation of particle distributions while remaining computationally manageable.
We require that the mesh:

$$V(\boldsymbol{v}_i) \cap V(\boldsymbol{v}_j) = \varnothing, \quad \text{for} \quad j \neq i,$$

ensuring that each volume element is distinct and non-overlapping. This is crucial for the independence of the measurements. It prevents double-counting of particles and ensures that each volume element contributes uniquely to the probability density calculation.

In a similar way, we can approximate $\mathrm{p}(\boldsymbol{x}_1, \boldsymbol{x}_2)$, which is the joint probability density of finding one particle centred at $\boldsymbol{x}_1$ and another centred at $\boldsymbol{x}_2$, while averaging over all over particle positions. If we assume that both $\boldsymbol{x}_1$ and $\boldsymbol{x}_2$ are distributed within $\mathcal{R}$, then we can approximate the function $\mathrm{p}(\boldsymbol{x}_1, \boldsymbol{x}_2)$ with the formula:

$$\mathrm{p}_V(\boldsymbol{v}_i, \boldsymbol{v}_j) = \frac{1}{S} \sum_{s}^{S} \frac{\#\left[\mathcal{X}^s \cap V(\boldsymbol{v}_i)\right]}{\#\mathcal{X}^s} \frac{\#\left[\mathcal{X}^s \cap V(\boldsymbol{v}_j)\right]}{\#\left[\mathcal{X}^s \backslash V(\boldsymbol{v}_i)\right]} \frac{1}{|V(\boldsymbol{v}_i)||V(\boldsymbol{v}_j)|}, \quad \text{for} \quad i \neq j, \quad (4.2)$$

where $\mathrm{p}_V(\boldsymbol{v}_i, \boldsymbol{v}_i) = 0$ for every i, and $\mathcal{X}^s \backslash V(\boldsymbol{v}_i)$ is defined as the set $\mathcal{X}^s$ without $V(\boldsymbol{v}_i)$. Note that:

$$\mathrm{p}(\boldsymbol{v}_i, \boldsymbol{v}_j) \approx \mathrm{p}_V(\boldsymbol{v}_i, \boldsymbol{v}_j),$$

for every $\boldsymbol{v}_i$ and $\boldsymbol{v}_j$. In simple terms, it allows us to estimate the probability of finding pairs of particles at specific positions within a material by statistically approximating the probability.

As expected, using this approximation, the integral of $\mathrm{p}(\boldsymbol{x}_1, \boldsymbol{x}_2)$ for $\boldsymbol{x}_1, \boldsymbol{x}_2 \in \mathcal{R}$

gives one:

$$\begin{aligned}\int \mathrm{p}(\boldsymbol{x}_1,\boldsymbol{x}_2)\mathrm{d}\boldsymbol{x}_1\mathrm{d}\boldsymbol{x}_2 &\approx \sum_{i,j}\mathrm{p}_V(\boldsymbol{v}_i,\boldsymbol{v}_j)|V(\boldsymbol{v}_i)||V(\boldsymbol{v}_j)| \\ &= \frac{1}{S}\sum_{s}^{S}\sum_{i}\sum_{j\neq i}\frac{\#\left[\mathcal{X}^s\cap V(\boldsymbol{v}_i)\right]}{\#\mathcal{X}^s}\frac{\#\left[\mathcal{X}^s\cap V(\boldsymbol{v}_j)\right]}{\#\left[\mathcal{X}^s\backslash V(\boldsymbol{v}_i)\right]} \\ &= \frac{1}{S}\sum_{s}^{S}\sum_{i}\frac{\#\left[\mathcal{X}^s\cap V(\boldsymbol{v}_i)\right]}{\#\mathcal{X}^s}\frac{\#\left[\mathcal{X}^s\cap \cup_{j\neq i}V(\boldsymbol{v}_j)\right]}{\#\left[\mathcal{X}^s\backslash V(\boldsymbol{v}_i)\right]} \\ &= \frac{1}{S}\sum_{s}^{S}\frac{\#\left[\mathcal{X}^s\cap \cup_{i}V(\boldsymbol{v}_i)\right]}{\#\mathcal{X}^s} = 1, \end{aligned} \tag{4.3}$$

where we used that $\cup_i V(\boldsymbol{v}_i)=\mathcal{R}$, $\mathrm{d}\boldsymbol{x}_1\approx|V(\boldsymbol{v}_i)|$,$\mathrm{d}\boldsymbol{x}_2\approx|V(\boldsymbol{v}_j)|$, and $\mathcal{R}\cap\cup_{j\neq i}V(\boldsymbol{v}_j)=\mathcal{R}\backslash V(\boldsymbol{v}_i)$ which implies that $\mathcal{X}^s\cap\cup_{j\neq i}V(\boldsymbol{v}_j)=\mathcal{X}^s\backslash V(\boldsymbol{v}_i)$.

The term that often appears in methods that use ensemble averaging of particulates [4, 51, 54] is the particle pair-correlation, which is defined as:

$$\mathrm{g}(\boldsymbol{x}_1,\boldsymbol{x}_2) := \frac{J-1}{J}\frac{\mathrm{p}(\boldsymbol{x}_1,\boldsymbol{x}_2)}{\mathrm{p}(\boldsymbol{x}_1)\mathrm{p}(\boldsymbol{x}_2)}, \tag{4.4}$$

where $J=\#\mathcal{X}_s$ is the total number of particle, where we have assumed that every configuration $\#\mathcal{X}_s$ has the same number of particles. The factor $\frac{J-1}{J}$ is correction for a finite number of particles in a region when calculating the pair-correlation function $\mathrm{g}(\boldsymbol{x}_1,\boldsymbol{x}_2)$. In an infinite region, as particles become uncorrelated due to distance or lack of interaction, the pair-correlation approaches 1, indicating a random distribution without any correlation between particle positions. However, in a finite region, the presence of a limited number of particles introduces a bias because each particle is slightly more likely to be closer to another particle than it would be in an infinite region. The correction factor $\frac{J-1}{J}$ adjusts for this bias by scaling down the correlation as the number of particles increases, ensuring that $\mathrm{g}(\boldsymbol{x}_1,\boldsymbol{x}_2)\to 1$ for large distances between particles or when particles become uncorrelated as confirmed by [54, Equation (8.1.2)]. We demonstrate this in the next section.

4.2.1 Particles as Dirac delta

For a finite, but very large number, of particles we can rewrite the pair-correlation in terms of Dirac deltas. For example, turning to (4.1) we assume there is a finite number of ensembles S, each with a finite number of particles J. Then we can make

the volume elements $V(\boldsymbol{v}_i)$ small enough so that there is at most one particle in each volume element, which implies that $\#\mathcal{X}^s = J$ and:

$$\#\left[\mathcal{X}^s \cap V(\boldsymbol{v}_i)\right] = \begin{cases} 1, & \text{if there is a particle in } V(\boldsymbol{v}_i), \\ 0, & \text{if there is no particle in } V(\boldsymbol{v}_i). \end{cases} \tag{4.5}$$

For notational convenience, we choose the mesh of volume elements such that each element is centred at a particle $\boldsymbol{r}_i \in \mathcal{X}^s$, if it contains a particle. Equation (4.5) allows us to rewrite (4.1) in the form:

$$\mathrm{p}_V(\boldsymbol{r}_i) = \frac{1}{S}\sum_{s}^{S} \frac{1}{|V(\boldsymbol{r}_i)|}\frac{1}{J}, \tag{4.6}$$

for every $\boldsymbol{r}_i \in \mathcal{X}^s$.

As we are taking the limit of all the volume elements going to zero, $|V(\boldsymbol{r}_i)| \to 0$, we can approximate:

$$\mathrm{p}(\boldsymbol{x}) = \begin{cases} \mathrm{p}_V(\boldsymbol{r}_i), & \text{if } \boldsymbol{x} \in V(\boldsymbol{r}_i), \\ 0, & \text{else}, \end{cases}$$

where $\mathrm{p}(\boldsymbol{x}) = 0$ if $\boldsymbol{x}$ is in a volume element that does not contain a particle. With this definition, and taking the limit $|V(\boldsymbol{v}_i)| \to 0$ for every i, we can rewrite (4.1) in the form:

$$\mathrm{p}(\boldsymbol{x}) = \frac{1}{JS}\sum_{s}^{S}\sum_{\boldsymbol{r}_i \in \mathcal{X}^s} \delta(\boldsymbol{x} - \boldsymbol{r}_i), \tag{4.7}$$

where $\delta(\boldsymbol{x} - \boldsymbol{r}_i)$ is the Dirac delta function. This allows each volume element to represent an infinitesimally small point in space, effectively turning each particle into a point particle. For details on the Dirac delta see [2].

Repeating analogous steps for the joint probability density (4.2) we obtain:

$$\mathrm{p}(\boldsymbol{x}_1, \boldsymbol{x}_2) = \frac{1}{S}\frac{1}{J(J-1)}\sum_{s}^{S}\sum_{\boldsymbol{r}_i \in \mathcal{X}^s}\sum_{\boldsymbol{r}_j \neq \boldsymbol{r}_i, \boldsymbol{r}_j \in \mathcal{X}^s} \delta(\boldsymbol{x}_1 - \boldsymbol{r}_i)\delta(\boldsymbol{x}_2 - \boldsymbol{r}_j). \tag{4.8}$$

In (4.8), the outer summation over all ensembles S accounts for the randomness and is essential for capturing the statistical variation across different possible configurations of particles within the material. The inner summation considers all pairs of particles $\boldsymbol{r}_i$ and $\boldsymbol{r}_j$ within each ensemble, excluding cases where $\boldsymbol{r}_i = \boldsymbol{r}_j$ because a particle

cannot pair with itself. This guarantees that the model accurately represents the joint probability of finding two distinct particles at two specific points.

This method provides a robust and flexible framework for statistical analysis across a wide range of densities, especially in disordered systems. However, it can be computationally intensive due to the high level of detail and precision it requires. As each particle is represented as a point in space, the computations involve handling potentially large numbers of Dirac delta functions.

4.2.2 Isotropic distributions

For most of this paper we focus on homogeneous and isotropic distributions. The homogeneous assumption dictates that the particles are equally likely to be placed anywhere in space, which leads to $\mathrm{p}(\boldsymbol{r})$ being a constant. If we choose all volume elements to have the same volume $|V(\boldsymbol{v}_i)| = |V|$, then using that $\mathrm{p}_V(\boldsymbol{v}_i)$ is a constant together with (4.1) leads to:

$$\mathrm{p}_V(\boldsymbol{v}_j) = \frac{1}{SI}\sum_i\sum_s^S \frac{\#\left[\mathcal{X}^s \cap V(\boldsymbol{v}_i)\right]}{\#\mathcal{X}^s}\frac{1}{|V|} = \frac{1}{SI}\frac{1}{|V|}\sum_s^S \frac{\#\left[\mathcal{X}^s \cap \cup_i V(\boldsymbol{v}_i)\right]}{\#\mathcal{X}^s} = \frac{1}{I|V|} = \frac{1}{|\mathcal{R}|}, \tag{4.9}$$

where I is the total number of volume elements $V(\boldsymbol{v}_i)$, $|\mathcal{R}|$ is the volume of $\mathcal{R}$, and we used $\cup_i V(\boldsymbol{v}_i) = \mathcal{R}$ and similarity $I|V| = |\mathcal{R}|$.

For an isotropic distribution we have that only the inter-particle distance is needed for their joint probability [37, 38]. That is $\mathrm{p}(\boldsymbol{x}_1, \boldsymbol{x}_2) = \mathrm{p}(|\boldsymbol{x}_1 - \boldsymbol{x}_2|)$, where $|\boldsymbol{r}|$ is the magnitude of the vector $\boldsymbol{r}$. To use this property to simplify the formula for the pair-correlation (4.4), we start by writing:

$$\mathrm{g}(|\boldsymbol{x}_1 - \boldsymbol{x}_2|) = \mathrm{g}(\boldsymbol{x}_1, \boldsymbol{x}_2), \tag{4.10}$$

then integrate both sides over all values such that $|\boldsymbol{x}_1 - \boldsymbol{x}_2| = z$ for fixed z relative to the variables of integration. To make this clearer we introduce the ball region using standard set-builder notation:

$$\mathcal{B}(\boldsymbol{x}; r) = \{\boldsymbol{y} \in \mathbb{R}^3 : \ |\boldsymbol{x} - \boldsymbol{y}| \leq r\}. \tag{4.11}$$

The ball region is introduced to simplify the process of integrating over distances. It defines a spherical region of radius r around a point $\boldsymbol{x}$, which is essential for transforming the pair-correlation function into a function of distance alone.

Using this notation, we will integrate both sides of (4.10) over every $\boldsymbol{x}_2 \in$

$\partial\mathcal{B}(\boldsymbol{x}_1; z) \cap \mathcal{R}$, followed by over all $\boldsymbol{x}_1 \in \mathcal{R}$, which results in:

$$\int_{\mathcal{R}} \int_{\partial\mathcal{B}(\boldsymbol{x}_1;z)\cap\mathcal{R}} \mathrm{g}(|\boldsymbol{x}_1 - \boldsymbol{x}_2|)\mathrm{d}S_2\mathrm{d}\boldsymbol{x}_1 = \int_{\mathcal{R}} \int_{\partial\mathcal{B}(\boldsymbol{x}_1;z)\cap\mathcal{R}} \mathrm{g}(\boldsymbol{x}_1, \boldsymbol{x}_2)\mathrm{d}S_2\mathrm{d}\boldsymbol{x}_1. \tag{4.12}$$

Here, $\boldsymbol{x}_1$ represents the position of a particle within the region $\mathcal{R}$, $\boldsymbol{x}_2$ is the position of another particle, and $\partial\mathcal{B}(\boldsymbol{x}_1; z)$ is the surface of a sphere with radius z centred at $\boldsymbol{x}_1$. Physically, this means we are looking at all possible positions a second particle could occupy that are exactly a distance z away from the first particle, and we are integrating the pair-correlation function over the spherical surface that lies within the region $\mathcal{R}$, to understand how particle density varies at this specific separation distance. The left side of (4.12) can move out of the integral, resulting in:

$$\int_{\mathcal{R}} \int_{\partial\mathcal{B}(\boldsymbol{x}_1;z)\cap\mathcal{R}} \mathrm{g}(z)\mathrm{d}S_2\mathrm{d}\boldsymbol{x}_1 = L(z)\mathrm{g}(z), \text{ with } L(z) = \int_{\mathcal{R}} \int_{\partial\mathcal{B}(\boldsymbol{x}_1;z)\cap\mathcal{R}} \mathrm{d}S_2\mathrm{d}\boldsymbol{x}_1. \tag{4.13}$$

For the right side of (4.12) we use the definition (4.4), and then rearrange (4.12) to reach:

$$\mathrm{g}(z) = \frac{J-1}{J}\frac{1}{L(z)} \int_{\mathcal{R}} \int_{\partial\mathcal{B}(\boldsymbol{x}_1;z)\cap\mathcal{R}} \frac{\mathrm{p}(\boldsymbol{x}_1, \boldsymbol{x}_2)}{\mathrm{p}(\boldsymbol{x}_1)\mathrm{p}(\boldsymbol{x}_2)}\mathrm{d}\boldsymbol{x}_1\mathrm{d}S_2. \tag{4.14}$$

To reach a simple formula to calculate $\mathrm{g}(z)$, we need to calculate the integral $L(z)$. In general, calculating $L(z)$ can be awkward and we show how to avoid this in the next section.

To simplify the radial pair-correlation (4.14) we combine (4.8) and (4.9) to write the pair-correlation (4.4) in terms of Dirac delta functions, which we then substituted into (4.14), and integrate over $\boldsymbol{x}_1$ to obtain:

$$\mathrm{g}(z) = \frac{1}{S}\frac{1}{\mathfrak{n}^2} \sum_{s}^{S} \sum_{\boldsymbol{r}_i \in \mathcal{X}^s} \sum_{\boldsymbol{r}_j \neq \boldsymbol{r}_i, \boldsymbol{r}_j \in \mathcal{X}^s} \frac{1}{L(z)} \int_{\partial\mathcal{B}(\boldsymbol{r}_i;z)\cap\mathcal{R}} \delta(\boldsymbol{x}_2 - \boldsymbol{r}_j)\mathrm{d}S_2. \tag{4.15}$$

where $\mathfrak{n} := J/|\mathcal{R}|$ is the particle number density. To simplify (4.15), note that because $\boldsymbol{r}_j \in \mathcal{R}$ we have that:

$$\int_{\partial\mathcal{B}(\boldsymbol{r}_i;z)\cap\mathcal{R}} \delta(\boldsymbol{x}_2 - \boldsymbol{r}_j)\mathrm{d}S_2 = \int_{\partial\mathcal{B}(\boldsymbol{r}_i;z)} \delta(\boldsymbol{x}_2 - \boldsymbol{r}_j)\mathrm{d}S_2.$$

At greater length, this is a result of the integral over $\boldsymbol{x}_2 \notin \mathcal{R}$ having an integrand which

is zero, $\delta(\boldsymbol{x}_2 - \boldsymbol{r}_j) = 0$, because $\boldsymbol{r}_j \in \mathcal{R}$, allowing us to rewrite (4.15) in the form:

$$\mathrm{g}(z) = \frac{1}{S}\frac{1}{\mathfrak{n}^2}\sum_{s}^{S}\sum_{\boldsymbol{r}_i\in\mathcal{X}^s}\sum_{\boldsymbol{r}_j\neq\boldsymbol{r}_i,\boldsymbol{r}_j\in\mathcal{X}^s}\frac{1}{L(z)}\int_{\partial\mathcal{B}(\mathbf{0};z)}\delta(\boldsymbol{r}_i - \boldsymbol{r}_j + \boldsymbol{x})\mathrm{d}S_x, \tag{4.16}$$

where we used the change of variables $\boldsymbol{x} = \boldsymbol{x}_2 - \boldsymbol{r}_i$. The change of variables to $\boldsymbol{x} = \boldsymbol{x}_2 - \boldsymbol{r}_i$ essentially shifts the centre of the sphere to the origin. We can now show how the Dirac delta function can be used to isolate the contribution of particle pairs at exactly distance z apart:

$$\int_{\partial\mathcal{B}(\mathbf{0};z)}\delta(\boldsymbol{r} + \boldsymbol{x})\mathrm{d}S_x = \delta(|\boldsymbol{r}| - z), \tag{4.17}$$

by noting that for any $z_1 < z_2$ we have that:

$$\int_{z_1}^{z_2}\int_{\partial\mathcal{B}(\mathbf{0};z)}\delta(\boldsymbol{r} + \boldsymbol{x})\mathrm{d}S_x\mathrm{d}z = \int_{\mathcal{B}(\mathbf{0};z_2)\setminus\mathcal{B}(\mathbf{0};z_1)}\delta(\boldsymbol{r} + \boldsymbol{x})\mathrm{d}V_x = \begin{cases} 1, & \text{if } z_1 < |\boldsymbol{r}| < z_2, \\ 0, & \text{else}, \end{cases} \tag{4.18}$$

where we note that $\mathrm{d}S_x\mathrm{d}z = \mathrm{d}V_x$ is a volume element. Considering the properties of the Dirac delta [2], equation (4.18) can be used to deduce (4.17).

Substituting these results into (4.16) leads to:

$$\mathrm{g}(z) = \frac{1}{S}\frac{1}{\mathfrak{n}^2 L(z)}\sum_{s}^{S}\sum_{\boldsymbol{r}_i\in\mathcal{X}^s}\sum_{\boldsymbol{r}_j\neq\boldsymbol{r}_i,\boldsymbol{r}_j\in\mathcal{X}^s}\delta(|\boldsymbol{r}_i - \boldsymbol{r}_j| - z). \tag{4.19}$$

The only change in (4.19) when changing from three spatial dimensions to two spatial dimensions is that $L(z)$ is given by (4.13) but with $\mathcal{R}$ being two dimensional and the integral over S_2 being a line integral.

4.3 Particles in two regions

To avoid the influence of the boundary that encloses the particles, and avoid calculating $L(z)$ appearing in (4.33), we consider two different regions where particles can be placed $\mathcal{R}_1$ and $\mathcal{R}_2$ as shown in Figure 4.1. We consider that $\boldsymbol{x}_1$ and $\boldsymbol{x}_2$ are two different random variables with $\boldsymbol{x}_1 \in \mathcal{R}_1$ and $\boldsymbol{x}_2 \in \mathcal{R}_2$. Note that $\mathcal{R}_1 \subset \mathcal{R}_2$, so, the particles J_1 of $\mathcal{R}_1$ are a subset of particles J_2 of $\mathcal{R}_2$. This setup allows for a focus on the internal interactions within $\mathcal{R}_1$ while minimising the boundary effects from $\mathcal{R}_2$.

To calculate the joint probability distribution $\mathrm{p}(\boldsymbol{x}_1, \boldsymbol{x}_2)$, let $\mathcal{X}^s$ be such that every

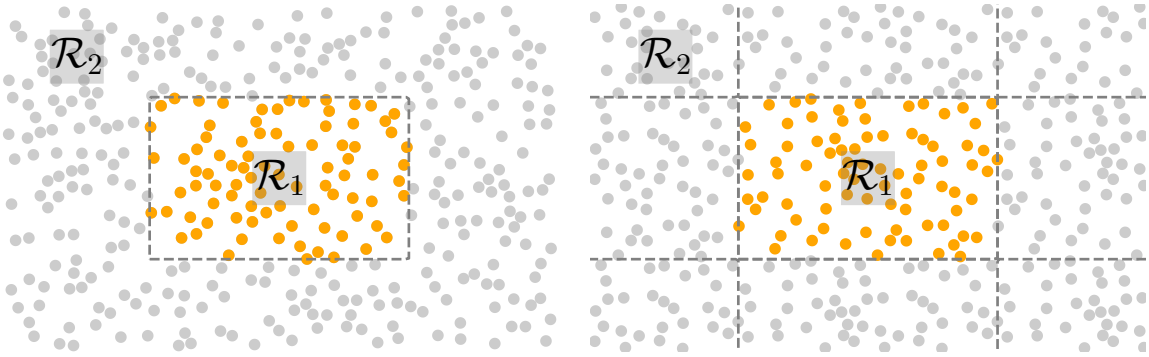

Figure 4.1: The left image shows a finite set of particles in a region $\mathcal{R}_1$ taken from a larger set of disordered particles in the region $\mathcal{R}_2$. Note that $\mathcal{R}_1$ is contained within $\mathcal{R}_2$. On the right a unit cell of random particles in a region $\mathcal{R}_1$ that is periodically tilled. On the right, the region $\mathcal{R}_2$ is a cut out from the periodic tilling of the particles in $\mathcal{R}_1$. We use ℓ to indicate the minimum length of periodicity, which is the height of the unit cell shown in the image on the right.

$\boldsymbol{x}_2 \in \mathcal{X}^s$ is also in $\boldsymbol{x}_2 \in \mathcal{R}_2$, then considering that $\boldsymbol{x}_1 \in \mathcal{R}_1$ and $\boldsymbol{x}_2 \in \mathcal{R}_2$ we have that:

$$\mathrm{p}_V(\boldsymbol{v}_i, \boldsymbol{v}_j) = \frac{1}{S}\sum_{s}^{S} \frac{\#\left[\mathcal{X}^s \cap V(\boldsymbol{v}_i)\right]}{\#[\mathcal{X}^s \cap \mathcal{R}_1]} \frac{\#\left[\mathcal{X}^s \cap V(\boldsymbol{v}_j)\right]}{\#[\mathcal{X}^s \backslash V(\boldsymbol{v}_i)]} \frac{1}{|V(\boldsymbol{v}_i)||V(\boldsymbol{v}_j)|} \quad \text{for } i \neq j, \tag{4.20}$$

such that $\boldsymbol{v}_i \in \mathcal{R}_1$, $\boldsymbol{v}_j \in \mathcal{R}_2$, and $V(\boldsymbol{v}_i) \cap V(\boldsymbol{v}_j) = \varnothing$ for every i, j, and:

$$\cup_{i=1}^{J_1} V(\boldsymbol{v}_i) = \mathcal{R}_1 \quad \text{and} \quad \cup_{j=1}^{J_2} V(\boldsymbol{v}_j) = \mathcal{R}_2.$$

As a check of the formula (4.20), performing an integral of $\mathrm{p}_V(\boldsymbol{v}_i, \boldsymbol{v}_j)$ for $\boldsymbol{v}_i \in \mathcal{R}_1$ and $\boldsymbol{v}_j \in \mathcal{R}_2$ gives 1 as expected by following similar steps as shown in (4.3).

For the two different regions, the definition of the particle pair-correlation (4.4) now becomes:

$$\mathrm{g}(\boldsymbol{x}_1, \boldsymbol{x}_2) := \frac{J_2 - 1}{J_2} \frac{\mathrm{p}(\boldsymbol{x}_1, \boldsymbol{x}_2)}{\mathrm{p}(\boldsymbol{x}_1)\mathrm{p}(\boldsymbol{x}_2)}, \tag{4.21}$$

where $J_2 = \#\mathcal{X}^s$.

4.3.1 Isotropic distributions

The probability density for the two regions, and an isotropic distribution of particles, is similar to before with:

$$\mathrm{p}(\boldsymbol{x}_1) = \frac{1}{|\mathcal{R}_1|} \quad \text{and} \quad \mathrm{p}(\boldsymbol{x}_2) = \frac{1}{|\mathcal{R}_2|}. \tag{4.22}$$

Using analogous steps shown in Section 4.2.2 to reach (4.19) we can reach:

$$\mathrm{g}(z) = \frac{1}{\mathfrak{n}^2 L(z)} \frac{1}{S} \sum_{s}^{S} \sum_{r_i \in \mathcal{X}^s \cap \mathcal{R}_1} \sum_{r_j \neq r_i, r_j \in \mathcal{X}^s} \delta(|\boldsymbol{r}_i - \boldsymbol{r}_j| - z). \tag{4.23}$$

Equation (4.23) "selects" only those particle pairs whose separation distance is exactly z. It does this by being zero everywhere except where its argument is zero. In this case, it becomes non-zero only when $|\boldsymbol{r}_i - \boldsymbol{r}_j| = z$.

However, now we can explicitly calculate $L(z)$ given by:

$$L(z) = \int_{\mathcal{R}_1} \int_{\partial \mathcal{B}(\boldsymbol{x}_1; z) \cap \mathcal{R}_2} \mathrm{d}S_2 \mathrm{d}\boldsymbol{x}_1. \tag{4.24}$$

Assume we want to calculate $\mathrm{g}(z)$ for $0 \leq z \leq Z$. To do this we can require that: the distance between the boundaries $\partial\mathcal{R}_2$ and $\partial\mathcal{R}_1$ be greater than or equal to Z. This condition ensures that for any $z \leq Z$, any point $\boldsymbol{x}_2$ on the surface of the sphere $\mathcal{B}(\boldsymbol{x}_1; z)$ is also within $\mathcal{R}_2$. This is crucial for the validity of the pair-correlation calculation, as it guarantees that the integration domain over S_2 becomes the entire surface of the sphere, simplifying the computation of $L(z)$. In other words, the domain of integration over S_2 becomes $\partial\mathcal{B}(\boldsymbol{x}_1; z) \cap \mathcal{R}_2 = \partial\mathcal{B}(\boldsymbol{x}_1; z)$, which used in (4.24) for three spatial dimensions leads to:

$$L(z) = 4\pi z^2 |\mathcal{R}_1|. \tag{4.25}$$

As a quick check, if $\mathcal{R}_2$ was a sphere with radius R_2 centred at the origin, then, $\int_0^{R_2} L(z)\mathrm{d}z = |\mathcal{R}_1||\mathcal{R}_2|$ as it should. Substituting (4.24) into (4.23) leads to:

$$\mathrm{g}_3(z) = \frac{1}{4\pi\mathfrak{n} z^2 J_1} \frac{1}{S} \sum_{s}^{S} \sum_{r_i \in \mathcal{X}^s \cap \mathcal{R}_1} \sum_{r_j \neq r_i, r_j \in \mathcal{X}^s} \delta(|\boldsymbol{r}_i - \boldsymbol{r}_j| - z), \quad \text{(3D spatial)}, \tag{4.26}$$

where $J_1 = \#[\mathcal{X}^s \cap \mathcal{R}_1]$, and we use g_3 instead of g to indicate that (4.26) is for 3 spatial dimensions.

For two spatial dimensions we have $L(z) = 2\pi z |\mathcal{R}_1|$ which substituted into (4.23) leads to:

$$\mathrm{g}_2(z) = \frac{1}{2\pi\mathfrak{n} z J_1} \frac{1}{S} \sum_{s}^{S} \sum_{r_i \in \mathcal{X}^s \cap \mathcal{R}_1} \sum_{r_j \neq r_i, r_j \in \mathcal{X}^s} \delta(|\boldsymbol{r}_i - \boldsymbol{r}_j| - z), \quad \text{(2D spatial)}. \tag{4.27}$$

Next, we re-deduce (4.26) and (4.27) without using Dirac delta functions.

4.4 The discrete form for isotropic pair-correlations

In this section we redo the calculations that lead to (4.26) and (4.27) but without the use of the Dirac delta function. That is, without taking the limit of volume elements tending to zero as used to reach (4.7). Doing this serves two purposes:

- It can be simpler to understand these discrete formulas, and implement them as a numerical method.
- It helps to verify the formulas by reaching formulas we can compare with literature and having two avenues to deduce the same formulas.

4.4.1 Particles in one region

Here we consider that all particles are within one region, $\boldsymbol{r}_i, \boldsymbol{r}_j \in \mathcal{X}^s$, and re-deduce the results that led to the formula (4.19) but without Dirac deltas.

To reach a simple formula for $\mathrm{g}(z)$ with the discrete approximation (4.2), we discretise the integral in (4.14), substitute (4.2), and use the discrete approximation for the differentials:

$$\mathrm{d}\boldsymbol{x}_1 = |V(\boldsymbol{v}_i)|, \quad \mathrm{d}z\mathrm{d}S_2 = |V(\boldsymbol{v}_j)|, \tag{4.28}$$

to obtain:

$$\mathrm{g}(z) = \frac{J-1}{J}\frac{|\mathcal{R}|^2}{L(z)\mathrm{d}zS}\sum_{s}^{S}\sum_{i}\sum_{|\boldsymbol{v}_i-\boldsymbol{v}_j|\approx z}\frac{\#\left[\mathcal{X}^s \cap V(\boldsymbol{v}_i)\right]}{\#\mathcal{X}^s}\frac{\#\left[\mathcal{X}^s \cap V(\boldsymbol{v}_j)\right]}{\#\left[\mathcal{X}^s \backslash V(\boldsymbol{v}_i)\right]}, \tag{4.29}$$

where we used (4.9) to substitute $\mathrm{p}(\boldsymbol{x}_1) = \mathrm{p}(\boldsymbol{x}_2) = 1/|\mathcal{R}|$, and the sum over j is for every $\boldsymbol{v}_j$ such that $z - \mathrm{d}z/2 < |\boldsymbol{v}_i - \boldsymbol{v}_j| < z + \mathrm{d}z/2$. As the minimum value for $z = 2a$, we just set $\mathrm{g}(z) = 0$ for $z \leq 2a$, where a denotes the radius of the particle.

At this point, due to the choice (4.28), the volumes $|V(\boldsymbol{v}_i)|$ and $|V(\boldsymbol{v}_j)|$ do not appear explicitly in (4.29). This allows us to simplify the formula by choosing $V(\boldsymbol{v}_i)$ and $V(\boldsymbol{v}_j)$ to be sufficiently small so that they each contain no more than one particle. For the indices i and j where there is no particle in $V(\boldsymbol{v}_i)$ and $V(\boldsymbol{v}_j)$ respectively, we have $\#\left[\mathcal{X}^s \cap V(\boldsymbol{v}_i)\right] = 0$ and $\#\left[\mathcal{X}^s \cap V(\boldsymbol{v}_j)\right] = 0$. This makes it convenient now to only sum over the i, and j where:

$$\#\left[\mathcal{X}^s \cap V(\boldsymbol{v}_i)\right] = \#\left[\mathcal{X}^s \cap V(\boldsymbol{v}_j)\right] = 1, \tag{4.30}$$

$$\#\left[\mathcal{X}^s \backslash V(\boldsymbol{v}_i)\right] = \#\mathcal{X}^s - 1 = J - 1, \tag{4.31}$$

which used in (4.29) leads to:

$$\mathrm{g}(z) = \frac{1}{\mathfrak{n}^2}\frac{1}{L(z)dzS}\sum_{s}^{S}\sum_{i}\sum_{|\boldsymbol{v}_i-\boldsymbol{v}_j|\approx z} 1, \tag{4.32}$$

where we used the particle number density $\mathfrak{n} := J/|\mathcal{R}|$. Now, when the volume elements $V(\boldsymbol{v}_i)$ and $V(\boldsymbol{v}_j)$ are significantly small, approaching zero there is only one particle centre in $V(\boldsymbol{v}_i)$ and one other particle centre in $V(\boldsymbol{v}_j)$. In this limit, $\boldsymbol{v}_i$ and $\boldsymbol{v}_j$ approximate the actual positions $\boldsymbol{r}_i$ and $\boldsymbol{r}_j$ in $\mathcal{X}^s$, which means we can sum over the actual positions $\boldsymbol{r}_i$ and $\boldsymbol{r}_j$ instead of the volume elements $\boldsymbol{v}_i$ and $\boldsymbol{v}_j$. This leads us to rewrite (4.32) in the reduced form:

$$\mathrm{g}(z) = \frac{1}{\mathfrak{n}^2 L(z)\mathrm{d}zS}\sum_{s}^{S}\sum_{\boldsymbol{r}_i\in\mathcal{X}^s}\#\mathcal{X}_i^s(z), \quad \text{(discrete pair-correlation)}, \tag{4.33}$$

where $\mathcal{X}_i^s(z)$ are all the particles $\boldsymbol{r}_j$ such that are $|\boldsymbol{r}_i - \boldsymbol{r}_j| \approx z$, or, more precisely with set builder notation:

$$\mathcal{X}_i^s(z) := \{\boldsymbol{r}_j \in \mathcal{X}^s : z - \mathrm{d}z/2 \leq |\boldsymbol{r}_i - \boldsymbol{r}_j| < z + \mathrm{d}z/2\}, \tag{4.34}$$

and $\#\mathcal{X}_i^s(z)$ is the number of elements in $\mathcal{X}_i^s(z)$.

The only change in the formula (4.32) when changing from three spatial dimensions to two spatial dimensions is that $L(z)$ is given by (4.13) but with $\mathcal{R}$ being two dimensional and the integral over S_2 being a line integral.

Now, to show that the discrete pair-correlation function (4.33) is equivalent to (4.19) involving the Dirac delta, we need to show that:

$$\lim_{\mathrm{d}z\to 0}\frac{\#\mathcal{X}_i^s(z)}{\mathrm{d}z} = \sum_{r_j\neq r_i, r_j\in\mathcal{X}^s}\delta(|\boldsymbol{r}_i - \boldsymbol{r}_j| - z). \tag{4.35}$$

To verify (4.35), let us define:

$$f(x) = \begin{cases} 1, & \text{if} \quad z - \mathrm{d}z/2 \leq x \leq z + \mathrm{d}z/2, \\ 0, & \text{otherwise}. \end{cases}$$

Then, $\#\mathcal{X}_i^s(z) = \sum_{r_j\neq r_i, r_j\in\mathcal{X}^s} f(|\boldsymbol{r}_i - \boldsymbol{r}_j|)$. To complete the demonstration of (4.35) we

note that for any x we have that:

$$\lim_{\mathrm{d}z\to 0} \frac{f(x)}{\mathrm{d}z} = \delta(x-z). \tag{4.36}$$

Equation (4.36) becomes infinitely high and narrow while integrating to 1, precisely picking out values at $x = z$.

4.4.2 Particles in two regions

Using (4.22) and the steps shown in Section 4.3, we can reach a formula which is analogous to (4.33) but for $\boldsymbol{r}_i \in \mathcal{R}_1$ and $\boldsymbol{r}_j \in \mathcal{R}_2$ as illustrated in Figure 4.1 given by

$$\mathrm{g}_3(z) = \frac{1}{S}\frac{1}{4\pi z^2 dz}\sum_{s}^{S}\frac{1}{\mathfrak{n}J_1}\sum_{r_i\in\mathcal{X}^s\cap\mathcal{R}_1}\#\mathcal{X}_i^s(z), \quad \text{(3D isotropic)}, \tag{4.37}$$

where we substituted (4.25) and used $J_1 = \#[\mathcal{X}^s \cap \mathcal{R}_1]$. Equation (4.37) is the same as the formula [3, Equation (2)], and [54, Equation (8.3.8)] when specialising their formula for particles with the same radius, and when taking $\mathcal{R}_1 = \mathcal{R}_2$.

For two spatial dimensions the pair-correlation becomes

$$\mathrm{g}_2(z) = \frac{1}{S}\frac{1}{2\pi z dz}\sum_{s}^{S}\frac{1}{\mathfrak{n}J_1}\sum_{r_i\in\mathcal{X}^s\cap\mathcal{R}_1}\#\mathcal{X}_i^s(z), \quad \text{(2D isotropic)}. \tag{4.38}$$

As a final check, note that if particle positions were uncorrelated then $\#\mathcal{X}_i^s(z) \approx 4\pi\mathfrak{n}z^2\mathrm{d}z$, for three spatial dimensions, because the number of particles would then be proportional to the volume times the number density. Substituting this approximation into (4.37) leads to $\mathrm{g}_3(z) = 1$, which is what is expected from uncorrelated particles.

4.5 The Structure Factor

The structure factor, known as $\mathrm{S}(k)$, plays a crucial role in material science and condensed matter physics [29, 30, 41, 42, 48]. Many experimental techniques, such as X-ray diffraction, neutron scattering and electron microscopy, inherently measure the structure factor, providing a deep understanding of the arrangement and density fluctuations of particles within a material [5, 31, 49]. Unlike the pair-correlation function $\mathrm{g}(r)$ which gives the probability of finding particle pairs at a certain distance, the structure factor captures the intensity of scattered waves from materials, revealing both local and long-range order through its relationship as the Fourier transform of

$\mathrm{g}(r)$ [10, 24, 55]. This makes the structure factor, $\mathrm{S}(k)$, an integral part of interpreting experimental data, providing information for both characterising new materials and designing them with specific properties.

The expressions for the structure factor in two and three dimensions are well-established in the field of material science [39, 51, 55]. In this section we re-derive the structure factor from first principles using (4.26) and (4.27).

Mathematically, the pair-correlation $\mathrm{g}(z)$ in the form (4.26) shows how $\mathrm{g}(z)$ is a discontinuous function when calculated from a finite number of particles. It is discontinuous in the variables z and the position of the particles $\boldsymbol{r}_i$. As $\mathrm{g}(z)$ is not a smooth function, we can not use techniques from local nonlinear optimisation to calculate a particle configuration to match a specific pair-correlation. To avoid this, we can take a transform of the pair-correlation such as the structure factor:

$$\mathrm{S}(k) = 1 + \mathfrak{n} \int (\mathrm{g}(r) - 1)\mathrm{e}^{-\mathrm{i}\boldsymbol{k}\cdot\boldsymbol{r}}\mathrm{d}\boldsymbol{r}, \quad \text{(The Structure factor)}, \tag{4.39}$$

where $r = |\boldsymbol{r}|$ and $k = |\boldsymbol{k}|$ is the magnitude of the wave vector. Equation (4.39) matches the typical definition of the structure factor [51, 54, 56], noting that the notation $h(r) = \mathrm{g}(r) - 1$ is commonly used.

For some of the following calculations, we will perform the integral over $\mathrm{g}(r)$ and -1 separately. To do this we note that:

$$\delta(\boldsymbol{k}) = \frac{1}{(2\pi)^n} \int \mathrm{e}^{-\mathrm{i}\boldsymbol{k}\cdot\boldsymbol{r}}\mathrm{d}\boldsymbol{r}, \tag{4.40}$$

where n is the spatial dimension, which in this paper is either $n = 3$ or $n = 2$.

For any given isotropic pair-correlation $\mathrm{g}(r)$ the structure factor (4.39) can be simplified to a 1D integral. To do this, we assume that particles become uncorrelated at a distance of R so that $\mathrm{g}(r) = 1$ for $0 \leq r \leq R$. Then from (4.39) we can calculate that for three spatial dimensions:

$$\mathrm{S}_3(k) = 1 + \frac{4\pi}{k}\mathfrak{n} \int_0^R (\mathrm{g}_3(r) - 1)\sin(kr)r\mathrm{d}r, \tag{4.41}$$

and for two spatial dimensions:

$$\mathrm{S}_2(k) = 1 + 2\pi\mathfrak{n} \int_0^R (\mathrm{g}_2(r) - 1)\mathrm{J}_0(kr)r\mathrm{d}r. \tag{4.42}$$

We will use (4.42) to calculate the structure factor from a target pair-correlation in

the next section.

We can further simplify the structure factor when calculating it from a configuration of particles. For three spatial dimensions, we can substitute (4.26) into the structure factor (4.41), but with $R = \infty$, and using the property of the Dirac delta, to obtain:

$$\mathrm{S}_3(k) = 1 + \frac{1}{S}\sum_{s}^{S}\frac{1}{J_1}\sum_{\boldsymbol{r}_i\in\mathcal{X}^s\cap\mathcal{R}_1}\sum_{\substack{\boldsymbol{r}_j\in\mathcal{X}^s\\ \boldsymbol{r}_j\neq\boldsymbol{r}_i}}\frac{\sin(k|\boldsymbol{r}_i-\boldsymbol{r}_j|)}{k|\boldsymbol{r}_i-\boldsymbol{r}_j|}, \quad \text{(3D Structure factor)}, \quad (4.43)$$

for $k > 0$. When calculating (4.43), a term of the form $-(2\pi)^3\mathrm{n}\delta(\boldsymbol{k})$ appears, according to (4.40), however, as we consider only $k > 0$ it has no contribution to the above.

Following analogous steps, the two dimensional structure factor calculated from (4.27) becomes:

$$\mathrm{S}_2(k) = 1 + \frac{1}{SJ_1}\sum_{s}^{S}\sum_{\boldsymbol{r}_i\in\mathcal{X}^s\cap\mathcal{R}_1}\sum_{\substack{\boldsymbol{r}_j\in\mathcal{X}^s\\ \boldsymbol{r}_j\neq\boldsymbol{r}_i}}\mathrm{J}_0(|k||\boldsymbol{r}_i-\boldsymbol{r}_j|), \quad \text{(2D Structure factor)}, \quad (4.44)$$

for $k > 0$, where J_0 is the Bessel function of the first kind.

4.6 Particle configurations from the structure factor

In theory, the pair-correlation is calculated by taking into account an infinite number of different particle configurations. Yet, many exotic material properties can be achieved by choosing specific pair-correlations, with one example being hyperuniform disordered materials [51, 52, 59]. So being able to calculate one configuration of particles which closely represents any given pair-correlation would provide a route to fabricate particulate materials which exhibit exotic properties.

To recover a specific configuration of particles from a pair-correlation, we show a method to find a configuration of particles which is the mean particle configuration. Suppose we are given some pair-correlation $\mathrm{g}^\star(z)$, then we want one configuration of particles that when substituted into (4.37) will be close to $\mathrm{g}^\star(z)$, when removing the sum over the ensembles by setting $S = 1$.

4.6.1 Restrictions

For any given pair-correlation g and S structure factor there are certain restrictions [10, 55, 57] that need to be satisfied. These need to be considered when choosing a

target pair-correlation $\mathrm{g}^\star$ or structure factor $\mathrm{S}^\star$. We will only consider a few of these restrictions, and note that there may be an infinite number of necessary, though more complicated, conditions on the pair-correlation [10].

The simplest restrictions are that:

$$\mathrm{g}^\star(r) \geq 0 \quad \text{and} \quad \mathrm{S}^\star(k) \geq 0, \tag{4.45}$$

where the first is due to the definition (4.21) together with the basic rule that probability functions must be positive. The second needs to be non-negative because of the relation of the structure factor $\mathrm{S}(k)$ with the variance of the particle density. This is discussed in [10, 48, 55, 57].

As we focus on disordered particulates we require that particles become uncorrelated at some distance R. This requirement implies that:

$$\mathrm{g}^\star(r) = 1, \qquad \text{for every } \; r \geq R. \tag{4.46}$$

Further, from the definition (4.21), together with (4.22), we have that:

$$\begin{aligned}\int_{\mathcal{R}_2}\int_{\mathcal{R}_1} \mathrm{g}(\boldsymbol{x}_1,\boldsymbol{x}_2)\mathrm{d}\boldsymbol{x}_1\mathrm{d}\boldsymbol{x}_2 &= \frac{J_2-1}{J_2}|\mathcal{R}_1||\mathcal{R}_2| \int_{\mathcal{R}_1}\int_{\mathcal{R}_2} \mathrm{p}(\boldsymbol{x}_1,\boldsymbol{x}_2)\mathrm{d}\boldsymbol{x}_1\mathrm{d}\boldsymbol{x}_2 \\ &= \frac{J_2-1}{J_2}|\mathcal{R}_1||\mathcal{R}_2|. \end{aligned} \tag{4.47}$$

Alternatively, using isotropy so that g depends on only $|\boldsymbol{x}_1-\boldsymbol{x}_2|$, the condition (4.46), and specialising to three spatial dimensions, we make use of (4.26) to obtain:

$$\begin{aligned}\int_{\mathcal{R}_2}\int_{\mathcal{R}_1} (\mathrm{g}_3(|\boldsymbol{x}_1-\boldsymbol{x}_2|)-1)\mathrm{d}\boldsymbol{x}_1\mathrm{d}\boldsymbol{x}_2 &= \int\int_0^R \int_{\mathcal{R}_1} (\mathrm{g}_3(z)-1)\mathrm{d}\boldsymbol{x}_1 z^2\mathrm{d}z\mathrm{d}\Omega \\ &= 4\pi|\mathcal{R}_1|\int_0^R (\mathrm{g}_3(z)-1)z^2\mathrm{d}z. \end{aligned} \tag{4.48}$$

In (4.48), the integral over the regions $\mathcal{R}_1$ and $\mathcal{R}_2$ are simplified to a radial integral over distance z with an angular component represented by Ω, the solid angle. The solid angle Ω is crucial for integrating over all directions in three-dimensional space, accounting for the isotropy condition (4.46). By changing variables to $\boldsymbol{z} = \boldsymbol{x}_2 - \boldsymbol{x}_1$, we further simplify the expression, resulting in the integral over z and Ω that accounts for the entire spherical symmetry around a point. Combining (4.47) and (4.48) leads to the restriction:

$$\int_0^R \mathrm{g}_3(z)z^2\mathrm{d}z = \frac{R^3}{3} - \frac{1}{4\pi\mathfrak{n}}, \tag{4.49}$$

where we used $\mathfrak{n} = J_2/|\mathcal{R}_2|$. For two spatial dimensions, following analogous steps and using (4.27), we obtain the restriction:

$$\int_0^R \mathrm{g}_2(z) z \mathrm{d}z = \frac{R^2}{2} - \frac{1}{2\pi\mathfrak{n}}. \tag{4.50}$$

We can also translate the pair-correlation to satisfy (4.50). Let:

$$\mathrm{g}_2(r) = \mathrm{g}_2^0(r) + \mathfrak{a}\, dp(r), \tag{4.51}$$

where $dp(r) \to 0$ when $r \to R$. In simple terms, (4.51) modifies an initial pair-correlation function $\mathrm{g}_2^0(r)$ to include a perturbation, aiming to adjust the particle distribution within a specific range. The perturbation $dp(r)$ is designed to become negligible as the distance r reaches a specific point R. Then, given a number density $\mathfrak{n}$ we can obtain dp from (4.50):

$$\mathfrak{a} = \Big[\frac{R^2}{2} - \frac{1}{2\pi\mathfrak{n}} - \int_0^R \mathrm{g}_2(z) z \mathrm{d}z\Big]\Big[\int_0^R dp(z) z \mathrm{d}z\Big]^{-1}. \tag{4.52}$$

The selection of $dp(r) = \mathrm{e}^{-6r/R}$ guarantees this vanishing effect, exponentially decreasing as r increases. The equation for $\mathfrak{a}$ calculates the necessary scaling factor to achieve the desired distribution pattern, factoring in the number density of particles and the integral of the pair-correlation function up to R.

4.6.2 Gradient optimisation

For some inner product:

$$\langle \mathcal{G}, \mathcal{H} \rangle_k = \int \mathcal{G}(k)\mathcal{H}(k) w(k) \mathrm{d}k,$$

where $w(k)$ is some known weight. The objective is to find a particle configuration $\mathcal{X}$ that minimises:

$$\min_{\boldsymbol{r}_i \in \mathcal{X}} f(\mathcal{X}), \quad \text{where} \quad f(\mathcal{X}) := \langle \mathrm{S} - \mathrm{S}^\star, \mathrm{S} - \mathrm{S}^\star \rangle_k. \tag{4.53}$$

Equation (4.53) uses an integral to assess the similarity between the actual and target structure factors, S and $\mathrm{S}^\star$ respectively, over a range of spatial frequencies k. This method helps to quantify how much the particle configuration $\mathcal{X}$ deviates from the desired configuration.

Most methods in the literature [28, 43] achieve this by using non-gradient-based methods such as Genetic Algorithms, Nelder-Mead, and Simulated Annealing. However, f, as written above, is a smooth function of the position of the particles in $\mathcal{X}$. Further, it is straightforward to analytically calculate the gradient of f in terms of the particle positions $\boldsymbol{r}_j$. This implies the gradient based methods [45] hold significant potential for superior performance over traditional non-gradient-based approaches. In specific, the objective function f, and its gradient, can be computational expensive to calculate so we opt to use the Limited memory BFGS (L-BFGS) methods [27, 33], as it stores information on the Hessian (the gradient of the gradient) and uses this to accelerate convergence. This often implies that L-BFGS requires less evaluations of the objective function and its gradient [27].

Specifically, we develop a method to minimise (4.53) in two steps, one global, and one local. Separating the two steps allows us to search over a large area of the parameter space with the global step, while still obtaining high precision with the local step. Another clear reason, based on recovering a configuration of particles, is that if we had the constraint of particles not overlapping, then it can lead to particles being locked in configurations which can be far from the global minimum. For this reason we only enforce no particle overlapping in the local step. In more detail the two steps are:

- **The global step.** A global optimisation that completely rearranges all particles to minimise (4.53). For this step, we will allow particles to overlap, helping us explore a broad range of particle configurations and avoid locking the particles in a configuration and we will use a limited range for the wavenumbers $k_1 \leq k \leq k_2$ when minimising (4.53). That is, in this step we do not want to resolve spatial details smaller than the length scale $2a$, since it might not significantly influence the properties of the material. So the shortest wavelength λ we consider for the structure factor is $\lambda = 2a$ which corresponds to wavenumbers $k \leq k_2 = \pi/a$. The smallest wavenumber k_1 is determined by the dimensions of the material: let D_1 be the smallest dimension of $\mathcal{R}_1$, then the longest wavelength we consider is $\lambda = D_1$ which implies that $k \geq k_1 = 2\pi/D_1$.
- **The local step.** This step improves the particle configurations obtained from the global step. This involves making small adjustments to the particle positions to achieve a more accurate and realistic distribution of particles. We also enforce a penaliser W, shown in (4.60), to prevent overlaps between particles. The penaliser has the form of an exponential that increases very rapidly as the distance decreases. This means that as particles get closer to each other, the

penalty for their overlap increases exponentially. For this step we also want to resolve spatial details. Suppose we want to resolve details up to $a/4$, then $k_2 = 8\pi$ and $k_1 \leq k \leq k_2$ for this step.

To use techniques from nonlinear optimisation [33, 45] to minimise calculate (4.53) we need to calculate the gradient:

$$\frac{\partial f(\mathcal{X})}{\partial \boldsymbol{r}_j} = \frac{\partial}{\partial \boldsymbol{r}_j}\langle \mathrm{S} - \mathrm{S}^\star, \mathrm{S} - \mathrm{S}^\star\rangle_k = 2\sum_i \langle \frac{\partial \mathrm{S}}{\partial R_{ij}}, \mathrm{S} - \mathrm{S}^\star\rangle_k \frac{\partial R_{ji}}{\partial \boldsymbol{r}_j} \tag{4.54}$$

$$= 2\langle \sum_i \frac{\partial \mathrm{S}}{\partial R_{ji}} \frac{\boldsymbol{R}_{ji}}{R_{ji}}, \mathrm{S} - \mathrm{S}^\star\rangle_k, \tag{4.55}$$

where

$$\begin{cases} \boldsymbol{R}_{ji} = \boldsymbol{r}_j - \boldsymbol{r}_i, & \text{the vector from } \boldsymbol{r}_i \text{ to } \boldsymbol{r}_j, \\ R_{ji} = |\boldsymbol{r}_j - \boldsymbol{r}_i|, & \text{the magnitude of } \boldsymbol{R}_{ji}, \\ \dfrac{\partial R_{ji}}{\partial \boldsymbol{r}_j} = \dfrac{\boldsymbol{R}_{ji}}{R_{ji}}, & \text{the gradient of } R_{ji} \text{ with respect to } \boldsymbol{r}_j. \end{cases} \tag{4.56}$$

In particular, for (4.44) we have:

$$\frac{\partial \mathrm{S}_2}{\partial R_{ji}} = \frac{k}{J_1} \begin{cases} \mathrm{J}_0'(|k|R_{ji}), & \text{if} \quad \boldsymbol{r}_j \notin \mathcal{R}_1, \\ 2\mathrm{J}_0'(|k|R_{ji}), & \text{if} \quad \boldsymbol{r}_j \in \mathcal{R}_1, \end{cases} \tag{4.57}$$

where there are two cases because: if $\boldsymbol{r}_j \in \mathcal{R}_1$ then $\mathrm{J}_0(kR_{ji})$ gets summed twice in (4.44), but if $\boldsymbol{r}_j \notin \mathcal{R}_1$ then $\mathrm{J}_0(kR_{ij})$ only appears once in the summation. Likewise for (4.43) we have:

$$\frac{\partial \mathrm{S}_3}{\partial R_{ji}} = \frac{k}{J_1}\frac{1}{(kR_{ij})^2} \begin{cases} kR_{ij}\cos(kR_{ij}) - \sin(kR_{ij}), & \text{if} \quad \boldsymbol{r}_j \notin \mathcal{R}_1, \\ 2kR_{ij}\cos(kR_{ij}) - 2\sin(kR_{ij}), & \text{if} \quad \boldsymbol{r}_j \in \mathcal{R}_1. \end{cases} \tag{4.58}$$

For most optimisation methods, we choose to use Optim.jl [33], we need to supply the total gradient:

$$\nabla f = \left[\frac{\partial f(\mathcal{X})}{\partial \boldsymbol{r}_1}, \frac{\partial f(\mathcal{X})}{\partial \boldsymbol{r}_2}, \ldots, \frac{\partial f(\mathcal{X})}{\partial \boldsymbol{r}_j}\right],$$

where the block vector on the right is typically flattened to be just one large vector. For the local step, after the global step is complete, we add a restriction that penalises particles that are overlapping. That is instead of minimising (4.53), we minimise:

$$\min_{\boldsymbol{r}_i \in \mathcal{X}} f(\mathcal{X}) + AW(\mathcal{X}), \tag{4.59}$$

where A is some large positive constant that is problem dependant and:

$$W = \sum_{i,j\neq i} \chi_{\{R_{ji}<2a\}} \mathrm{e}^{-4R_{ji}^2/(2a)^2}. \tag{4.60}$$

The specific formula for the penaliser (4.60) has the form of a Gaussian distribution [21] and was chosen to effectively prevent particle overlaps during the local optimisation step. This function is smooth and differentiable, and it rapidly increases the penalty as the distance between particles becomes less than twice their radius. Having said that, the gradient of the penaliser (4.60) with respect to the position of the j-th particle has the following form:

$$\frac{\partial W}{\partial \boldsymbol{r}_j} = -\frac{4}{a^2} \sum_{i\neq j} \chi_{\{R_{ji}<2a\}} \mathrm{e}^{-4R_{ji}^2/(2a)^2} \boldsymbol{R}_{ji}. \tag{4.61}$$

For ease of implementation we use a discrete form:

$$\langle \mathcal{G}, \mathcal{H} \rangle_k = \sum_q \mathcal{G}_q \mathcal{H}_q w_q,$$

where w_q are some Gaussian quadrature weights. For example we can write:

$$\frac{\partial f(\mathcal{X})}{\partial \boldsymbol{r}_j} = 2 \sum_{iq} \frac{\partial \mathrm{S}_q}{\partial R_{ji}} \frac{\boldsymbol{R}_{ji}}{R_{ji}} (\mathrm{S}_q - \mathrm{S}_q^\star) w_q. \tag{4.62}$$

The discrete form (4.62) simplifies the calculation of gradients in computational simulations. This technique allows for efficient numerical approximation of gradients necessary for optimising particle positions based on the difference between observed and desired structural properties.

4.6.3 Preliminary numerical results

In this section we share our preliminary results and discuss potential future developments with our method.

Selection of pair-correlation. The first step is to have a systematic way to choose candidate pair-correlations, with one motivation being to control wave propagation [15]. Our work begins with the selection of appropriate pair-correlations that satisfy the restrictions given in Section 4.6.1. Our choice is the Percus-Yevick model, a well-studied pair-correlation [1, 23, 51, 54] which represents disordered particles with very short range correlation. This model effectively catches the behaviour of

uniformly distributed particles that exhibit correlations only because they can not overlap. Figure 4.2 illustrates this concept, displaying the pair-correlation for hard discs in a two-dimensional setup, where these discs account for a 15% volume fraction and each particle has a radius of $a = 1$. This figure also includes the corresponding structure factor, highlighting how the spatial arrangement of particles influences wave propagation through the material.

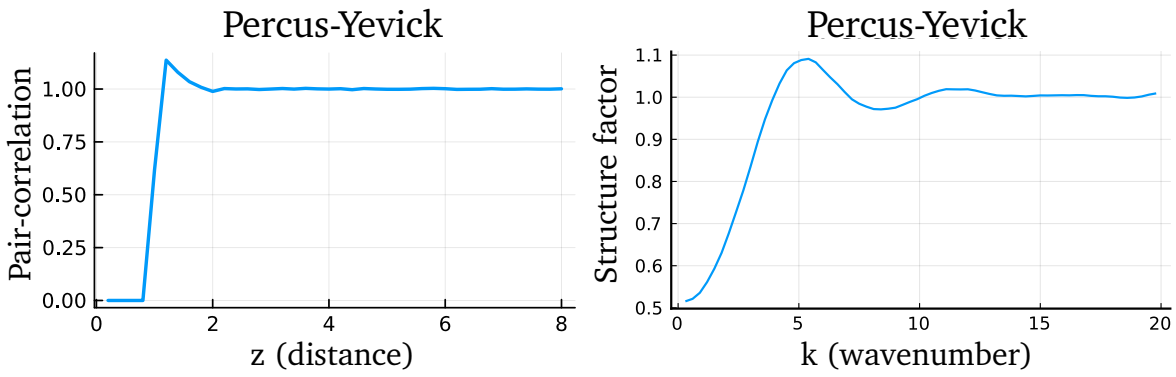

Figure 4.2: On the left, the Percus-Yevick pair-correlation for hard discs [1], in two spatial dimensions, where the discs occupy 15% of the volume fraction. On the right the corresponding structure factor when using (4.42).

Initial configuration. The next step is to generate an initial configuration of particles with the correct sizes, and within a given volume fraction [54], as shown in Figure 4.3a. The simplest way to do this is to place particles on a grid. This also facilitates defining the regions $\mathcal{R}_1$ and $\mathcal{R}_2$ which are needed to calculate the pair-correlation without introducing artefacts from the boundary, as discussed in Section 4.3. However, placing particles exactly in a periodic grid would lead to a set of problems, especially when it comes to finding the optimal arrangement using gradient-based optimisation techniques. The symmetrical nature of the periodic grid tends to position the configuration at a local maximum which may not be an ideal starting position for gradient-based methods. In other words, this symmetry can trick our optimisation methods into thinking they have found the best arrangement when there might be better choices they have not explored yet. To avoid this, we introduce a simple yet effective strategy: we slightly move each particle by a small distance in a random direction to break the symmetry, creating a more favourable setting for optimisation.

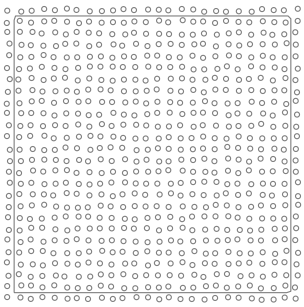

(a) Initial particle configuration.

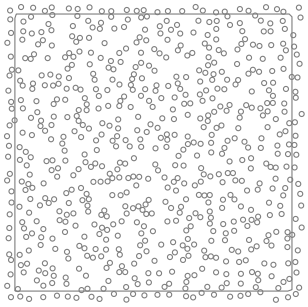

(b) Predicted particle configuration.

Figure 4.3: Figure 4.3a presents the initial position of all the particles, while Figure 4.3b demonstrates the optimised particle configuration that closely aligns with the structure factor depicted in Figure 4.2, achieved through our optimisation method.

Optimisation method and results. Our optimisation method is executed in two steps: The first step of our method, the global step, minimises the objective function (4.53) and is able to exactly match the specified structure factor, as demonstrated in Figure 4.2. Following this global step, we employ a local optimisation step to refine the particle configuration further. The result of the structure factor of the optimised particle configuration, after the local step, is displayed in Figure 4.4. Despite the slight noise introduced by the finite number of particles (600 particles of radius $a = 1$ occupying a 15% volume fraction in two spatial dimensions), the predicted structure factor matches the target structure factor. Moreover, the predicted pair-correlation, shown in Figure 4.4, offers further insight. Although there is some noise due to the small number of particles, we see a good match with the desired pair-correlation.

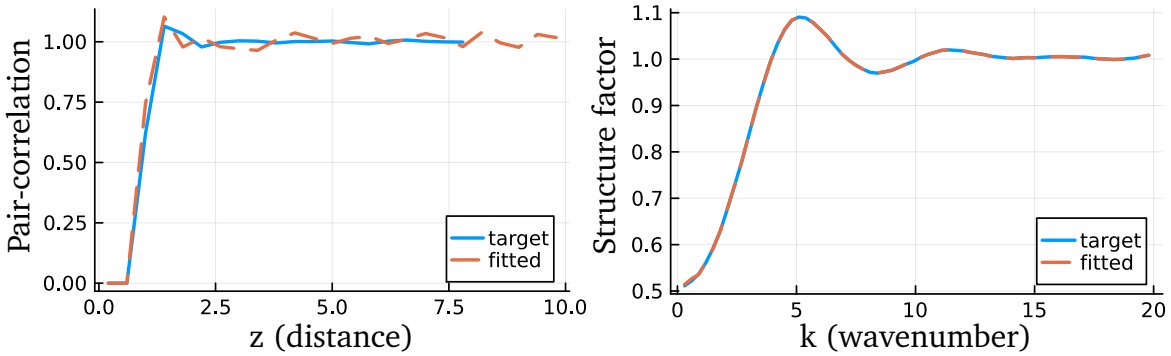

Figure 4.4: The optimised particle configuration consisting of 600 particles of radius $a = 1$ occupying 15% of the particulate, depicted in Figure 4.3b, closely aligns with the desired structure factor and pair-correlation, despite noise introduced by the limited number of particles.

4.7 Conclusions

In this paper, we deduced from first principles how to calculate both the pair-correlation and structure factor of a finite disordered particulate. We demonstrated how to do this without getting artefacts from the boundary of the particulate, something which seems to be ignored in the literature. Thus, it was possible to calculate the pair-correlation of an infinite particulate from a finite sample. This is generally desired, as most theoretical methods use the pair-correlations from an infinite medium, including the very important translation invariance which greatly simplifies the pair-correlation.

Being able to calculate the pair-correlation from a particulate was rather straightforward in comparison to the inverse: calculating a particulate from a pair-correlation. We presented a method to calculate one configuration of particles that best fitted a given pair-correlation or structure factor.

Most methods in the literature [20, 45, 55] that calculate particle configurations from the pair-correlation of structure factor use non-gradient-based methods such as Genetic Algorithms, Nelder-Mead, and Simulated Annealing. Several works in fact focus on trying to approximate the pair-correlation with a particulate, which is an inherently discontinuous function as the joint probability function (4.8) involves Dirac deltas. Instead, we suggested that it is best to seek a configuration of particles to approximate the structure factor, as it is a smooth function of the particle positions, as shown by (4.43) and (4.44). This enabled us to analytically calculate the gradient of the structure factor, in terms of the particle positions, leading to faster convergence to optimal configurations. The efficacy of our method was evidenced through visual representations in Figure 4.3, which showed the transformation from the initial to the optimised particle configurations, matching the theoretical model. Furthermore, the comparison of the structure factors before and after optimisation, as depicted in Figure 4.4, underscored the precision of our approach, achieving an almost identical match to the targeted structure factor.

Optimising particle configurations holds significant implications for a wide range of engineering applications. By precisely controlling particle configurations, engineers can tailor material properties for diverse applications in aerospace, automotive, and structural engineering, ensuring optimal performance and reliability.

Future avenues. We presented a two step method to calculate the structure factor from a configuration of particles, one step for global optimisation that avoids particle locking, and one step for local optimisation. To have clear evidence about the performance advantage of our method, it is essential to further validate and

compare our method against traditional brute-force, non-gradient-based optimisation techniques, such as Genetic Algorithms and Simulated Annealing. This method can be further developed to easily add priors about the particle configuration and treat this as a statistical inverse problem [21]. There is a significant amount of prior information that could be used [36, 58]. For example, when using more than one type of particle, some particles may repel or attract each other. Or there can be specific knowledge on chains or sub-components of particles. This information can be added as a prior, or regulariser. This seems to be an unexplored approach that could greatly increase the performance of this inverse problem. Moreover, the preliminary results presented in Section 4.6.3, not only validate our novel approach to determining particle configurations from structure factors, but also open up new possibilities for future research. By fine-tuning the particle configurations, we could explore a wider range of pair-correlations and structure factors, potentially uncovering new ways to manipulate wave propagation in disordered particulate materials.

Author contributions

AK conceived of the study, drafted the manuscript, wrote all the code for the numerical calculations, developed the theoretical calculations, and produced all the figures. ALG helped conceive the study, edited the manuscript, assisted with and verified the theoretical calculations.

Data and reproducibility

To produce our results we used the open source software [17], [18] and [34].

References

[1] M. Adda-Bedia et al. ‘Solution of the Percus-Yevick equation for hard disks’. In: *The Journal of Chemical Physics* 128.18 (May 2008). URL: http://dx.doi.org/10.1063/1.2919123.

[2] George B Arfken et al. *Mathematical methods for physicists: a comprehensive guide*. Academic press, 2011.

[3] J.A. Barker et al. ‘Monte Carlo values for the radial distribution function of a system of fluid hard spheres’. In: *Molecular Physics* 21.1 (Jan. 1971), 187–191. URL: http://dx.doi.org/10.1080/00268977100101331.

[4] V.V. Bringi et al. ‘The effects on pair correlation function of coherent wave attenuation in discrete random media’. In: *IEEE Transactions on Antennas and Propagation* 30.4 (July 1982), pp. 805–808. URL: https://doi.org/10.1109/tap.1982.1142852.

[5] O. L. Caballero et al. ‘Molecular Dynamics Simulations for Neutrino Scattering in Heterogeneous High Dense Media’. In: (2008). URL: https://doi.org/10.1063/1.2905137.

[6] Rémi Carminati et al. *Principles of Scattering and Transport of Light*. Cambridge University Press, June 2021. URL: https://doi.org/10.1017/9781316544693.

[7] F. Carsughi et al. ‘Small-angle neutron scattering from silica particles in solution with different concentrations’. In: *Physica B: Condensed Matter* 234-236 (June 1997), pp. 343–346. URL: https://doi.org/10.1016/s0921-4526(97)00980-0.

[8] F. S. Carvalho et al. ‘Radial distribution function for liquid gallium from experimental structure factor: a Hopfield neural network approach’. In: *Journal of Molecular Modeling* 26.8 (July 2020). URL: https://doi.org/10.1007/s00894-020-04436-y.

[9] L Cormier et al. ‘A reverse Monte Carlo study of a titanosilicate glass’. In: *Journal of Physics: Condensed Matter* 9.46 (Nov. 1997), pp. 10129–10136. URL: https://doi.org/10.1088/0953-8984/9/46/011.

[10] O. Costin et al. ‘On the Construction of Particle Distributions with Specified Single and Pair Densities’. In: *The Journal of Physical Chemistry B* 108.51 (Oct. 2004), pp. 19614–19618. URL: https://doi.org/10.1021/jp047793m.

[11] Jenness Crawford et al. 'Aspects of correlation function realizability'. In: *The Journal of Chemical Physics* 119.14 (Sept. 2003), pp. 7065–7074. URL: https://doi.org/10.1063/1.1606678.

[12] Debdas Dhabal et al. 'Probing the triplet correlation function in liquid water by experiments and molecular simulations'. In: *Physical Chemistry Chemical Physics* 19.4 (2017), pp. 3265–3278. URL: https://doi.org/10.1039/c6cp07599a.

[13] M. Fábián et al. 'Network structure of multi-component sodium borosilicate glasses by neutron diffraction'. In: *Journal of Non-Crystalline Solids* 353.18-21 (June 2007), pp. 2084–2089. URL: https://doi.org/10.1016/j.jnoncrysol.2007.02.030.

[14] Hiroyuki Fujii et al. 'Structural properties of liquid Au–Si and Au–Ge alloys with deep eutectic region'. In: *Journal of Non-Crystalline Solids* 353.18-21 (June 2007), pp. 2094–2098. URL: https://doi.org/10.1016/j.jnoncrysol.2007.02.031.

[15] Artur L Gower et al. 'Effective waves for random three-dimensional particulate materials'. In: *New Journal of Physics* 23.6 (June 2021), p. 063083. URL: http://dx.doi.org/10.1088/1367-2630/abdfee.

[16] Artur L. Gower et al. 'Multiple Waves Propagate in Random Particulate Materials'. In: *SIAM Journal on Applied Mathematics* 79.6 (Jan. 2019), 2569–2592. URL: http://dx.doi.org/10.1137/18M122306X.

[17] Artur L Gower et al. 'MultipleScatering.jl: A Julia library for simulating, processing, and plotting multiple scattering of waves.' In: *github.com/JuliaWaveScattering/MultipleScattering.jl* (2020).

[18] Artur L Gower et al. 'ParticleCorrelations.jl: A package to calculate typical pair correlations (or structure factor) for disordered particulates, such as Percus-Yevick, and to calculate specific particle configurations from given pair correlation.' In: *github.com/arturgower/ParticleCorrelations.jl* (2023).

[19] C. J. Horowitz et al. 'Neutrino pasta scattering: The opacity of nonuniform neutron-rich matter'. In: *Physical Review C* 69.4 (Apr. 2004). URL: https://doi.org/10.1103/physrevc.69.045804.

[20] C. J. Horowitz et al. 'Nonuniform neutron-rich matter and coherent neutrino scattering'. In: *Physical Review C* 70.6 (Dec. 2004). URL: https://doi.org/10.1103/physrevc.70.065806.

[21] Jari P. Kaipio et al. *Statistical and Computational Inverse Problems*. Springer New York, 2005. URL: http://dx.doi.org/10.1007/b138659.

[22] D. A. Keen et al. 'Structural modelling of glasses using reverse Monte Carlo simulation'. In: *Nature* 344.6265 (Mar. 1990), pp. 423–425. URL: https://doi.org/10.1038/344423a0.

[23] Gerhard Kristensson et al. *Multiple scattering by a collection of randomly located obstacles Part IV: The effect of the pair correlation function*. English. Vol. TEAT-7272. Technical Report LUTEDX/(TEAT-7272)/1-23/(2021). 2021. URL: https://portal.research.lu.se/en/publications/multiple-scattering-by-a-collection-of-randomly-located-obstacles-8.

[24] T. Kuna et al. 'Realizability of Point Processes'. In: *Journal of Statistical Physics* 129.3 (Sept. 2007), pp. 417–439. URL: https://doi.org/10.1007/s10955-007-9393-y.

[25] Tobias Kuna et al. 'Necessary and sufficient conditions for realizability of point processes'. In: *The Annals of Applied Probability* 21.4 (Aug. 2011). URL: https://doi.org/10.1214/10-aap703.

[26] O. Leseur et al. 'High-density hyperuniform materials can be transparent'. In: *Optica* 3.7 (July 2016), p. 763. URL: http://dx.doi.org/10.1364/OPTICA.3.000763.

[27] Dong C Liu et al. 'On the limited memory BFGS method for large scale optimization'. In: *Mathematical programming* 45.1-3 (1989), pp. 503–528.

[28] C. Manwart et al. 'Reconstruction of random media using Monte Carlo methods'. In: *Physical Review E* 59.5 (May 1999), pp. 5596–5599. URL: https://doi.org/10.1103/physreve.59.5596.

[29] R L McGreevy. 'Reverse Monte Carlo modelling'. In: *Journal of Physics: Condensed Matter* 13.46 (Nov. 2001), R877–R913. URL: https://doi.org/10.1088/0953-8984/13/46/201.

[30] R. L. McGreevy et al. 'Reverse Monte Carlo Simulation: A New Technique for the Determination of Disordered Structures'. In: *Molecular Simulation* 1.6 (Dec. 1988), pp. 359–367. URL: https://doi.org/10.1080/08927028808080958.

[31] M. Micoulaut et al. 'Structural properties of chalcogenide glasses and the isocoordination rule: Disentangling effects from chemistry and network topology'. In: *Physical Review B* 106.1 (July 2022). URL: http://dx.doi.org/10.1103/PhysRevB.106.014206.

[32] Milan M. Milošević et al. 'Hyperuniform disordered waveguides and devices for near infrared silicon photonics'. In: *Scientific Reports* 9.1 (Dec. 2019). URL: http://dx.doi.org/10.1038/s41598-019-56692-5.

[33] Patrick K. Mogensen et al. 'Optim: A mathematical optimization package for Julia'. In: *Journal of Open Source Software* 3.24 (2018), p. 615. URL: https://doi.org/10.21105/joss.00615.

[34] Patrick Kofod Mogensen et al. 'Optim: A mathematical optimization package for Julia'. In: *Journal of Open Source Software* 3.24 (2018), p. 615.

[35] Rana Nandi et al. 'Transport Properties of the Nuclear Pasta Phase with Quantum Molecular Dynamics'. In: *The Astrophysical Journal* 852.2 (Jan. 2018), p. 135. URL: https://doi.org/10.3847/1538-4357/aa9f12.

[36] Edoardo Patelli et al. 'On optimization techniques to reconstruct microstructures of random heterogeneous media'. In: *Computational Materials Science* 45.2 (Apr. 2009), pp. 536–549. URL: https://doi.org/10.1016/j.commatsci.2008.11.019.

[37] R.K. Pathria et al. *Statistical Mechanics of Interacting Systems: The Method of Cluster Expansions*. Elsevier, 2011, pp. 299–343. URL: https://doi.org/10.1016/b978-0-12-382188-1.00010-4.

[38] Oliver H. E. Philcox et al. 'Disordered Heterogeneous Universe: Galaxy Distribution and Clustering across Length Scales'. In: *Physical Review X* 13.1 (Mar. 2023). URL: https://doi.org/10.1103/physrevx.13.011038.

[39] J. Piekarewicz et al. 'Proton fraction in the inner neutron-star crust'. In: *Physical Review C* 85.1 (Jan. 2012). URL: https://doi.org/10.1103/physrevc.85.015807.

[40] Szilvia Pothoczki et al. 'Partial radial distribution functions of methylene halide molecular liquids'. In: *Journal of Molecular Liquids* 153.2-3 (May 2010), pp. 112–116. URL: https://doi.org/10.1016/j.molliq.2010.01.011.

[41] L. Pusztai et al. 'MCGR: An inverse method for deriving the pair correlation function from the structure factor'. In: *Physica B: Condensed Matter* 234-236 (June 1997), pp. 357–358. URL: https://doi.org/10.1016/s0921-4526(96)00986-6.

[42] L. Pusztai et al. 'Reverse Monte Carlo model calculations on a-C:H two-component systems'. In: *Zeitschrift für Physik B Condensed Matter* 101.4 (Dec. 1996), pp. 631–636. URL: https://doi.org/10.1007/s002570050256.

[43] Jacques A. Quiblier. 'A new three-dimensional modeling technique for studying porous media'. In: *Journal of Colloid and Interface Science* 98.1 (Mar. 1984), pp. 84–102. URL: https://doi.org/10.1016/0021-9797(84)90481-8.

[44] V. Romero-García et al. 'Wave transport in 1D stealthy hyperuniform phononic materials made of non-resonant and resonant scatterers'. In: *APL Materials* 9.10 (Oct. 2021). URL: http://dx.doi.org/10.1063/5.0059928.

[45] Andrzej Ruszczynski. *Nonlinear optimization*. Princeton university press, 2011.

[46] A. Sheremet et al. 'Absorption of scalar waves in correlated disordered media and its maximization using stealth hyperuniformity'. In: *Physical Review A* 101.5 (May 2020). URL: http://dx.doi.org/10.1103/PhysRevA.101.053829.

[47] Bo Sjöberg et al. 'Interparticle interactions and structure in nonideal solutions of human serum albumin studied by small-angle neutron scattering and Monte Carlo simulation'. In: *Biophysical Chemistry* 52.2 (Oct. 1994), pp. 131–138. URL: https://doi.org/10.1016/0301-4622(94)00089-1.

[48] Frank H. Stillinger et al. 'Pair Correlation Function Realizability: Lattice Model Implications'. In: *The Journal of Physical Chemistry B* 108.51 (Aug. 2004), pp. 19589–19594. URL: https://doi.org/10.1021/jp0478155.

[49] S. Torquato et al. 'Controlling the Short-Range Order and Packing Densities of Many-Particle Systems'. In: *The Journal of Physical Chemistry B* 106.33 (July 2002), pp. 8354–8359. URL: https://doi.org/10.1021/jp0208687.

[50] S. Torquato et al. 'Exactly solvable disordered sphere-packing model in arbitrary-dimensional Euclidean spaces'. In: *Physical Review E* 73.3 (Mar. 2006). URL: https://doi.org/10.1103/physreve.73.031106.

[51] S Torquato et al. 'Random Heterogeneous Materials: Microstructure and Macroscopic Properties'. In: *Applied Mechanics Reviews* 55.4 (July 2002), B62–B63. URL: https://doi.org/10.1115/1.1483342.

[52] Salvatore Torquato. 'Hyperuniform states of matter'. In: *Physics Reports* 745 (June 2018), pp. 1–95. URL: https://doi.org/10.1016/j.physrep.2018.03.001.

[53] G. Torrie et al. 'Monte Carlo calculation of y(r) for the hard-sphere fluid'. In: *Molecular Physics* 34.6 (Dec. 1977), pp. 1623–1628. URL: https://doi.org/10.1080/00268977700102821.

[54] Leung Tsang et al. *Scattering of Electromagnetic Waves: Numerical Simulations*. Wiley, May 2001. URL: http://dx.doi.org/10.1002/0471224308.

[55] O.U. Uche et al. 'On the realizability of pair correlation functions'. In: *Physica A: Statistical Mechanics and its Applications* 360.1 (Jan. 2006), pp. 21–36. URL: https://doi.org/10.1016/j.physa.2005.03.058.

[56] Kevin Vynck et al. 'Light in correlated disordered media'. In: *Reviews of Modern Physics* 95.4 (Nov. 2023). URL: http://dx.doi.org/10.1103/RevModPhys.95.045003.

[57] Masami Yamada. 'Geometrical Study of the Pair Distribution Function in the Many-Body Problem'. In: *Progress of Theoretical Physics* 25.4 (Apr. 1961), pp. 579–594. URL: https://doi.org/10.1143/ptp.25.579.

[58] C. L. Y. Yeong et al. 'Reconstructing random media'. In: *Physical Review E* 57.1 (Jan. 1998), pp. 495–506. URL: https://doi.org/10.1103/physreve.57.495.

[59] Ge Zhang et al. 'Realizable hyperuniform and nonhyperuniform particle configurations with targeted spectral functions via effective pair interactions'. In: *Physical Review E* 101.3 (Mar. 2020). URL: https://doi.org/10.1103/physreve.101.032124.

Chapter 5

Conclusions

Multiple Effective Wavenumbers. In Chapter 2, our primary goal was to establish solid proof for the existence of multiple effective wavenumbers within an averaged particulate material - a phenomenon considered unconventional in the context of isotropic homogeneous media supporting only scalar waves. This finding holds substantial significance as it challenges conventional expectations and aligns with theoretical predictions [5, 6, 7, 16, 17, 18] highlighting the direct impact of multiple wavenumbers on the behaviour of transmitted and reflected waves in particulate materials with random microstructure.

Our rigorous Monte-Carlo simulations, undertaken to validate the presence of multiple effective wavenumbers, confirmed the existence of two distinct wavenumbers contributing to the total field as shown in Figure 2.8 and closely aligns with our theoretical predictions. As far as we are aware, this is the first clear validation on predictions of more than one effective wavenumber.

In a practical sense, a reasonable question that arose during this research was how to identify the factors leading to the appearance of multiple effective wavenumbers. Specifically, we wanted to understand when the classical theory, which relies on just one effective wavenumber [2, 8, 9, 11, 12, 15], might not give accurate results. Existing literature [6, 7, 10] has revealed a dispersion equation (2.13) as the source of effective wavenumbers k_p. Dealing with the dispersion equation (2.13) can be quite time-consuming but there is a clear takeaway from our findings: strong scattering gives rise to multiple wavenumbers.

Ewald-Oseen extinction theorem. One achievement we did not expect was to prove the *Ewald-Oseen extinction theorem* [1, 4, 13], and determine exactly how far the incident wave travels before becoming extinct in a disordered particulate material. The proof of extinction in particulate materials also demonstrates that the average

transmitted field behaves as a sum of effective waves, provided the distance from the material boundary exceeds the extinction length. Additionally, our work has provided a precise determination of the extinction length, shedding light on the distance an incident wave must travel before becoming extinct. These theoretical achievements enhance our comprehension of wave transmission in complex particulate media.

Wave reflection. In Chapter 3, we refined our understanding of wave reflections by employing two different methods to calculate the reflection coefficients: the *Dominant-wavenumber* and the *All-wavenumbers* methods. The former considers a single effective wavenumber k_1, whereas the latter includes multiple wavenumbers. Our analysis showed that for sound-hard particles, both methods produced matching results. However, in the case of sound-soft particles where multiple wavenumbers can get excited, the results do not agree. This indicates that the existence of multiple wavenumbers leads to changes in the reflection coefficients.

Asymptotic location of wavenumbers. An important finding was the determination of multiple effective wavenumbers in three dimensions, by solving an implicit dispersion equation. We developed an asymptotic method to identify complex effective wavenumbers in three dimensions, particularly for monopole scatterers. When comparing the analytical findings derived asymptotically with the numerical results, we showed that both approaches closely match.

Cookie-cutter method. Perhaps the most significant finding in our computational analysis of particulate materials was the *Cookie-cutter* method. This innovative approach, detailed in Section 3.3.2, was a decisive factor to tackle the challenges that arose when performing Monte-Carlo simulations. Typically, each simulation involves placing a set of particles within a finite region, a process that can introduce artefacts from the boundaries of the particulate. The Cookie-cutter method effectively eliminated these boundary artefacts, allowing us to accurately simulate the desired pair-correlations.

Structural determination. In our research, detailed in Chapter 4, we tackled the challenge of identifying particle configurations based on their pair-correlations. We deduced from first principles the calculations necessary for both the pair-correlation function $\mathrm{g}(r)$ and the structure factor $\mathrm{S}(k)$, for finite random particulate materials. To accomplish that, we showed how to avoid the effects of boundaries when calculating pair-correlations. This allowed us to accurately determine particle configurations from their pair-correlations or structure factors, marking a significant advancement in our ability to understand and manipulate particulate material properties.

Gradient-based Optimisation. Developing more efficient methods for reconstructing particle configurations from pair-correlations remains an open question in the fields of material science and computational chemistry [14]. Our proposed method employed techniques from smooth nonlinear optimisation to enhance efficiency. Since the structure factor is a smooth function of the particle positions, we developed a two step gradient-based method as a more efficient alternative to traditional non-gradient techniques. The process involves a global optimisation step to avoid particle locking, and a subsequent local optimisation step for fine-tuning.

Future Avenues. Most sensing methods, for particulate materials [3], attempt to link the wavespeed and attenuation to the microstructure. This link only works when there is a single effective wavenumber. By establishing that there are at least two effective wavenumbers, in some parameter regimes, we now can foresee that current sensing methods are unlikely to work in these regimes. To address this, there are two possible avenues:

- Verify for which materials and parameter regimes there is approximately only one effective wavenumber.
- Accept that there are two wavenumbers, try to measure both, and extract from both of them more information about the microstructure (i. e. average particle size and concentration) than would be possible when just measuring one effective wavenumber.

These are both promising directions for further research. In terms of the first bullet point, we note that there is a lot of current work on adding resonators to materials, and that our work indicates that resonators would trigger several effective wavenumbers.

In this thesis, we developed a robust theoretical and numerical framework to understand wave materials influence wave transmission. We demonstrated that the average transmitted wave consists only of effective waves and our Cookie-cutter method effectively eliminates artefacts from the boundary of the particulate. Having said that, an important question arises: How can we tune the material to alter those transmitted fields? For instance, can we design materials that can block certain waves by using specific patterns of particle configurations? This question has been unresolved, however, our innovative gradient-based approach to reconstruct particle configurations from pair-correlations offers a promising way to understand it better. So, the next natural step is to:

- Compare our method with brute-force methods such as Genetic Algorithms, and Simulated Annealing, in terms of efficiency and accuracy.
- Create a method to generate families of pair-correlations that meet the restric-

tions presented in Section 4.6.1.
- Test that our method is able to recover a wide range of pair-correlations.
- Extend to materials with different types of particles, often called multi-species.
- Develop a systematic way to include prior information about how different sub-components tend to form in the material. That is, to use prior information from chemistry and physics in the optimisation method.

This seems to be an unexplored approach that could increase the performance of this inverse problem and extend our understanding of material properties at a fundamental level.

In conclusion, my work has raised more questions than answers. At the very least, I have shown how there are many opportunities in studying waves in disordered materials.

References

[1] Max Born et al. *Principles of Optics: 60th Anniversary Edition*. Cambridge University Press, Dec. 2019. URL: http://dx.doi.org/10.1017/9781108769914.

[2] Rémi Carminati et al. *Principles of Scattering and Transport of Light*. Cambridge University Press, June 2021. URL: https://doi.org/10.1017/9781316544693.

[3] R E Challis et al. 'Ultrasound techniques for characterizing colloidal dispersions'. In: *Reports on Progress in Physics* 68.7 (June 2005), pp. 1541–1637. URL: https://doi.org/10.1088/0034-4885/68/7/r01.

[4] P. P. Ewald. 'Zur Begründung der Kristalloptik'. In: *Annalen der Physik* 354.1 (1916), pp. 1–38. URL: https://doi.org/10.1002/andp.19163540102.

[5] Artur L. Gower et al. 'A proof that multiple waves propagate in ensemble-averaged particulate materials'. In: *Proceedings of the Royal Society A: Mathematical, Physical and Engineering Sciences* 475.2229 (Sept. 2019), p. 20190344. URL: http://dx.doi.org/10.1098/rspa.2019.0344.

[6] Artur L Gower et al. 'Effective waves for random three-dimensional particulate materials'. In: *New Journal of Physics* 23.6 (June 2021), p. 063083. URL: http://dx.doi.org/10.1088/1367-2630/abdfee.

[7] Artur L. Gower et al. 'Multiple Waves Propagate in Random Particulate Materials'. In: *SIAM Journal on Applied Mathematics* 79.6 (Jan. 2019), 2569–2592. URL: http://dx.doi.org/10.1137/18M122306X.

[8] C. M. Linton et al. 'Multiple Scattering by Multiple Spheres: A New Proof of the Lloyd–Berry Formula for the Effective Wavenumber'. en. In: *SIAM J. Appl. Math.* 66.5 (Jan. 2006), pp. 1649–1668. URL: http://epubs.siam.org/doi/abs/10.1137/050636401 (visited on 14/09/2016).

[9] C. M. Linton et al. 'Multiple scattering by random configurations of circular cylinders: Second-order corrections for the effective wavenumber'. en. In: *J. Acoust. Soc. Am.* 117.6 (2005), p. 3413. URL: http://scitation.aip.org/content/asa/journal/jasa/117/6/10.1121/1.1904270 (visited on 04/09/2016).

[10] Francine Luppé et al. 'Effective wave numbers for thermo-viscoelastic media containing random configurations of spherical scatterers'. In: *The Journal of the Acoustical Society of America* 131.2 (Feb. 2012), pp. 1113–1120. URL: https://doi.org/10.1121/1.3672690.

[11] P. A. Martin. 'Multiple scattering by random configurations of circular cylinders: Reflection, transmission, and effective interface conditions'. In: *The Journal of the Acoustical Society of America* 129.4 (Apr. 2011), 1685–1695. URL: http://dx.doi.org/10.1121/1.3546098.

[12] Michael I. Mishchenko. *Electromagnetic Scattering by Particles and Particle Groups: An Introduction*. Cambridge University Press, Apr. 2014. URL: http://dx.doi.org/10.1017/CBO9781139019064.

[13] C. W. Oseen. 'Über die Wechselwirkung zwischen zwei elektrischen Dipolen und üer die Drehung der Polarisationsebene in Kristallen und Flüssigkeiten'. In: *Annalen der Physik* 353.17 (1915), pp. 1–56. URL: https://doi.org/10.1002/andp.19153531702.

[14] Edoardo Patelli et al. 'On optimization techniques to reconstruct microstructures of random heterogeneous media'. In: *Computational Materials Science* 45.2 (Apr. 2009), pp. 536–549. URL: https://doi.org/10.1016/j.commatsci.2008.11.019.

[15] V. K. Varadan et al. 'Multiple scattering theory for waves in discrete random media and comparison with experiments'. In: *Radio Science* 18.3 (May 1983), pp. 321–327. URL: https://doi.org/10.1029/rs018i003p00321.

[16] J. R. Willis. 'Transmission and reflection at the boundary of a random two-component composite'. In: *Proc. R. Soc. A* 476.2235 (Mar. 2020), p. 20190811. URL: https://doi.org/10.1098/rspa.2019.0811.

[17] J. R. Willis. 'Transmission and reflection of energy at the boundary of a random two-component composite'. In: *Proceedings of the Royal Society A: Mathematical, Physical and Engineering Sciences* 479.2271 (Mar. 2023). URL: http://dx.doi.org/10.1098/rspa.2022.0730.

[18] J.R. Willis. 'Some personal reflections on acoustic metamaterials'. In: *Wave Motion* 108 (Jan. 2022). URL: http://dx.doi.org/10.1016/j.wavemoti.2021.102834.